IMAGING, CHARACTERIZATION AND PROCESSING WITH AXICON DERIVATIVES

by

Andrew Grey Saikaley

A thesis submitted in partial fulfillment
of the requirements for the degree of
Master of Science (MASc) in Engineering

The School of Graduate Studies
Laurentian University
Sudbury, Ontario, Canada

THESIS DEFENCE COMMITTEE

Laurentian Université/Université Laurentienne
School of Graduate Studies/École des études supérieures

Title of Thesis Titre de la thèse	IMAGING, CHARACTERIZATION AND PROCESSING WITH AXICON DERIVATIVES
Name of Candidate Nom du candidat	Saikaley, Andrew Grey
Degree Diplôme	Master of Applied Science
Department/Program Département/Programme	Natural Resources Engineering
Date of Defence Date de la soutenance	July 12, 2013

APPROVED/APPROUVÉ

Thesis Examiners/Examinateurs de thèse:

Dr. Brahim Chebbi
(Supervisor/Directeur de thèse)

Dr. Ilya Golub
(Co-supervisor/Co-directeur de thèse)

Dr. Meysar Zeinali
(Committee member/Membre du comité)

Dr. Michel Piché
(External Examiner/Examinateur externe)

Approved for the School of Graduate Studies
Approuvé pour l'École des études supérieures

Dr. David Lesbarrères
M. David Lesbarrères
Director, School of Graduate Studies
Directeur, École des études supérieures

ACCESSIBILITY CLAUSE AND PERMISSION TO USE

I, **Andrew Grey Saikaley**, hereby grant to Laurentian University and/or its agents the non-exclusive license to archive and make accessible my thesis, dissertation, or project report in whole or in part in all forms of media, now or for the duration of my copyright ownership. I retain all other ownership rights to the copyright of the thesis, dissertation or project report. I also reserve the right to use in future works (such as articles or books) all or part of this thesis, dissertation, or project report. I further agree that permission for copying of this thesis in any manner, in whole or in part, for scholarly purposes may be granted by the professor or professors who supervised my thesis work or, in their absence, by the Head of the Department in which my thesis work was done. It is understood that any copying or publication or use of this thesis or parts thereof for financial gain shall not be allowed without my written permission. It is also understood that this copy is being made available in this form by the authority of the copyright owner solely for the purpose of private study and research and may not be copied or reproduced except as permitted by the copyright laws without written authority from the copyright owner.

Abstract

Axicons have been proposed for imaging applications since they offer the advantage of extended depth of field (DOF). This enhanced DOF comes at the cost of degraded image quality. Image processing has been proposed to improve the image quality. Initial efforts were focused on the use of an axicon in a borescope thereby extending depth of focus and eliminating the need for a focusing mechanism. Though promising, it is clear that image processing would lead to improved image quality. This would also eliminate the need, in certain applications, for a fiber optic imaging bundle as many modern day video borescopes use an imaging sensor coupled directly to the front end optics.

In the present work, three types of refractive axicons are examined: a linear axicon, a logarithmic axicon and a Fresnel axicon. The linear axicon offers the advantage of simplicity and a significant amount of scientific literature including the application of image restoration techniques. The Fresnel axicon has the advantage of compactness and potential low cost of production. As no physical prior examples of the Fresnel axicons were available for experimentation until recently, very little literature exists. The logarithmic axicon has the advantage of nearly constant longitudinal intensity distribution and an aspheric design producing superior pre-processed images over the aforementioned elements. Point Spread Functions (PSFs) for each of these axicons have been measured. These PSFs form the basis for the design of digital image restoration filters. The performance of these three optical elements and a number of restoration techniques are demonstrated and compared.

Keywords

axicon, image processing, Wiener Deconvolution, histogram equalization, point spread function, characterization, extended depth of field, resolution limit

Acknowledgments

First and foremost, I would like to thank Dr. Brahim Chebbi and Dr. Ilya Golub (my supervisors) for their patience, encouragement, and input throughout this effort.

Jennifer Levy was instrumental in the processing of the final images. Jennifer's efforts over the winter holidays helped to ensure that I was able to complete this thesis when I did. Also, many thanks to Igor Pak for his early work on the axicon and fibre optic imaging bundle.

I would like to thank B-Con Engineering of Ottawa and the Ontario Centres of Excellence whose funding helped to sustain me while carrying out this work.

Finally, I would also like to thank my family, without whom I would not have had the freedom to do graduate work.

Table of Contents

List of Tables and Figures

Nomenclature

a	Radius of lens aperture
DOF	Depth of field
f	Focal length
J_0	Bessel function of order 0
k	Wave number
n	Index of refraction
p	Distance from object to lens
q	Distance from image to lens
r	radius in cylindrical coordinates
w_{20}	Defocusing parameter
X_1	Distance from object to lens
X_2	Distance from object to imaging surface
z	Longitudinal distance in cylindrical coordinates

Greek letters

α	Axicon angle
β	Angle of rays with respect to axicon axis
λ	Wave length of light

Chapter I
INTRODUCTION
1.1 Motivation

Traditional optical systems, as applied to cameras, microscopes, telescopes, borescopes and endoscopes, typically use conventional spherical lenses. One of the drawbacks of spherical lenses is that they have a fixed focal length resulting in a short depth of field (DOF). A focussing mechanism is therefore required to produce a sharp image of an object within the field of view. These focusing mechanisms add cost to optical systems by increasing the number of lenses and the inclusion of precision mechanical traversing components they require. To reduce the need for such mechanisms, one can extend the depth of focus somewhat by using a smaller aperture, but it is at the expense of light energy reaching the imaging surface. In order to compensate for this, longer exposure periods are required to capture sufficient light. Though this may be acceptable when capturing images where there is little or no movement of the object relative to the camera, where there is relative motion, blurry images are often the result. Still, with a decrease in the size of the aperture improvement in the DOF tends to be modest.

In this thesis, we explore the use of axicons to extend the DOF of optical systems and to avoid the need of expensive focusing systems for some applications. Axicons, first introduced by John McLeod at Eastman Kodak in the early 1950s, are conical optical elements that refract light at a constant angle as a function of the radial distance from the optical axis. They are in effect a revolved prism. Instead of focussing light to a point as is the case for spherical lenses, axicon lenses focus light along a line, extending DOF substantially.

1.2 Objectives

Initially, within the context of this research, efforts to create a three axicon optical system with remote focusing capability as described in Chebbi et al. (2010) were undertaken. The purpose was to apply this optical system to a borescope by adding an intermediate element in the form of a fibre optic imaging bundle. Though not entirely successful, a simplified borescope using a single axicon lens demonstrated a focussed image over a significant depth of field. The results, though promising, suggested the need to apply digital image processing to enhance the quality of the images captured with this rudimentary device. It was decided that a number of techniques including Weiner Deconvolution would be used and compared. Weiner deconvolution as described in Digital Image Processing (Gonzalez and Woods 2008) was used extensively for image restoration herein as it is an effective and commonly used technique. Comparisons are made to other simpler techniques including contrast enhancement using histogram equalization and noise reduction through multiple image averaging. These techniques are demonstrated individually and in combination. In order to do this effectively, it was deemed necessary to carry out fundamental characterization of these optical elements. The characterization would require the acquisition of the lenses' impulse response, or point spread functions (PSFs), which could then later be used to deconvolve the images captured by the optical system.

Additionally, two derivatives of the axicon, a refractive logarithmic axicon, and a Fresnel axicon have been fabricated for the first time. These two prototypes also showed promise in previous experiments, particularly the logarithmic axicon (Golub et al., 2010). The experimental setup used to collect results for the regular axicon was also used to capture equivalent results for these two prototypes. Image processing techniques were also applied to these images.

This work was undertaken to characterize and thereby, in part, help determine the potential usefulness of a group of lenses for imaging purposes under development by B-Con Engineering. B-Con Engineering is an optical engineering company that concentrates on optical systems design and prototyping for the high technology sector. B-Con is located in Ottawa Ontario Canada.

In addition to the above mentioned refractive axicon, diffractive axicons have been demonstrated to good effect in papers by Mikula et al (2005) and Druart et al (2008). Although the properties of the axicon have been studied for many years, two new elements have been included here, the logarithmic axicon and Fresnel axicon, these latter two elements are prototypes although an element with similar properties to the logarithmic axicon, but with smaller DOF, a logarithmic asphere has been studied previously, Chi and George (2001). The Fresnel axicon however is an entirely new lens that has yet to be studied.

Early work described in this text concentrates on the practical application of using an axicon, or its above mentioned derivatives, as the primary optical element in a fibre optic telescope (borescope or endoscope). Even with the crude nature of the components used in these early experiments, a 7400 fibre imaging bundle scavenged from an inexpensive borescope and a 0.3 megapixel CMOS detector, the results demonstrated the viability of an axicon in such an application.

To improve the image quality acquired by such a telescope it was determined that digital image processing (DIP) should be applied to improve the raw images produced. Wiener deconvolution was proposed initially, thus requiring characterization of the elements in question to determine

their respective point spread functions under various conditions. Examples of this type of work have in addition to Wiener deconvolution, other restoration algorithms are applied and compared.

1.3 Document Organization

This document is organized as follows: Chapter 2 is a basic overview of the background theory. A brief description of the optical elements and some of their characteristics are discussed. The impulse response of the optical elements under investigation is also presented. Image processing techniques are also discussed in this chapter. Of particular interest is the application of the impulse response as a degradation function that can be used in inverse filtering.

Chapter 3 discusses literature related to the present study. It also sheds light on deficiencies in previous research in so far as they support a rationale for the present work.

Chapter 4 describes the experimental setup and displays examples of the images collected by this setup. Of particular interest are the test images and the impulse response of the optical system at a variety of distances.

Chapter 5 demonstrates the results of a variety of image processing techniques as they are applied to the test images. The latter half of this chapter focusses on a range of distances that are not covered by the existing literature as far as could be found.

Chapter 6 is a discussion of the work of chapter 5. Conclusions and recommendations are made here with regards to the suitability of the optics for imaging purposes in addition to the suitability of image processing techniques, if any, that should be used.

Chapter II
BACKGROUND THEORY

This chapter covers the background theory for the optical elements considered and for the image processing techniques used to enhance the images. Section 2.1 is meant to give the reader a basic understanding of some of the optical characteristics of axicons, Fresnel axicons and logarithmic axicons. Section 2.2 discusses the Bessel beams which are typically used to describe the intensity profiles obtained from axicons. Sections 2.3 and 2.4 describe the digital image processing techniques in the spatial and spatial frequency domain, respectively (Gonzalez et al., 2004).

2.1 Description of Optical Elements

The simplest refracting axicon is a conical lens and is sometimes referred to as the regular, or linear, axicon. This and two other axicons, which were first characterized in our lab, are described next: the refractive logarithmic axicon (Golub et al., 2010) and the Fresnel axicon (Gourley et al., 2012). A geometric optics approach will be used to give the reader a basic understanding of their optical properties. A cross sectional representation of these three elements is shown in Fig. 2.1. All axicons used for this thesis have a radius of 12.7 mm.

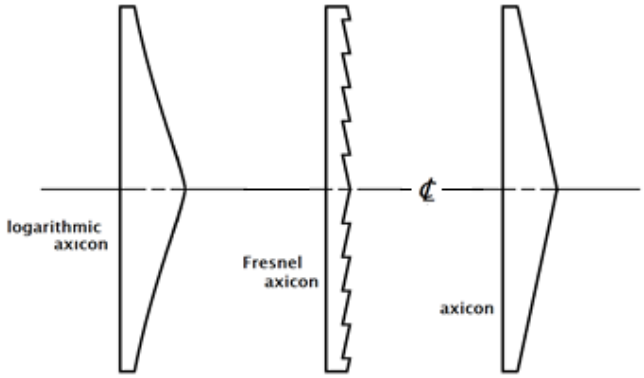

Figure 2.1:
Cross-sectional representation of axicon, Fresnel axicon, and logarithmic axicon.

2.1.1 Regular Axicon

The regular axicon was first introduced in the early 1950's. The axicon was created in an effort to produce a "universal-focus" lens (McLeod, 1954), who defined it by the following statement: "All axicons are figures of revolution. An axicon has the property that a point source on its axis of revolution is imaged to a range of points along its axis.". Figures 2.2 and 2.3 demonstrate the differences light rays are manipulated by a spherical lens (fig. 2.2) and an axicon (fig. 2.3).

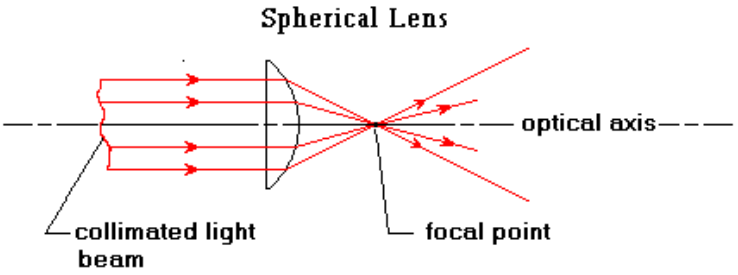

Figure 2.2:
Ray trace of spherical lens.

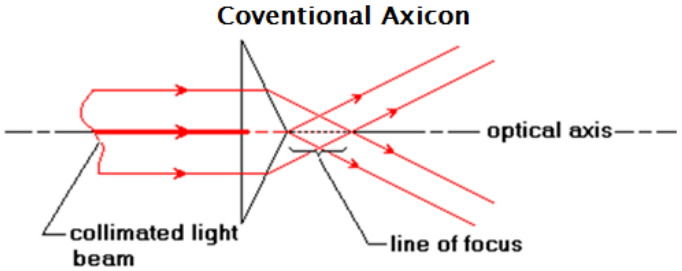

Figure 2.3:
Ray trace of conventional axicon.

Spreading light energy along a line instead of concentrating it to a single point, as is the case for a spherical lens, reducing optical power and contrast.

For incoming light plane waves, simple geometric optics suggests an uneven distribution of the light energy along the axis. In addition an increase in the angle of refraction causes the light energy to be spread over a shorter distance, making it more dense overall. The angle of refraction is driven, in part, by the angle of the axicon, α, this is analogous to the apex or base angle of a prism.

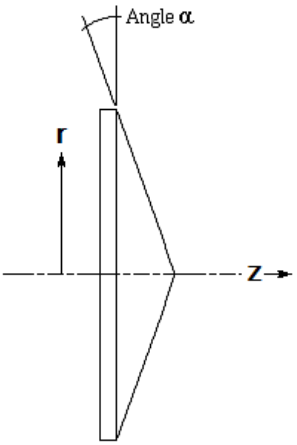

Figure 2.4:
Angle of axicon. For a 5° axicon, the 5° refers to the angle **α**.

2.1.2 Logarithmic Axicon

The logarithmic axicon though functionally similar to the regular axicon, is not a conical lens. This lens was conceived in an effort to achieve a constant intensity along the optical axis within a defined range when exposed to a plane wave. The center of the lens is in essence spherical, concentrating sufficient light energy at an initial focal point. As the radius increases, the light energy is evenly distributed along the optical axis, see figure 2.5.

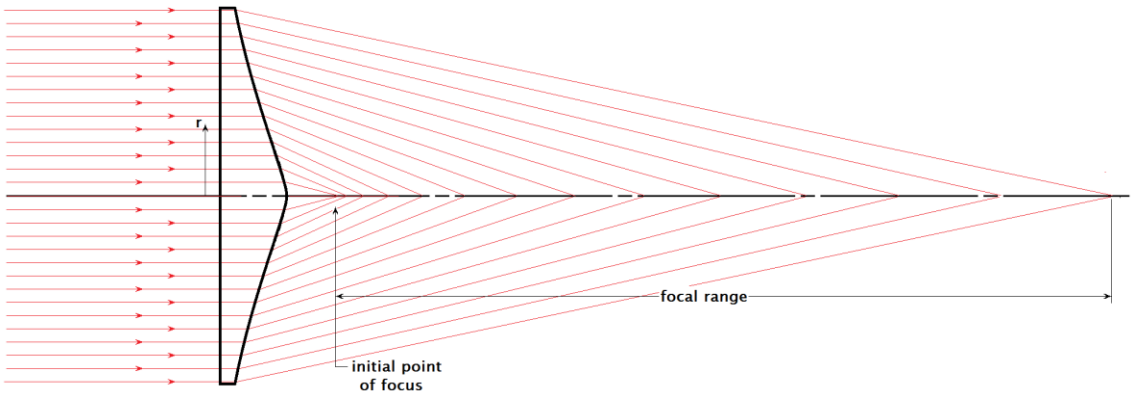

Figure 2.5: Distribution of light from a plane wave along optical axis for a logaxicon.

2.1.3 Fresnel Axicon

The Fresnel axicon (fraxicon) is, as one might imagine, a Fresnel version of a conventional axicon. Similar to a Fresnel lens, this element consists of concentric prism-like grooves with an apex angle equal to that of a regular axicon, as shown in figure 2.5, and whose action relies on refraction (Golub, 2006). The fraxicon has the advantages of low absorption and compactness. Additionally, this optical element is potentially inexpensive to produce.

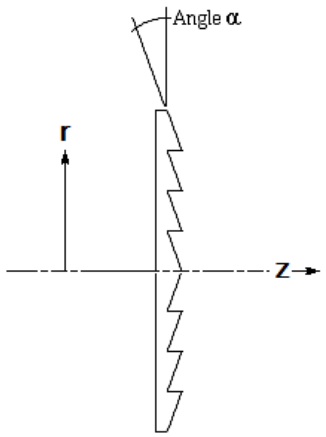

Figure 2.6: Angle of fraxicon.

There is however a slight reduction in the optical power density on any given imaging plane. The reason for this can be seen in figure 2.7.

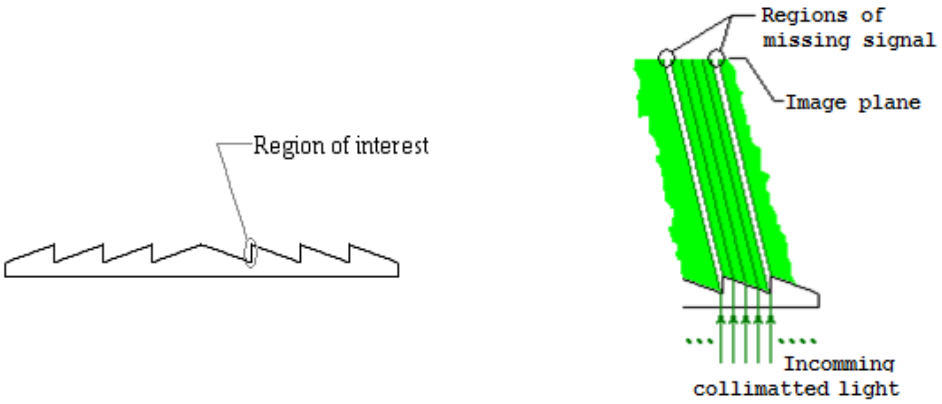

Figure 2.7: Disruption of optical signal from a Fresnel axicon.

Further degradation occurs for a point source at a finite distance from the lens. This signal distortion is caused by the surfaces parallel to the optical axis blocking and/or scattering light. Although the end result is similar to that for collimated light, a loss of optical power density at the imaging plane, the effect varies as a function of radius, as can be seen in figure 2.8. The further from the optical axis the incoming light enters the lens, the more severe the effect as the light forms a larger angle with the optical axis. The end result is that any light striking this surface will not behave in the same way as would be the case using a regular axicon.

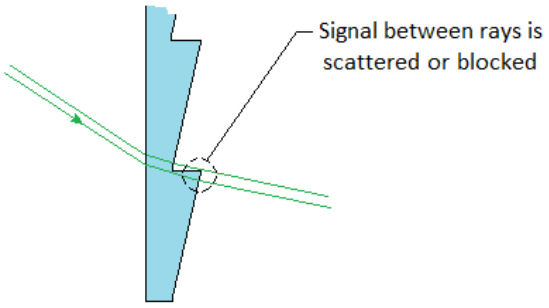

Figure 2.8: Fraxicon effects on point source at a finite distance.

2.2 Bessel beams and Bessel-Gauss beams

Durnin (1987) showed that a Bessel, or non-diffracting beam distribution is a solution to the wave equation. Axicons have been shown to produce Bessel-type beams (Roy and Tremblay, 1980). The Bessel beam distribution is ideal and cannot be realized in practice as it requires infinite energy. Instead a more realistic distribution can be obtained by considering an incoming Gaussian beam and solving the Fresnel diffraction integral with the stationary phase method (Friberg, 1996). The following variation of intensity distribution is obtained:

$$\boldsymbol{I(r,z) = I_0 \left(4\pi^2\beta^2 \frac{z}{\lambda}\right) exp\left[-\frac{2(\beta z)^2}{w_0^2}\right] {J_0}^2(k\beta r)} \qquad \textbf{(2.1)}$$

Here $\boldsymbol{J_0}$ is first kind Bessel function of zero order, $\boldsymbol{\beta}$ = arcsin(nsin α)-α, α is the axicon angle and $\boldsymbol{w_0}$ is the beam waist.

The above equation gives the variation of the intensity in a cylindrical coordinate system ***(z,r,θ)***, but since the lenses considered are symmetric about the z axis there is no variation with θ.

The on axis intensity is obtained by setting $\boldsymbol{r}$ = 0:

$$\boldsymbol{I(0,z) = I_0 \left(4\pi^2\beta^2 \frac{z}{\lambda}\right) exp\left[-\frac{2(\beta z)^2}{w_0^2}\right]} \qquad \textbf{(2.2)}$$

The radial/transverse distribution can also be obtained by setting **z** to a constant value along the axis. Since the images being captured are at relatively short distances, a plane wave is ill suited as an input. For the present study, a point source at a finite distance is used to characterize the optical system experimentally. This characterization can then be used to restore images captured

at these distances, in theory. In practice, it can be difficult to produce a satisfactory PSF experimentally. In such instances, an alternative image restoration approach is desirable.

2.3 Image Processing in the Spatial Domain

In general, enhancement is used to process an image in order to make it more suitable for a specific application.

A myriad of approaches to image processing exist, with many combinations and permutations. In many instances the optical system used to produce an image is insufficiently understood. This may require that observed deficiencies in an image be dealt with on a case by case basis. It may be possible to automate this technique once enough information has been inferred from successful application of various image processing techniques. There are two types of image enhancement:

- Spatial domain enhancement: manipulation of the pixels
- Frequency domain enhancement: manipulation of the Fourier transform of an image.

This subsection is dedicated to image processing techniques that are applied in the spatial domain. The two techniques discussed here are image averaging, a technique used to minimize random noise and adaptive histogram equalization. Subsection 2.4 will describe the spatial frequency domain processes used to carry out image restoration.

2.3.1 Spatial Domain Image Enhancement

Generally, an image reproduced by an optical system can be represented in the spatial domain as:

$$g(x, y) = T(f(x, y)) \quad \textbf{(2.3)}$$

Where f(x, y) is the input image, g(x, y) is the processed image, and T is the operator.

A neighbourhood of (x, y) is defined, and it is usually a square or rectangular sub-image centered about (x, y).

If the neighbourhood is made of the single pixel (x, y), then T is called a gray-level transformation and it can be written in the form:

$$s = T(r) \quad \textbf{(2.4)}$$

Where r denotes the gray level at $f(x, y)$ and s denotes the gray level of $g(x, y)$ at a point (x, y). T is also sometimes called intensity transformation or mapping transformation.

Some examples of gray-level transformations include image negatives, piecewise linear contrast stretching and histogram equalization. When larger neighbourhoods are considered, the transformations are called filters or masks.

2.3.2 Histogram Equalization

Histogram equalization (HE) is a technique used extensively in image processing to improve contrast in under or overexposed images.

For example, an underexposed image tends not to have higher intensity levels, meaning the upper end of the intensity spectrum is not used. Also, intensity levels that are very close to being the same are difficult to tell apart, reducing the ability to make out details. HE spreads out the signal over the entire spectrum. By making use of the entire intensity range, an underexposed image does not only appear brighter, it also shifts adjacent intensity levels so that they are easier

to discern from one another, improving overall contrast. Overexposed images also benefit from HE.

2.3.3 Adaptive Histogram Equalization

Adaptive histogram equalization (AHE) is a form of image manipulation that is based on global histogram equalization (GHE). Various forms of AHE have been developed to deal with short comings in GHE and even other forms of AHE in certain instances.

Histogram equalization in general takes the intensity level in an image and determines the number of pixel within the image at each intensity level. The intensity levels are then stretched to fill the entire range of available intensities, thereby increasing the contrast of the image. This is achieved by assigning the pixels in each intensity level/range the percentage of the range that matches there percentage of the total number of pixels in the image. For example, if 20% of the pixels are at a specific intensity (or range of intensities) within the image, this group of pixels will occupy 20% of the total intensity range in the equalized image. The pixels will still remain in the same order relative to all lighter and darker pixels in the original image, they will just be shifted and or stretched in terms of where and how much of the intensity range they occupy.

GHE is limited in its ability to enhance images with very bright and very dark areas since there is no possibility to enhance or stretch the contrast (no more available intensity range). In such instances, it might be possible to map the original intensity distribution, to make use of the middle of the intensity range.

Generally, the use of AHE breaks down the image into smaller sub-images and carries out histogram equalization on each of them. The size of the sub-image and the allowable range of intensities is largely a function of the specific technique.

We will have a look at several varieties of AHE techniques and discuss some of their advantages and disadvantages. The techniques that will be discussed here will include:

- Local Histogram Equalization (LHE) also known as AHE
- Block Based Adaptive Histogram Equalization (BBAHE)
- Contrast Limited Adaptive Histogram Equalization (CLAHE)

Within the literature even the above types are sometimes confused or described differently. We will try to describe and discuss a variety of techniques without getting too hung up on the labels.

2.3.4 Local Histogram Equalization

Local histogram equalization is a method that takes a histogram of a neighbourhood of pixels within an image and applies this information to change the intensity level of the central pixel in the neighbourhood. The transformed pixel is then mapped to a new image file in the same location as the original pixel existed in the source image. The neighbourhood then shifts over by one pixel and repeats the process. This is carried out until every pixel in the original image has been transformed and mapped to the new image.

Advantages of this technique over other methods include:

- Improved local contrast where a GHE method would be limited.
- No block edge mismatching/discontinuities as would occur in BBAHE.

Disadvantages of this technique include:

- Noise and other artifacts are indiscriminately enhanced in areas of low contrast.
- Requires a significant amount of processing time or power (less suitable for real time image enhancement), although interpolative methods can be used to reduce computation.

- Large neighbourhood size increases blurring of edges.

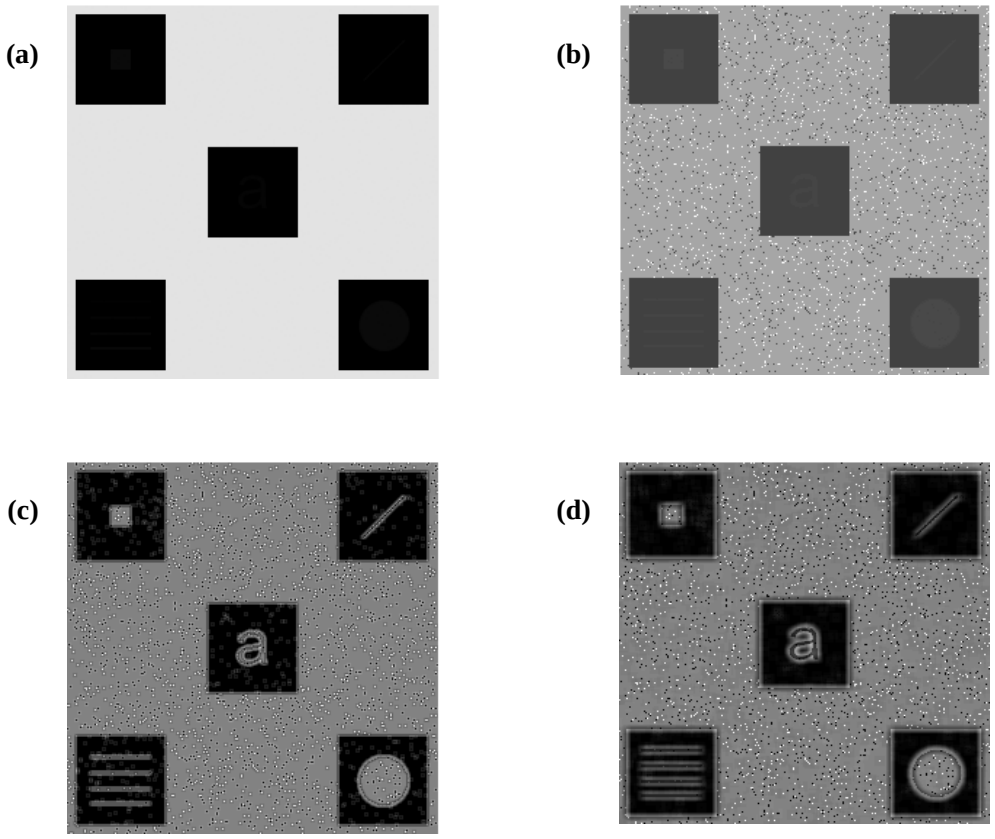

Figure 2.9: Global versus local adaptive histogram equalization: *a) Original image (Gonzalez et al., 2004) b) original image transformed using GHE. Note: in b) objects are barely visible due to pre-existing contrast in image. c) original image was transformed using L HE and a 3x3 neighbourhood. Notice noise in black boxes. d) transformed from the original using L HE and a 7x7 neighbourhood. Notice blurring around high intensity transition.*

2.3.5 Block Based Adaptive Histogram Equalization (BBAHE)

This technique cuts an image into a series of sub-images and carries out histogram equalization on each before reassembling them in a new image. Without further processing, this method is likely to have discontinuities at the boundary of each block. In order to avoid this, bilateral interpolation or smoothing is applied to the edges of adjacent sub-images.

This technique has similar disadvantages to the LHE in that in areas of low contrast, noise and other artifacts can be enhanced. While it reduces computation time for the initial AHE calculation when compared, this tends to be offset by the boundary treatment.

2.3.6 Contrast Limited Adaptive Histogram Equalization (CLAHE)

One drawback of AHE involves the equalization of regions with a low intensity range. In such regions, the noise can be excessively enhanced in addition to other artifacts. In order to limit this, a form of AHE that limits the increase in contrast to avoid enhancing unwanted artifacts and noise is applied.

This form of AHE can be implemented in tile form or window form. The window form (sliding window) is as described in LHE. The tile method carries out independent histogram equalization on individual sub-images (tiles) and moves to the next tile. One method of joining the tiles is through bilinear interpolation to eliminate artificial boundaries produced by separately processing each tile. A function exists within MATLAB® that uses this technique (adapthisteq). In either case, a clipping value or function is applied for each area to limit the contrast.

Advantages include reduced noise and artifacts over other AHE methods. This transformation produces a more subtle contrast enhancement leading to more realistic results in many instances.

2.3.7 Random Noise Reduction

Many random noise reduction techniques have the undesirable side effect of also reducing image sharpness. A simple technique to reduce random noise without a loss in sharpness is image averaging. This technique can be used when several identical images can be captured. By using the average value of the corresponding pixels from each of the images, random noise can be

significantly reduced. Although this is not often practical, with a rigid setup on an optical test bench it is possible to take any number of identical images.

In order for this technique to work, it is important to make sure that the 2 dimensional array elements used to sum the pixels can accept a sufficiently large value so as not to, in essence, clip the signal. Since pixel intensity is often stored in an 8 bit unsigned integer number, typically from 0 to 256, the pixel in the summing array should be 16 bit unsigned integer to ensure that they do not "clip". This would give one the ability to average up to 256 images without the risk of losing valuable information.

Calculating the averaged image is accomplished by dividing the 2-D array used to carry out the summation by a scalar quantity equal to the total number of images summed.

While finding the average value of the signal at each pixel is useful for producing an image with reduced noise, it can also be used for calculating signal to noise ratios. It can be done for the image as a whole or with a sufficient number of images, for individual pixels.

2.4 Image Processing in the Frequency Domain

Imaging systems are inherently imperfect. They have a limited ability to reproduce sharpness or spatial frequency. The result is blurring. For a single point of light, it is easy to collect all the light energy that is smeared by an optical system and return it to a single point through a simple summation. This is easily done in digital imaging at least so long as all the light is captured by the imaging device. If, however, many points of light make up an image, the problem is no longer so simply resolved.

Consider that an image produced by an optical system is made up of a series of points. Each of the points of the image contains a certain amount of optical energy or brightness. But, since the system causes blurring, some of the light energy at that point should (for a perfect optical system) belong to a neighbouring point. Since each point of light is blurred, not all of the optical energy that is at any point is in fact entirely where it belongs.

The result of this overlapping of blurred points can be described mathematically by convolution. Although convolution or degrading of an idealized signal can be readily carried out in the time domain, deconvolution is more readily carried out in the frequency domain. In the case of imaging, it is carried out in the spatial frequency domain. First however, it is important to characterize the blurring.

2.4.1 Characterising System Degradation: The Point Spread Function

Optical or optoelectronic systems can be characterized by determining the system's response to a simple input in a similar way to electronic and mechanical systems. A system's impulse response can be determined using an impulse function. The resulting output is broadly known as the impulse response or degradation function. Since the output of an imaging system is typically a two dimensional image, the input (or forcing) and the response functions are also typically two dimensional in nature.

In many instances, one does not have access to the optical system. This makes it impossible to measure the system's response directly. It is however possible, in many instances, to use a sudden change, from the edge of an object in the image for example to determine the response.

The point spread function (PSF) is an optical system's impulse response. As an impulse, a point source is used as an input to the optical system. The PSF is so named because in practice, any

optical system blurs (spreads or smears) a point of light to some extent. The PSF is also referred to as the degradation function. An ideal input pulse is shown in figure 2.9 (a) and (c).

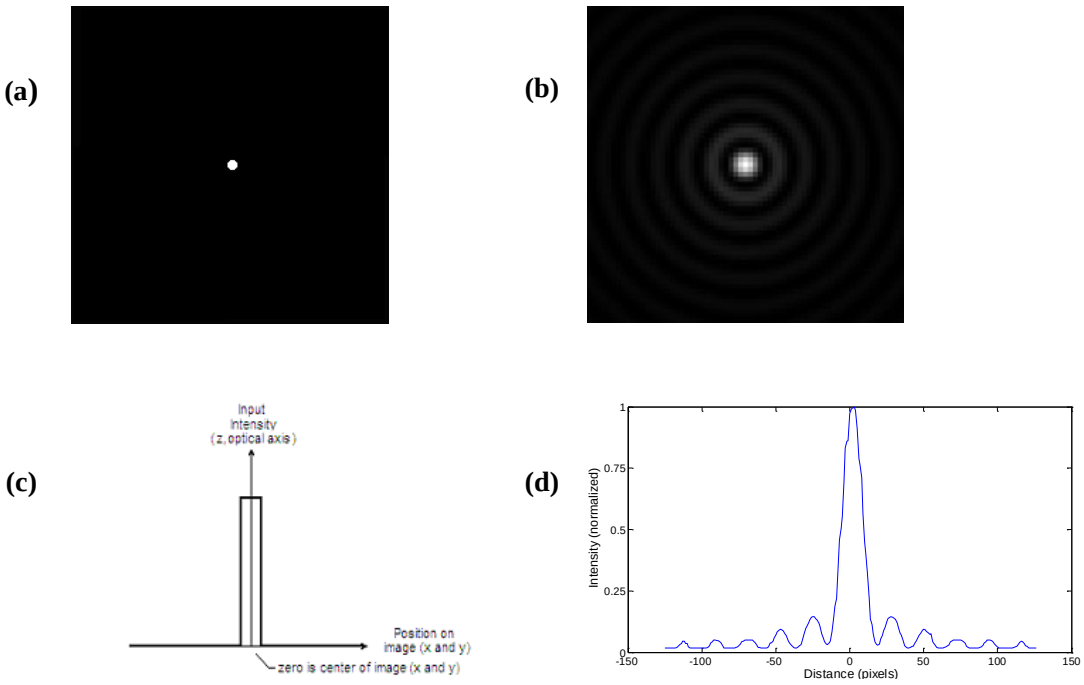

Figure 2.10: *a) Point source (system input). b) System response to adjacent input. The signal is smeared by the optical system (specifically this is characteristic of an axicon. c) Plot of input pulse. d) Plot of an axicon's response to a point source (point spread function).*

2.4.3 Direct Inverse Filtering

An integrated approach to image processing can be applied if the system used to produce the image is sufficiently well characterized. Once the system's effect on an input is understood, it should be possible to reverse it. By undoing the effect of the system on the input, the output should in theory be an ideal representation of the original input. This assumption is based on a noise free system.

An optical system that includes some form of integrated image restoration filter is shown in figure 2.11. The original object (or ideal image) is defined by $f(x, y)$.

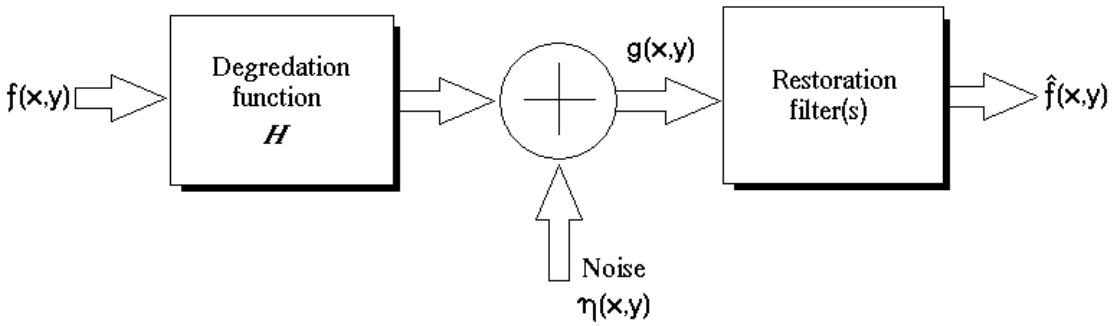

Figure 2.11: Integrated optoelectronic system with image restoration filter.

The degradation function, ***h*** describes the way in which the optical system modifies or degrades an input. This function reduces the quality of the ideal image in the process of reproducing it.This is the mathematical representation of the PSF. A noise function ***η(x,y)*** is added to the degradation function. The noise function is independent of the degradation function. This results in a degraded image, ***g(x,y)***, which includes the noise component within it. By applying an appropriate inverse function, it should be possible to reverse the effects of the degradation function. It is however necessary to first identify this degradation function or at least approximate it in some way.

Viewing an image as a series of impulses or points of light, it follows that each of these points is blurred in the same fashion as is the PSF. Due to the blurring of adjacent points of light, the effects of one point being blurred overlaps neighbouring pixels in the image generated by the optical system. The mathematical analogue of this process is convolution. So, the ideal image is convolved with the degradation function to produce the degraded image:

$$g(x,y) = h(x,y) \otimes f(x,y) + \eta(x,y) \qquad \textbf{(2.5)}$$

Where ***g(x,y)*** is the systems output (the degraded image), ***h(x,y)*** is the system response function, the degradation function or PSF, ***f(x,y)***, is the input function (the ideal un-degraded image), and ***η(x,y)*** is the noise function. The symbol $\otimes$ denotes convolution.

Deconvolving the degraded image from the degradation function is best carried out in the frequency domain using Fourier Transforms. Where ***f(x,y)***, ***g(x,y)***, ***h(x,y)*** , and ***η(x,y)*** are in the spatial domain, their frequency domain counterparts will be represented by ***F(u,v***) , ***G(u,v), H(u,v)*** and ***N(u,v***) respectively. Since deconvolution in the time/spatial domain transforms to multiplication in the frequency domain (spatial frequency) equation 5 becomes:

$$G(u,v) = H(u,v)F(u,v) + N(u,v) \qquad \textbf{(2.6)}$$

Assuming ***N(u,v)*** is negligible, it is possible to produce a facsimile of ***F(u,v***) (the un-degraded image) by dividing equation 6 by ***H(u,v)***:

$$\hat{F}(u,v) = F(u,v) + \frac{N(u,v)}{H(u,v)} \qquad \textbf{(2.7)}$$

Unfortunately, dividing the noise function by the degradation function often leads to poor performance in direct inverse filtering. This is due to zero or near zero elements within ***H(u,v)*** which cause the noise function to overwhelm the result.

2.4.4 Modulation Transfer Function

The modulation transfer function (MTF) is derived from the PSF. It is an optical system's spatial frequency response. As such, the MTF is the Fourier transform of the PSF, it is represented by ***H(u,v)*** (it appears in equations 6 and 7, it also appear later in equation 8 of this chapter).

2.4.5 Wiener Deconvolution

Norbert Wiener was among the first to use statistical methods to remove noise from signals. Without entering into a detailed derivation, the general form of the function as applied is:

$$\hat{F}(u,v) = \left[\frac{1}{H(u,v)} \frac{|H(u,v)|^2}{|H(u,v)|^2 + K} \right] G(u,v) \qquad \textbf{(2.8)}$$

Where $\boldsymbol{K = |N(u,v)|^2 / |F(u,v)|^2}$, referred to as the noise to signal ratio (NSR). The term $\boldsymbol{|N(u,v)|^2}$ is the power spectrum of the noise and $\boldsymbol{|F(u,v)|^2}$ is the power spectrum of the ideal image. Since these power spectra are often unknown, a constant $\boldsymbol{K}$ is often used. A value of zero for $\boldsymbol{K}$ implies that there is no noise in the system. If $\boldsymbol{K}$ is equal to zero, equation 8 reverts to equation 7, direct inverse filtering. Where the NSR is not known, it is generally possible to adjust this value until the best observable outcome is achieved.

In MatLab®, the MTF, ***H(u,v)***, is generated within the Wiener Deconvolution command, **deconvwnr**. Only a two dimensional PSF need be supplied in addition to the image and an NSR. The NSR used can in theory be calculated, but a trial and error approach is often used. Once a satisfactory value for the NSR is established for a given system, it appears to supply good results with only minor adjustments.

Chapter III
LITERATURE REVIEW
3.1 Types of Axicons

John H. McLeod is generally recognized as the pioneer in introducing the axicons which are optical elements generating a narrow focal line along the optical axis (McLoed, 1954 and McLoed, 1960). The transverse intensity of a collimated light beam passing through the axicon along the focal line can be approximated by a zero-order Bessel-type function and results in a non-diffracting beam which preserves its transverse distribution along the axis (Durnin, 1987). This characteristic of axicons results in an extended depth of focus (DOF). These properties differentiate the axicons from the more common spherical lenses which have shorter depth of fields and Gaussian like, diffracting transverse distribution beams.

There are many types of axicons, or optical elements in general, generating diffraction free Bessel-type beams and they can be refractive, reflective or diffractive. The most common are the refractive conical lenses which have been studied and used extensively and are commercially available. Some examples of investigations using these elements include Golub and Tremblay (1990) and Lei and Yao (2004). It is also possible to produce quasi non diffractive beams by using spherical lenses having strong spherical aberrations which cause an extended depth of field (Burvall et al., 2004), or combinations of refractive and reflective spherical elements (Burvall et al., 2007). Couture and Piché (1993) studied theoretically and experimentally the focusing properties of a pair of reflective axicons, one converging and one diverging. Recently, Brousseau et al. (2011) developed a magnetic liquid mirror axicon. Diffractive axicons have also been studied extensively, and are common; they mostly use diffractive circular gratings or

annular apertures (Turunen et al., 1988; Davidson et. al., 1991; Jaroszewicz et al., 1993; Popov and Friberg 1998). Disadvantages of diffractive axicons include their inefficient transmission of light and strong wavelength dependence.

There are many investigations which describe the development, fabrication and applications of micro axicons, a few examples include Eah et al. (2003), Kuang and Fang (2010), Lee and Rolland (2008) and Kotlyar et al. (2011).

Bessel beams have been the subject of many theoretical investigations including: Durnin (1987), Overfelt and Kenney (1991), Staroński et al. (1992) and Čižmár and Dholakia (2009). While in general the beams produced by axicons have near zero-order Bessel function distribution, Paterson and Smith (1996), and Art and Dolakia (2000) showed the generation of higher order Bessel beams for diffractive and refractive axicons respectively.

Jaroszewicz (1997) presents a comprehensive review on the different types of axicons, their design and properties.

3.2 Applications of axicons

Many applications can benefit from the extended DOF produced by axicons and the limited diffraction of the beams they produce. For example, many investigations explored the use of axicons in laser trapping among them (Shao et al., 2006 and Golub and Tremblay, 1990). A combination of axicons and lenses is used to generate light rings which can be used to cut holes with a precise control of their diameters in laser machining (Rioux et al., 1978), also Matsuoka et al. (2006) investigated the use of axicons in micro drilling. The limited divergence of Bessel beams was suggested as a means of improving the spatial resolution in laser Doppler velocimetry

(Voigt et al., 2009). The use of axicon has also been proposed in corneal surgery (Ren and Birngruber, 1990). Chebbi et al. (2010) proposed a remote focusing system using three axicons which can be used in endoscopic or boroscopic systems.

Probably the most common application of axicons are in imaging, For example, Arimoto et al., (1992) proposed their use in a scanning optical system and Dufour et al. (2005) and Golub (2007) proposed their use in microscopy. In addition, an axicon was used to improve the lateral resolution of an optical coherence tomography system over a long DOF and also maintain a nearly constant intensity over a larger depth range than conventional systems (Ding et al., 2002).

The use of the extended DOF of axicons in imaging applications will be reviewed in detail in the next section.

3.3 Extended depth of field imaging and axicons

Imaging applications can benefit greatly from the extended DOF of axicons. Three dimensional representations of objects can be captured without the complexity a mechanical focusing system. Different methods have been proposed to extend the DOF of imaging systems, such as the use of optical power-absorbing apodizers (Ojeda-Castaneda et al., 1989) and wave front coding (Dowski and Cathey, 1995). Cathey et al. (1984) suggested integrating the image processing with image acquisition. They present good basic frequency domain theory with band-pass versus low-pass filtering. The paper alludes to the integration of image processing and optical systems in the vein of present efforts. It is however a purely theoretical treatment with no experimental data or results.

Several investigations studied imaging with refractive and diffractive optical elements with extended DOF. The extended DOF of axicons and the nearly non-diffracting beams they generate makes them ideal candidate for use in imaging. There are a few investigations in the literature which studied the use of axicons in imaging.

Mikula et al. (2005) examined the imaging properties of two diffractive optical elements with extended depth of field: a light sword optical element (LSOE) and a linear diffractive axicon. For each of these elements they used two devices: one with a depth of field extending from approximately 1108 mm from the element to about 1354 mm and the second one with a depth of field extending from 985 mm from the element to 1477 mm. They compared the results to those of a Fresnel lens having a focal distance limited by the center of the DOF of the above element which is equal to 1231 mm. They performed numerical simulations of the PSF and MTF and took images of an object placed at a distance p=3,000 mm at planes at distances q=1782, 1922, 2087, 2283 and 2520 mm corresponding to different values of a defocusing parameter.

Mikula et al. (2007) compared the imaging properties of a diffractive forward logarithmic axicon, an axilens which is a holographic lens with extended depth of field, and a diffractive light sword optical element (LSOE). The forward logarithmic axicon and axilens achieve the extended depth of field by radial modulation of the phase transmittance. The LSOE obtains extended depth of field by angular modulation. They present images and modulation transfer functions (MTFs) at a series of object distances p ranging from 250 to 2000 mm and at an imaging plane at a fixed distance q=20 mm from the optical element. Simulated and experimentally derived images for each of the aforementioned element types were presented. The results suggest that the LSOE with its angular modulation produces images and MTFs that

are far less affected by position along the optical axis. In a subsequent paper (Ares Garcia et al., 2008) manufactured and tested the imaging properties of a refractive LSOE which does not suffer from the strong chromatic aberrations associated with diffractive LSOE.

Druart et al. (2008) used a diffractive axicon (a series of equally spaced circular slits) as a single element telescope. A two-step process by digitally processing axicon-captured images to restore/deblur the images has been suggested. The paper describes how the element can be translated along the optical axis to zoom in on an object and remain in focus. Three images were taken. The first two with the object at 3m from the diffractive axicon, one with the imaging plane at 88mm and the other at 37mm. A comparison of the first two images demonstrated the zooming capability of the system. The third image was taken at a distance of 1.3m from the object to the diffractive element and 37mm from the element to the imaging surface. This third image combined with the second image mentioned above demonstrates the invariance of the cut-off frequency along the focal line (invariance in MTFs for these images). In order to improve the contrast in these images, a high pass filter was used.

Zhai et al. (2009) developed an optical system comprised of a spherical lens, an axicon and a CCD camera to acquire images. The images are then processed using a Wiener filter. The specific details of the digital image processing are very limited, but the results compared to the unprocessed images are presented. In this treatment, the axicon lens is used largely as a method of improving an optical systems depth of focus. The author does mention an overall drop in image quality compared to an axicon free system while in focus, but, adds that with the axicon (and digital image processing), the system is less sensitive to defocus. The base angle of the

axicon used is 0.01 radians (approx. 0.5^{o}). Such a small angle brings this optical element close to a flat glass plate. In spite of this fact, the improvement in depth of focus is well demonstrated.

Chi and George (2001) developed and manufactured a logarithmic asphere. They used this element in a camera which incorporates a sharpening filter allowing it to remain in focus over a significant depth of focus, from 610 to 6100 mm. The equation for the distance a ray must travel from a point along the optical axis through the lens and to the focal point on the image plane is used. The phase delay which appears in this equation is then isolated and solved using Fermat's principle. The phase delay is determined through direct integration and converted to a power series expansion. This approximation describes the thickness of the lens as a function of radius to within $\pm 10^{-5}$ mm.

Although point spread functions (PSFs) were measured, the filter masks used to sharpen the images did not rely heavily on these PSFs. The filter used resembles a conventional sharpening mask that can be applied directly using the MatLab® **imfilter** command. The new lens-camera combination demonstrated a significant improvement in depth of focus after image restoration was applied when compared to a conventional Nikon lens with the same focal length to diameter ratio (*f/D*), or *f*-number.

Refractive axicons are more efficient energy-wise than diffractive axicons for generating a diffraction-free beam. To our knowledge, they were not extensively investigated in imaging applications, with the exception of Zhai et al. (2009) who used them with a regular lens to extend its depth of field. They suffer however from the high cost related to the way they are manufactured. In addition, a linear axicon has a varying on-axis intensity distribution. The Fresnel axicon manufactured and characterized in our lab (Gourley et al., 2009 and Gourley et

al., 2011) has a potential for reducing the cost of manufacturing and at the same time providing advantages such as compactness and very low bulk absorption. Gourley et al. (2011) compared its light distribution performance to a regular axicon and showed that on average these distributions are comparable even though some oscillations on the on-axis intensity are observed. Chebbi et al. (2012) showed experimentally and theoretically that these oscillations can be inhibited by judicial choice of the period of the fraxicon.

To remedy the change in the longitudinal intensity distribution, a logarithmic axicon recently manufactured and characterized will be used (Golub et al., 2010). The on axis intensity was measured to demonstrate that it remained relatively constant over the intended design range. This was then compared to that of a conventional 5^{o} axicon.

Chapter IV

EXPERIMENTAL TECHNIQUES AND MEASUREMENTS

4.1 Imaging with Fiber Optic Bundle Axicon System

4.1.1 Test bench setup

In an effort to determine the feasibility of an axicon in a borescope application, a fiber optic imaging bundle was combined with an axicon to view an object as shown in Figure 4.1. In practical applications, for example using endoscopes or borescopes, this object would be in an enclosure. A camera placed at the other end of the bundle takes pictures of the transmitted image.

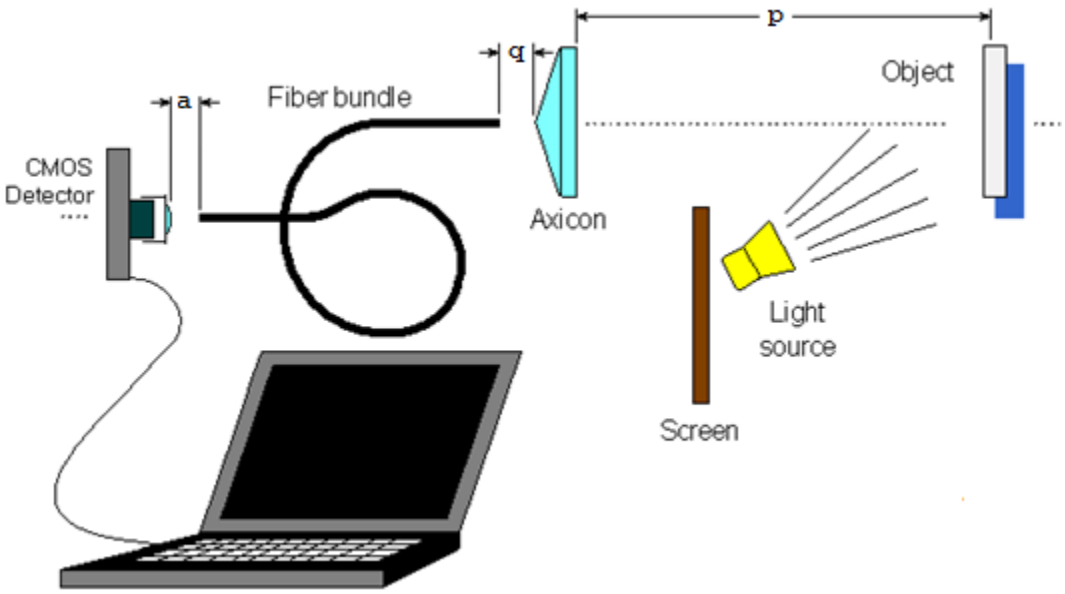

Figure 4.1: Fiber optic imaging bundle with axicon.

The imaging bundle was scavenged from a low cost borescope manufactured in China. The individual fiber size is approximately 15μm diameter with a total of 7400 fibers in the bundle. The CMOS detector used was a Logitech® Quickcam Deluxe 640x480 webcam digitally

enhanced to display 1.3 megapixels. A major advantage of this setup is that it allowed real time monitoring of image quality during setup and adjustment.

The fibre bundle ends were trimmed and polished to give sufficient optical clarity to carry out basic experiments. The CMOS detector optics was focused on the end of the fibre bundle, the fibre bundle having been placed as close to the CMOS detector's optics as possible. The intent was to have the fibre bundle fill as much of the detector imaging area as was practical.

4.1.2 Measurements

In order to demonstrate that an axicon can be used to improve depth of field over conventional spherical optics, images produced with a spherical lens were collected for comparison purposes. Therefore, the optical test bench previously described in this section was fitted initially with a spherical lens to collect images for this purpose. The spherical lens used had a 10 cm focal length. The images in Figure 4.2 are the result of using this lens. When using a regular lens, the image is blurred and unclear if displaced from the focal region even slightly as shown in Figure 4.2. The centre image is in focus. The image to the right of centre is 1 cm inside of the focal point and the image to the left of centre is 1cm beyond the focal point. The focal point is at a distance **p** from the object to the lens (see Figure 4.1).

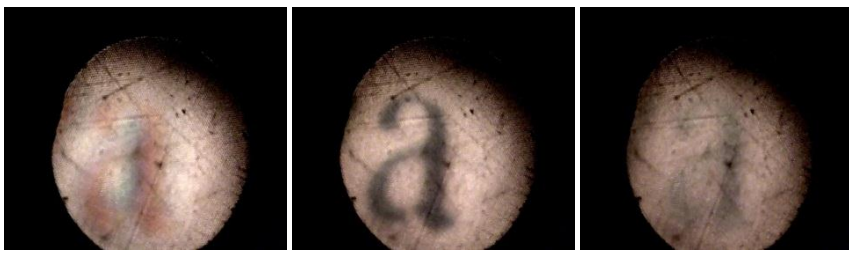

(a) **(b)** **(c)**

Figure 4.2:
Captured images using a lens of 10 cm focal length.
a) At 1cm before the focal point.
b) At the focal point.
c) At 1cm beyond the focal point.

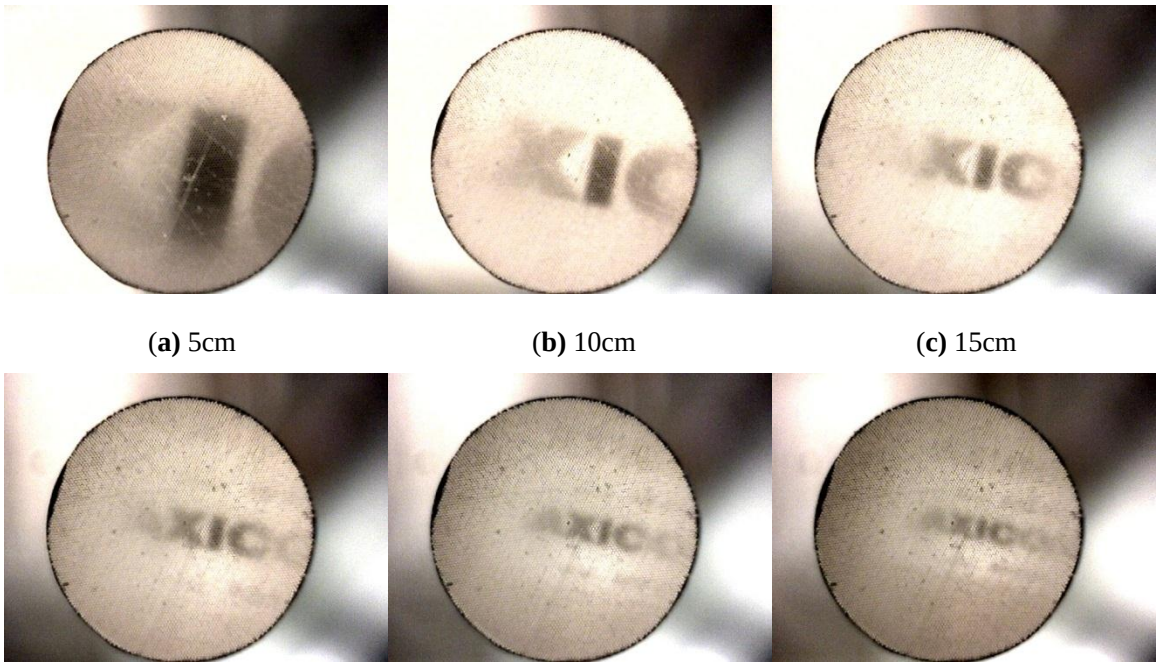

(**a)** 5cm (**b)** 10cm (**c)** 15cm

(d) 20cm (**e)** 25cm (**f)** 30cm

Figure 4.3: Captured images using fibre optic imaging bundle and 10° axicon. Distances given are from the object to the axicon.

The images in figure 4.3 were acquired using a 10° axicon. Using a fiber optic axicon system, the image could be placed at different locations along the focal region and still be viewed as shown in Figure 4.3. Although not shown here, the image remained in relative focus up to approximately **p** = 60 cm. All these pictures were taken from a video file which was recorded in real time while moving the optics and shows more clearly the advantage of using an axicon fiber optic system for a borescopic application.

4.2 Test Bench Setup for Lens Characterization

Just as is the case for a mechanical or electrical system, one can characterize an optical system by exciting it with a known input function and observe the systems output. In an effort to accomplish this task, a point source approximated by a tiny aperture was used as the input function. The systems output, known as the point spread function (PSF) and explained in chapter III, was captured using a 2 megapixel CMOS detector.

The test bench layout for collection of PSF images is shown below in figure 4.4. For the images within this section, a green laser (532 nm) was used. Both the axicon and fraxicon angle were 5° (see Figure 2.4 for an illustration of this angle).

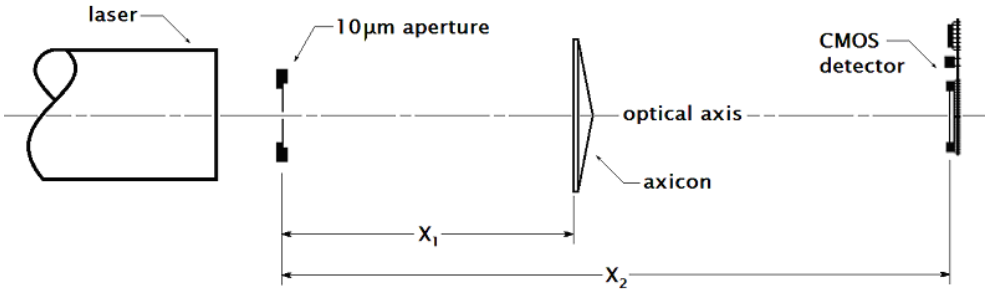

Figure 4.4:
PSF test bench setup

Optical element	Object distance **p**	Image distance **q**
Axicon (α=5°)	55 mm	145 mm, 245 mm, 345 mm
	80 mm	120 mm, 220 mm, 320 mm
	125 mm	75 mm, 175 mm, 275 mm
Fraxicon (α=5°)	55 mm	145 mm, 245 mm, 345 mm
	80 mm	120 mm, 220 mm, 320 mm
	125 mm	75 mm, 175 mm, 275 mm
Logaxicon	70 mm	130 mm, 230 mm, 330 mm
	80 mm	120 mm, 220 mm, 320 mm
	90 mm	110 mm, 210 mm, 310mm
	125 mm	75 mm, 175 mm, 275 mm
	145 mm	55 mm, 155 mm, 255 mm

Table 4.1: Values of p and q for first set of PSF and images measurements.

4.2.1 Axicon

The images that follow are examples of experimental PSFs taken using a 5° axicon. A 10 μm diameter aperture with a 532 nm laser for illumination was the point source. A pair of polarizing filters was used to vary the intensity of the laser. The filters were placed between the laser and the 10 μm aperture.

In Figure 4.5, each row purports to the same distance from the point source to the lens. As an example, row one images are all taken with the object or point source at a distance of 5.5 cm from the lens. This distance is the measurement $\mathbf{X_1}$ from Figure 4.4. Each column purports to the distance from the object to the imaging surface, $\mathbf{X_2}$ in Figure 4.4. So, all the images in column 1 below were taken at a distance, $\mathbf{X_2}$, of 20 cm from the point source to the imaging surface (CMOS detector).

Alternatively, $\mathbf{X_1}$ is equivalent to **p** the distance from the object to the lens, and $\mathbf{X_2 - X_1}$ is equivalent to **q**, the distance from the lens to the image.

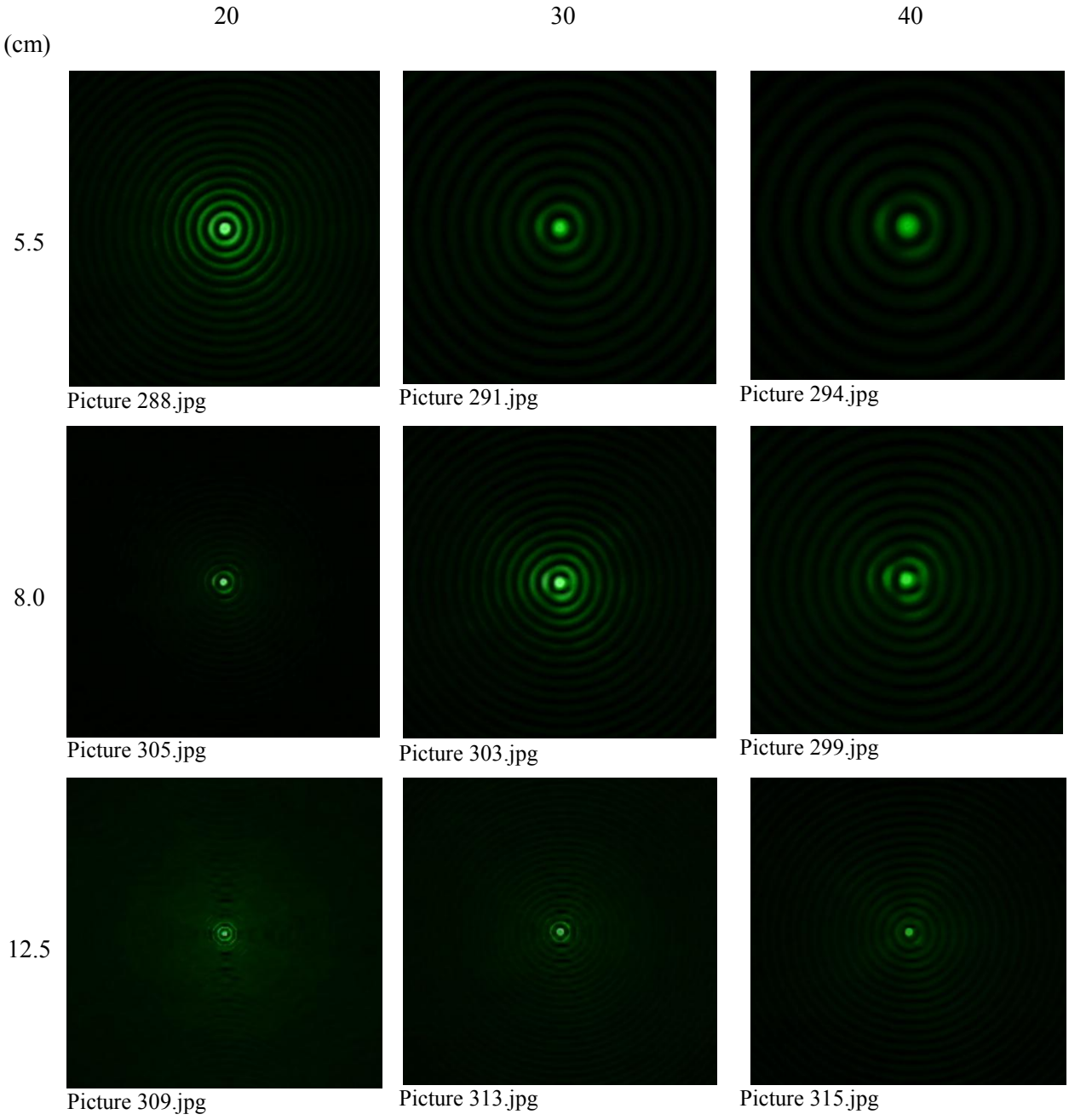

Figure 4.5: Measured Point Spread Function of 5° axicon.

Corresponding PSF plots for images on the previous page are shown below. The horizontal axis scale is in micrometers and the vertical axis is a normalised intensity (maximum intensity = 1, black = 0). These intensity plots were developed using an m-file created in MatLab®.

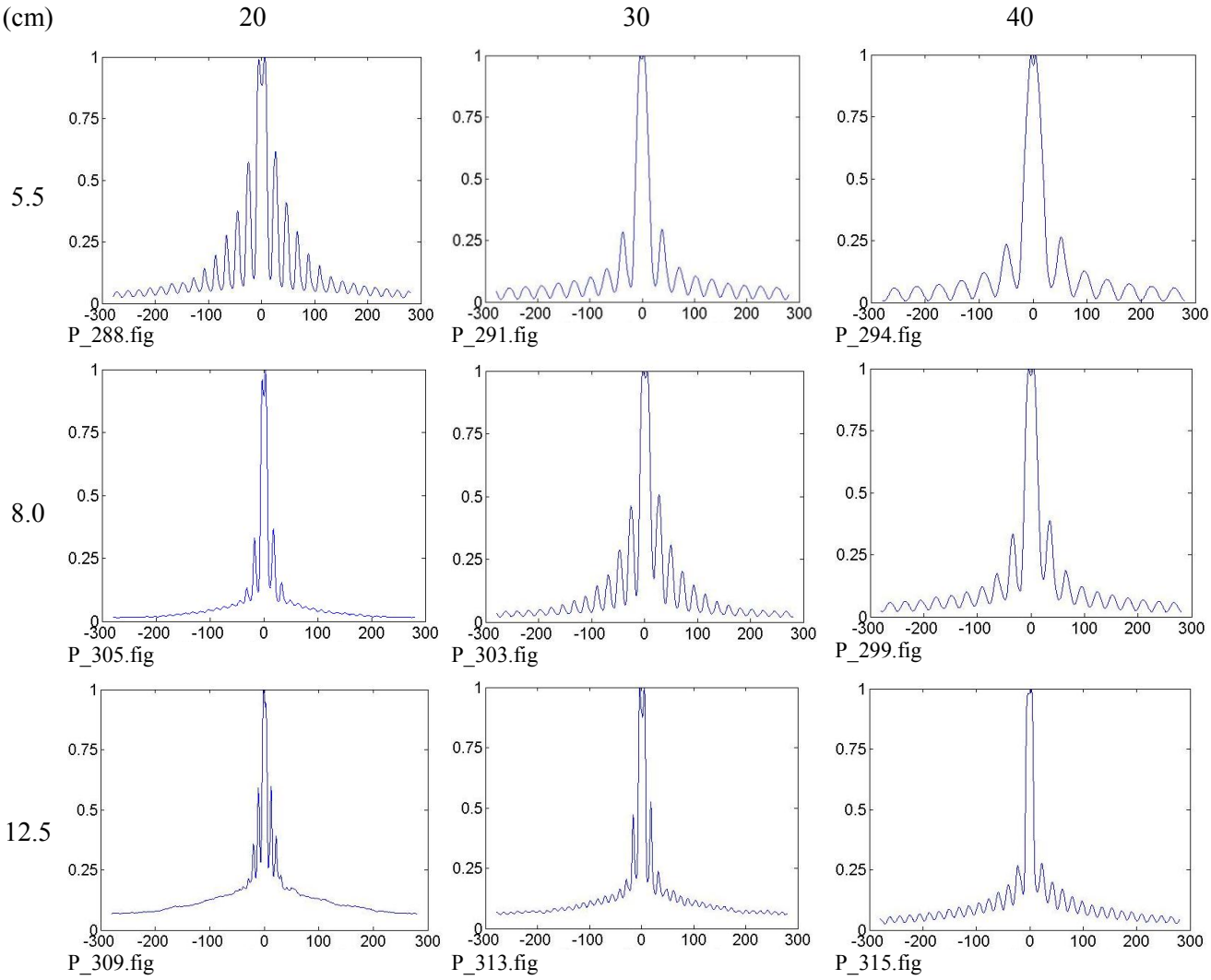

Figure 4.6: Point Spread Function plots for 5° axicon.

4.2.3 Fraxicon

The fraxicon PSF images, shown in Figure 4.7, were collected at the same distances and in the same way as for the axicon images in the previous section. This was done to allow for a direct comparison between the two lens types.

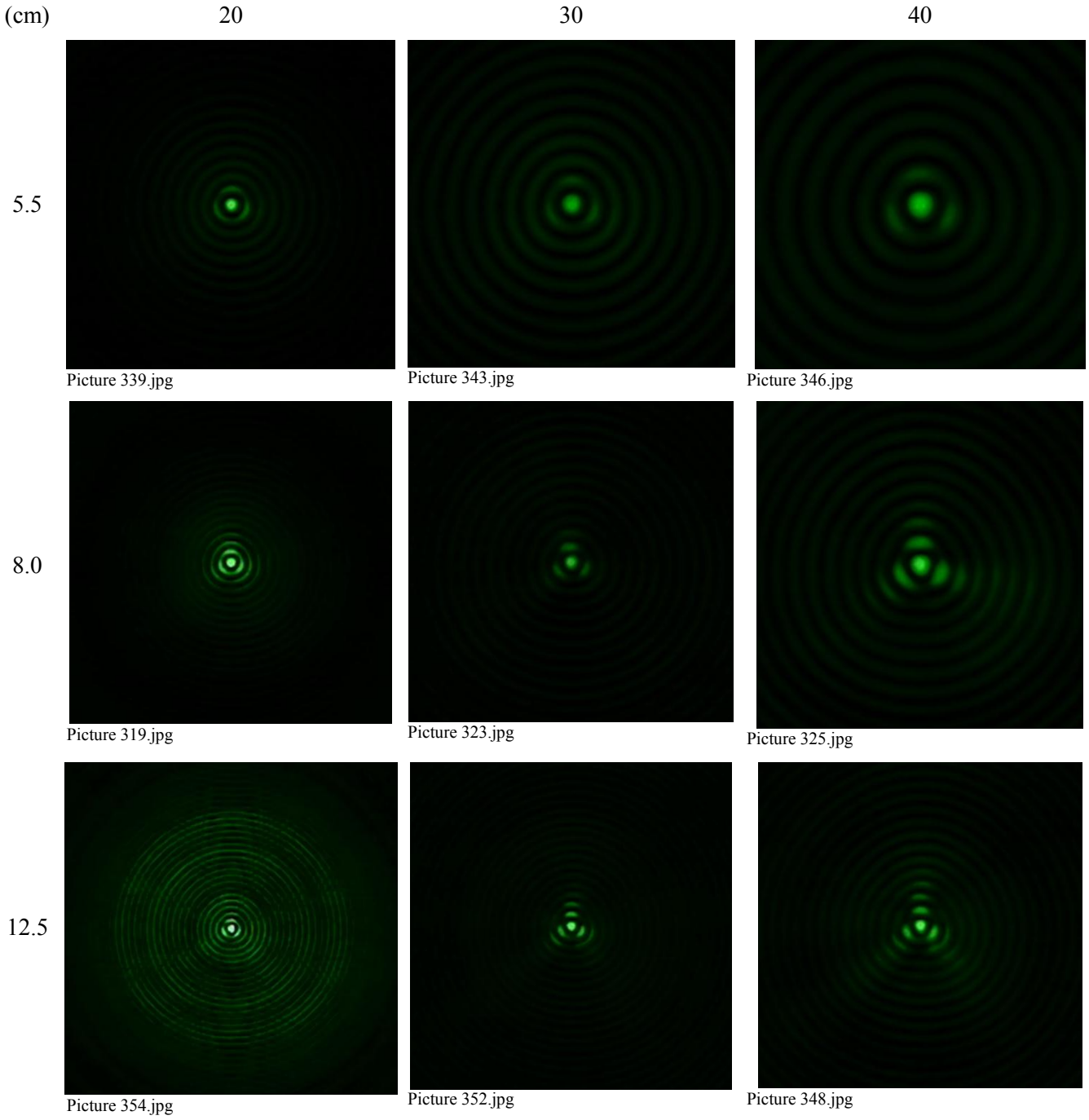

Figure 4.7: Measured Point Spread Function of 5° fraxicon.

Figure 4.8 shows PSF plots for images in figure 4.7 are son the previous page. These are representative of the same distances for $\mathbf{X_1}$ and $\mathbf{X_2}$ from the axicon images in the previous set.

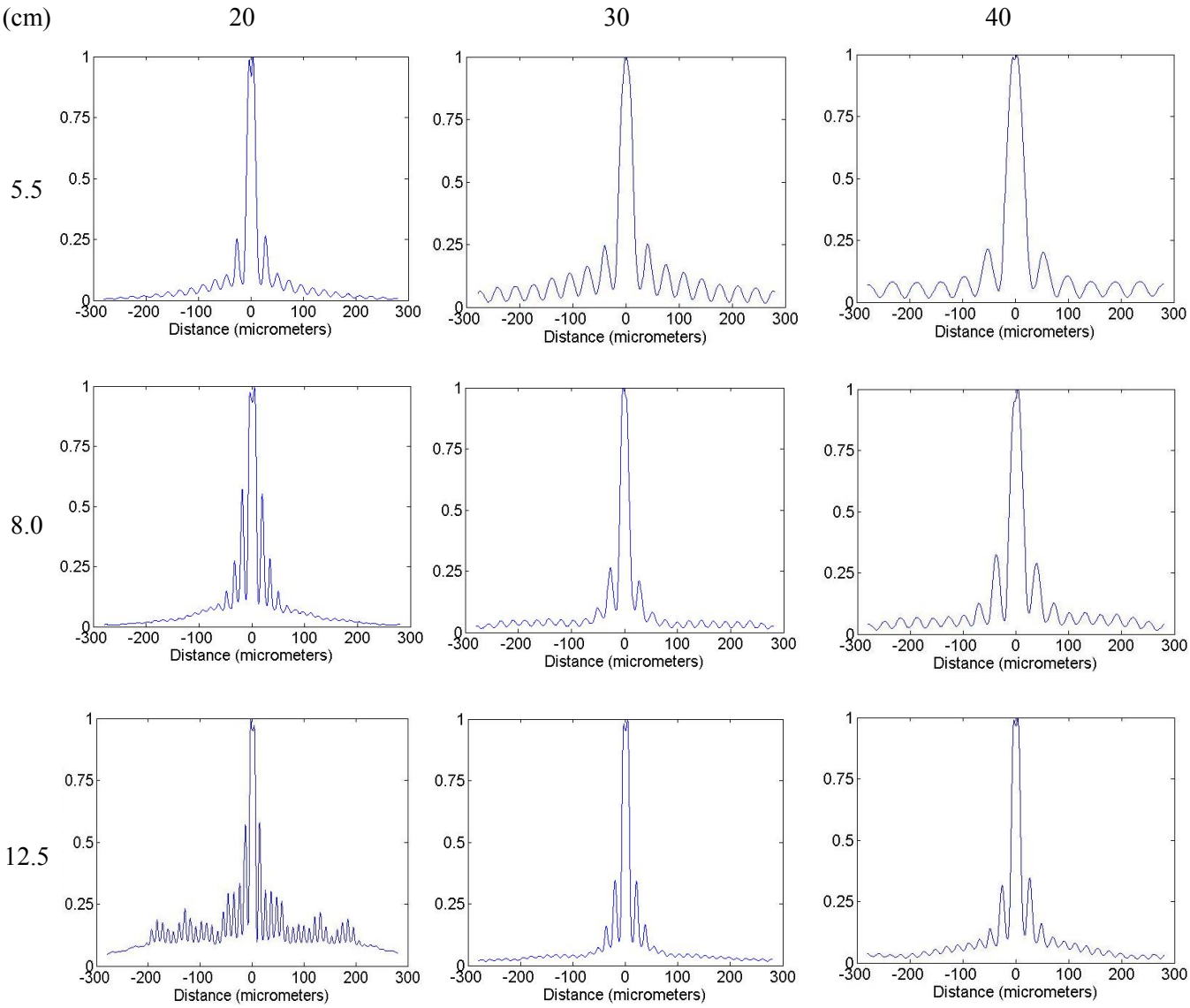

Figure 4.8: Point Spread Function plots for 5° fraxicon.

4.2.4 Logaxicon

The logarithmic axicon (logaxicon) is fundamentally different from the axicon and fraxicon in that it has more in common with an aspheric lens in so far as its shape is concerned. It is similar to an axicon in that it focuses light along a focal line rather than to a point. The purpose of the logarithmic axicon is to distribute the incoming light energy evenly along the optical axis over a set line of focus of length **L**, as shown in Figure 4.9. The curvature of this aspheric lens is specifically tailored to achieve this goal. For example, the logaxicon lens used to produce the PSF images that follow has the equivalent of a focal length spanning from 5 to 15 cm.

Consider a ring of light with a radius **r** about the optical axis and a thickness d**r** passing through a logaxicon (see Figure 4.9). For the purpose of this description, it is assumed that the incident light field is of constant intensity and a plane wave. The amount of light energy in such a ring is proportional to its radius. This means that in order to maintain a constant intensity along the focal line, rings of incoming light are more tightly spaced/imaged along the focal line for small values of **r** and the spacing spreads out along said line as **r** increases. This means that the curvature of a logaxicon is changing as a function of **r**. In other words the angle at any given point along the radius is a function of the radius itself.

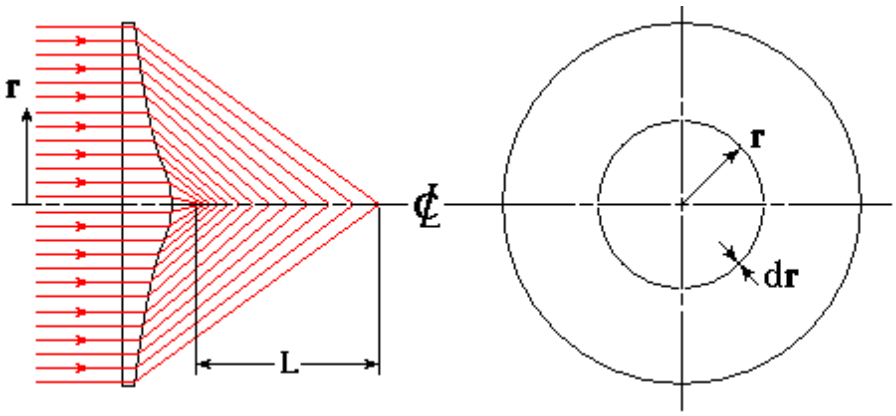

Figure 4.9: Focusing of a collimated light beam by a logarithmic axicon.

Since the logaxicon is an aspheric lens, it is more closely related to a conventional spherical lens than a standard axicon. This is particularly true near the center of a logaxicon since the light energy in this area is focused very tightly, close to a point in fact. This characteristic of the logaxicon would suggest that the image quality may be better than for conventional axicons, and fraxicons.

The PSF images of the logaxicon are shown in Figure 4.10. Since this optical element is of particular interest, a broader set of measurements were taken.

The image at $\mathbf{X_1}$ = 14.5 cm and $\mathbf{X_2}$ = 5.5 cm (the image in the lower left hand corner) is of particular interest. The likelihood is that this image falls outside of the focal range, in this case too close to the logarithmic axicon. Since the point at which the focal line begins has not yet been reached, light has not converged to the optical axis. The light ring around the dark central region is approaching the optical axis but has yet to reach it. This will happen further away from the lens.

The refractive logarithmic axicon has been studied in a previous paper by Golub et al. (2010). Of note is the alternating intensity of the interference ring patterns of the logarithmic axicon's PSF which is clearly visible in the image of the PSF but not mentioned in the paper. This same phenomenon is visible in PSFs acquired for this thesis.

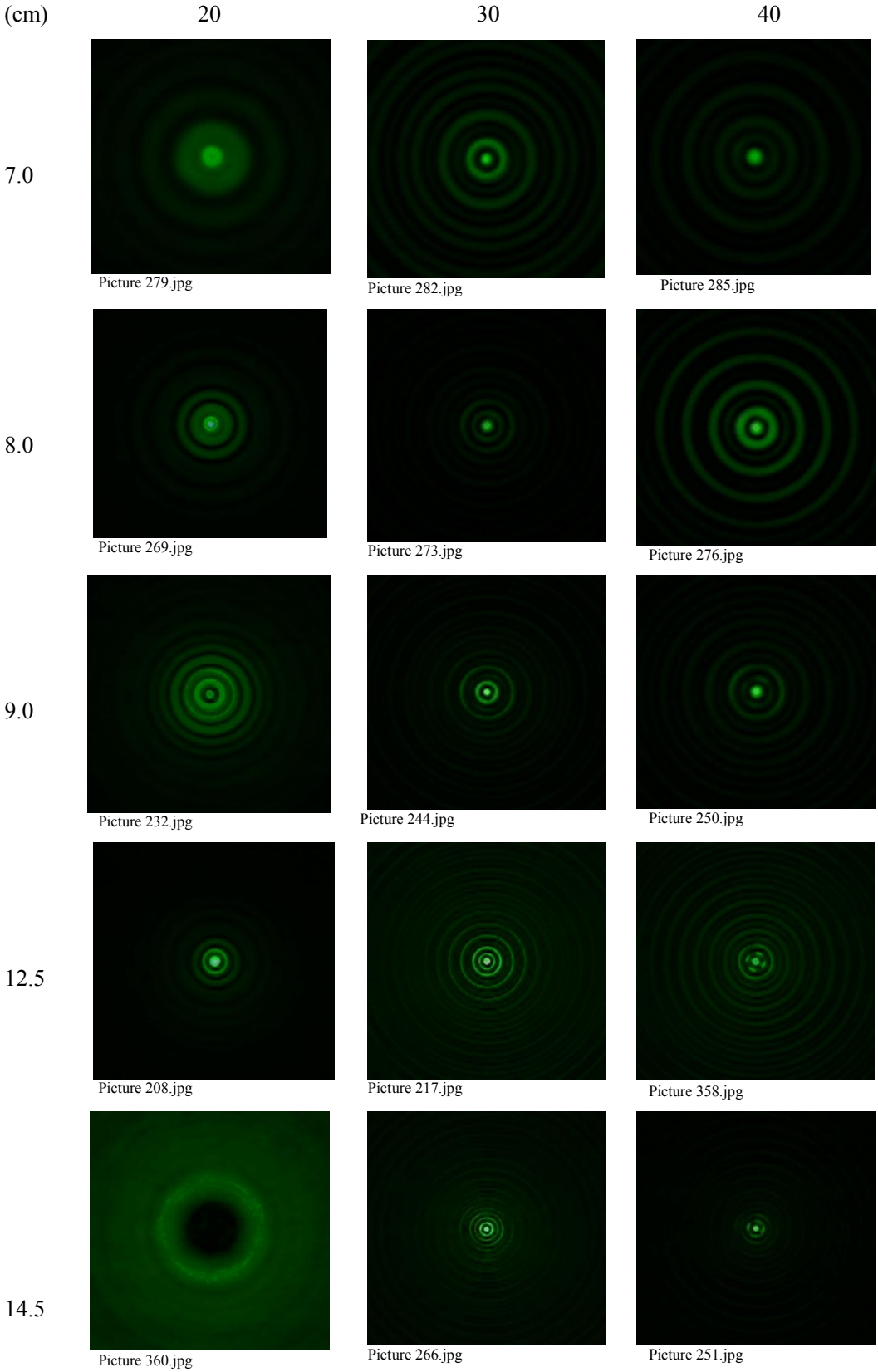

Figure 4.10: Measured Point Spread Function for logarithmic axicon.

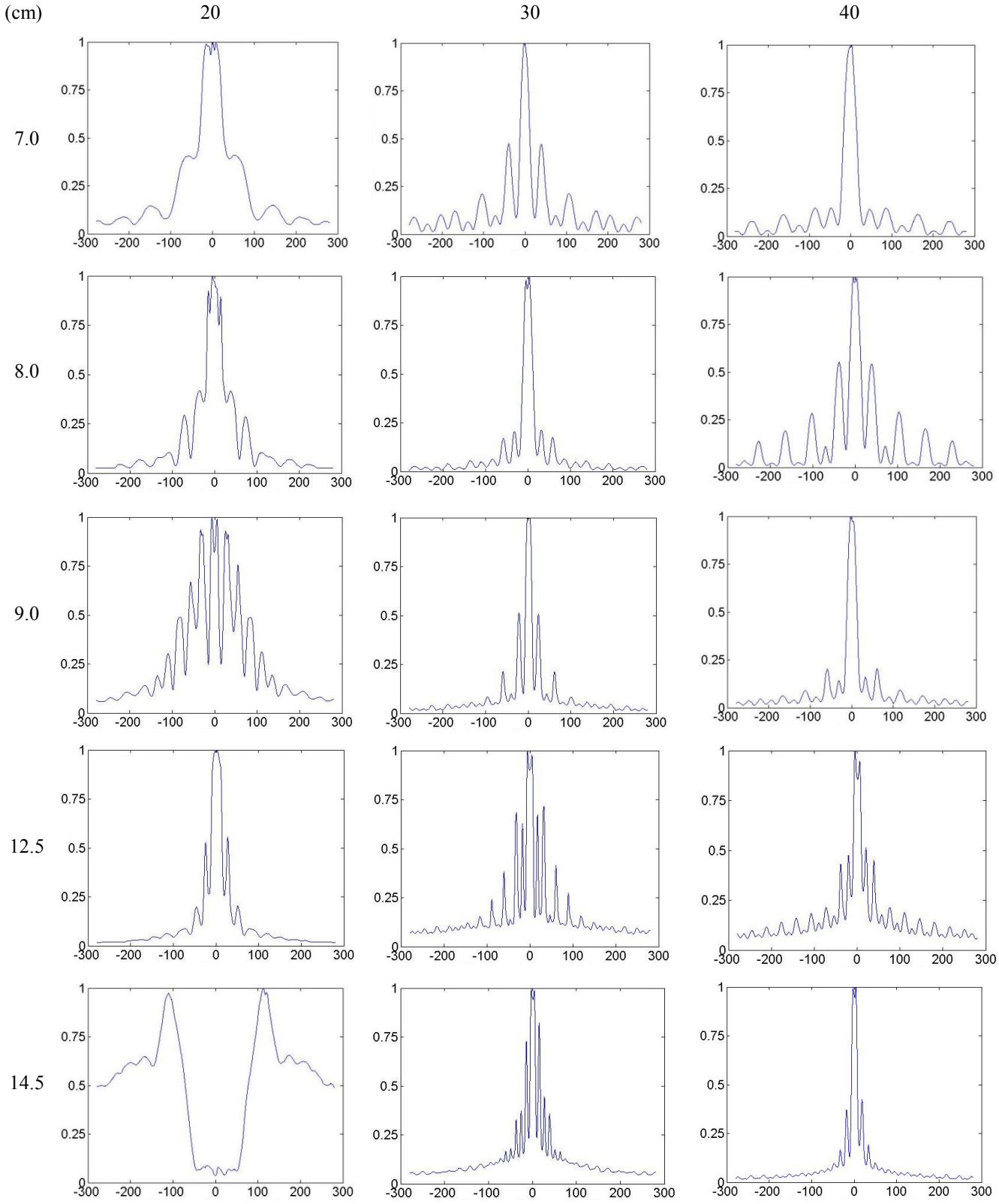

Figure 4.11: Point Spread Function plots for logaxicon corresponding to images in Figure 4.10.

Corresponding PSF plots for images on the previous page. The horizontal axis is in micrometers and the vertical axis is a normalised intensity (maximum intensity = 1, black = 0). Table columns (20, 30 and 40 cm) are distance from object to image and rows (7, 8, 9, 12.5 and 14.5 cm) are the distance from the object to the lens.

The image 'Picture 360.jpg' was actually taken at 21.5 cm (instead of 20). This was done because the center of the image is hollow (no light at the center inside of that distance). This is a characteristic of the logarithmic axicons since the lens does not focus/image to a point.

4.3 Use of Axicons to Capture Images

A setup shown in Figure 4.12 was used to capture images of a United States Air Force (USAF) pattern. This particular test pattern has a minimum feature size of 14.3 line pairs per millimeter. The images were taken with the axicon, the fraxicon and the logaxicon at the same locations where the PSF images were taken in order to use the PSFs for post-processing of the images.

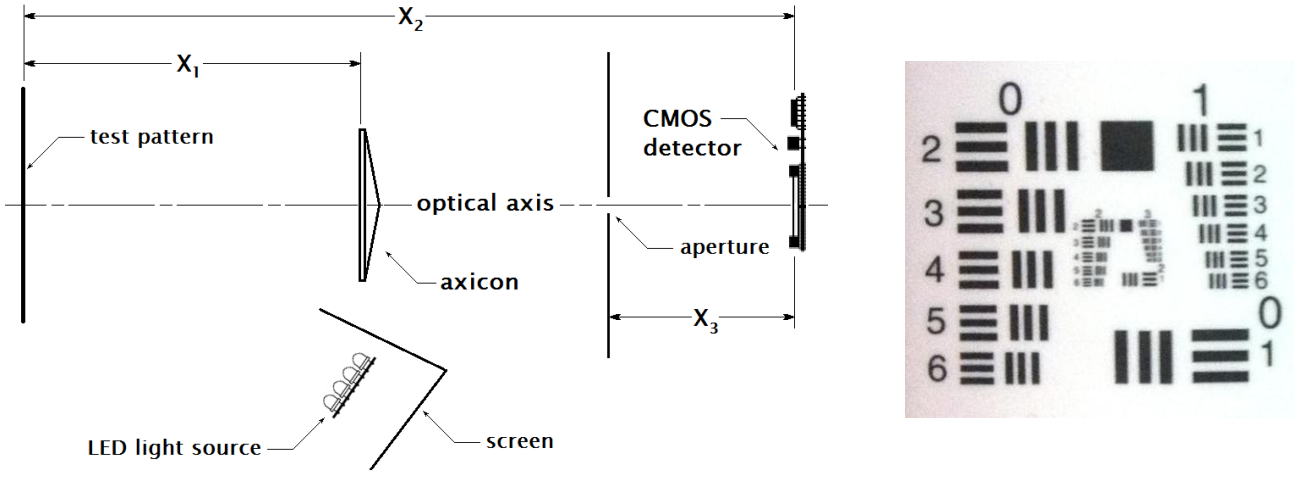

Figure 4.12: Left: Image capture test bench setup. Right: 1951 USAF test pattern image (groups 0-3)

The initial PSFs and images captured used the distances provided in Table 4.1. These PSFs and images were used initially, in the formative phase, to develop a consistent image processing technique.

A second set of images for the USAF was taken using the 5^o axicon, the 5^o fraxicon, a 10^o axicon and the logarithmic axicon for more demanding (close up) values of **p** and fixed values of **q** as might be seen in an actual camera system. Table 4.2 shows the values of **p** and **q** for these measurements. A large number of PSFs and corresponding images were taken and their processing will be discussed in the next chapter. These images are not included here as they are displayed for comparison purposes in chapter 5.

Optical element	Image distance **q**	Object distance **p**
Axicon ($\alpha=5^o$)	20 mm	20 mm, 30 mm, 40 mm, 60 mm, 80 mm, 100 mm, 150 mm, 200 mm, 300 mm, 500 mm, 700 mm, 900 mm.
	70 mm	175 mm, 215 mm, 355 mm, 655 mm.
Fraxicon ($\alpha=5^o$)	20 mm	20 mm, 30 mm, 40 mm, 60 mm, 80 mm, 100 mm, 150 mm, 200 mm, 300 mm, 500 mm, 700 mm, 900 mm.
	70 mm	175 mm, 215 mm, 355 mm, 655 mm.
Axicon ($\alpha=10^o$)	20 mm	20 mm, 30 mm, 40 mm, 50 mm, 60 mm, 80 mm, 100 mm, 150 mm, 200 mm, 300 mm, 500 mm, 700 mm, 900 mm.
	70 mm	175 mm, 215 mm, 355 mm, 655 mm.
Logaxicon	70 mm	175 mm, 215 mm, 355 mm, 655 mm.

Table 4.2: Values of p and q for second set of image measurements.

4.4 Additional Observations

The limitation of the CMOS sensor (in terms of saturation) has implications with respect to the PSF plots. As a result, the laser output was attenuated using one or two polarizing filters depending on whether or not the laser output was polarized.

Another observable issue was noise resulting from residual images. This noise was an issue in the early stages of image collection but was dealt with by capturing images under no light conditions in an effort to flush the previous images. In order to verify that residual noise had been flushed out, subsequent images with no input were checked by looking for pixels with non-zero intensity. If none existed, it was assumed that the residual noise had been removed sufficiently so as not to impact subsequent images. Adjusting the sensitivity to ensure these residual images did not manifest themselves in later images was also effective. Also, it makes sense to reduce the CMOS detector's exposure to light sources to a minimum between readings (at the very least, it is unlikely to have done any harm).

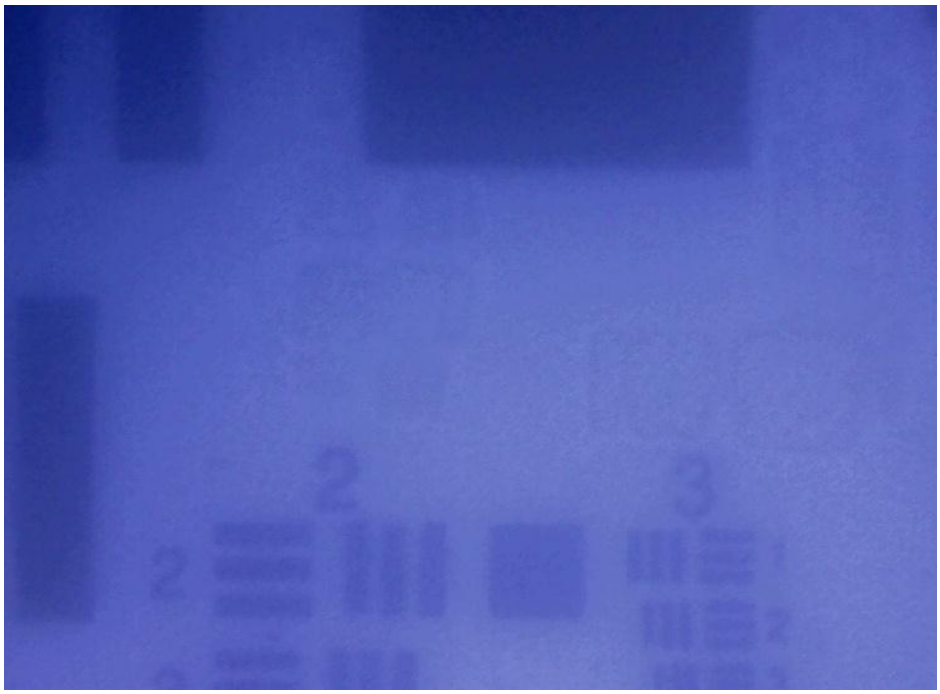

Figure 4.13: Residual image noise can be seen in this image (just above and to the left of center for example).

Later, green light was used to produce both the PSF (543 nm) and illuminate (532 nm) the USAF test pattern image. This appeared to resolve the issue, but no efforts were made to investigate this issue further.

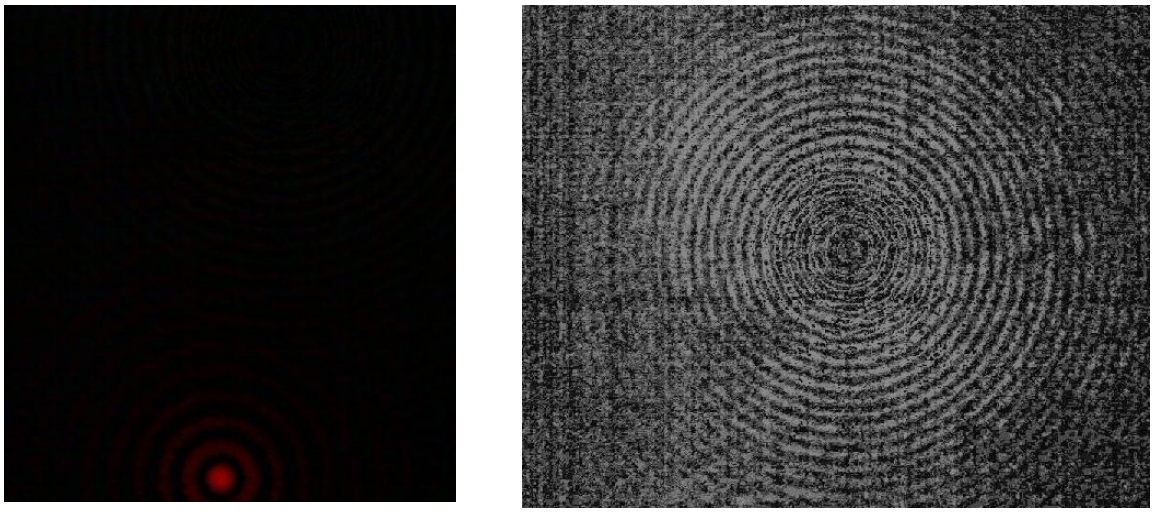

(a) **(b)**

Figure 4.14:
a) Residual image seen in upper half of image. Lower portion (in red) is desired image.
b) Enlarged residual image from upper half of fig. 4.14a enhanced using histogram equalization

Chapter V

ANALYSIS

In this chapter various techniques are applied in an effort to improve the quality of the images of the USAF test pattern reported in Chapter 4. The PSF measurements, which serve to characterise the impulse response of these optical elements, provide a basis for image restoration. It is preferable that a uniform process be applied here. Additionally, an ideal process should not be computationally intensive. Ideally, it should also not require human intervention. To this end a number of techniques are explored.

Initially, a process was developed using the first set of USAF images reported in Table 4.1. The approach first experimented with in section 5.1 is later refined and formalized. In section 5.2, this 'formalized' process is applied to the second set of images reported in Table 4.2. These latter images are produced with the object nearer to the lens thereby filling a void in the existing literature. For this later work an equation derived to predict the intensity field of a divergent beam (Roy and Tremblay, 1980), was adapted to calculate the PSF.

For the case of the logaxicon, which does not have a fixed angle β, a trial and error approach was applied to achieve the best possible result.

5.1 Processing of the First Set of Images

5.1.1 Deconvolving an Image with the Degradation Function

A Wiener filter, which is implemented in the MatLab® image processing toolbox, by way of the function deconvwnr can be used to de-convolve an image. The function as applied here, takes the following form:

`deconvwnr(I,PSFN,NSR)` where `I` is the image,

`PSFN` is the normalised point spread function

`NSR` is the noise to signal ratio of the image

In order to apply this function, the image in question is first imported and converted to a greyscale double precision two dimensional array. Similarly, the image used to generate the PSF array is converted to a greyscale double precision 2D array.

Figure 5.1:
Greyscale representation of PSF

The PSF describes the manner in which a point of light from the object plane is distorted by the optical system. More specifically, for the purposes of this discussion, it is demonstrative of how a point of light that, under ideal circumstances, should illuminate only a single pixel in an imaging sensor (the imaging plane) is actually distributed amongst neighbouring pixels. If we assume that the total energy from this source is to be accounted for in the resulting image, then the sum of the values in each element of the PSF array must add up to a value no greater than that of the source. Since in almost any real passive

system, some signal is lost, one must assume that the sum of all these elements will actually be less than that of the source.

The actual PSF images, once captured and converted to greyscale, store in each element of the image array an integer value that varies from zero (no light) to 255 (white light or saturation). In order to make use of the PSF as a filter that can be used in the **deconvwnr** function, the array must first be normalized. Simply put, take a summation of all elements in the PSF array and divide each element in the PSF by the summation of all its elements. The result is an array whose elements, if summed, equal 1. The end result is a degradation function that should not change the total light energy of the image it is meant to restore. Though not entirely accurate, this is the goal.

The last term in the `deconvwnr` command is the noise to signal ratio (NSR). For the purposes of the work done here, a trial and error method was used to establish the value to be applied. The NSR is not only dependent on the noise in the image, but also the noise levels in the PSF in order to generate an appropriate value. A value determined using trial and error, once established, need only be carried out a single time for any given opto-electronic system. The value determined for the NSR that returned the best results was approximately 0.12.

5.1.2 Processing of Axicon (5^o) Images

Image: Axicon, X1 = 18.7cm, X2-X1 = 4.5cm (Picture 59.jpg)

For this case, the measured point spread function was initially used to correct the image, fig. 5.2(b). The results were poor, most probably due to the poor quality PSF. An average of 4 exposures (to reduce random noise) with adaptive histogram equalization produced a significantly sharper image, fig. 5.2(c).

The measured PSF did include sufficient information to create a Bessel function with equivalent periodicity, fig. 5.2(d). It was decided that this should be used to generate a synthetic PSF, fig. 5.2(c). The results of the two could then be compared. A sharpening filter, as described in Chi and George (2001), was also applied, fig. 5.2(f), and is compared here, fig. 5.3(f).

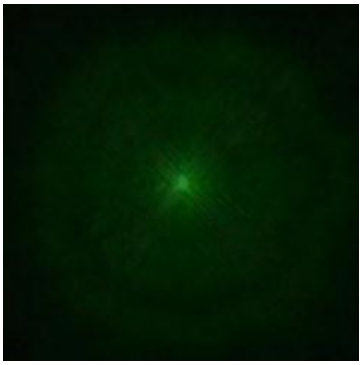

(a)

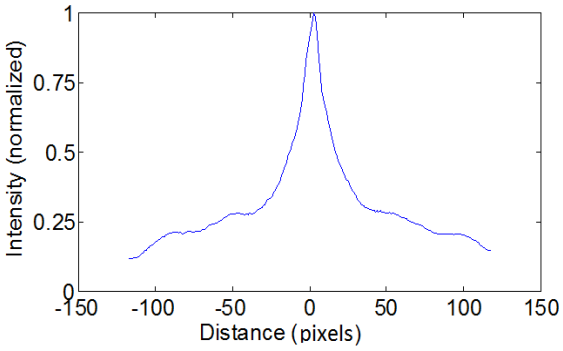

(b)

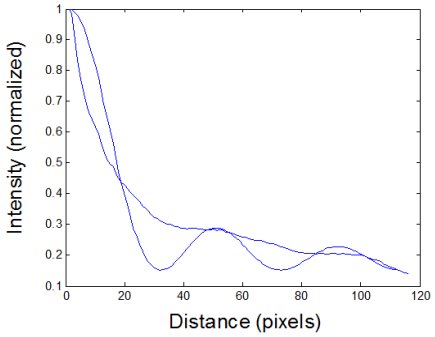

(c)

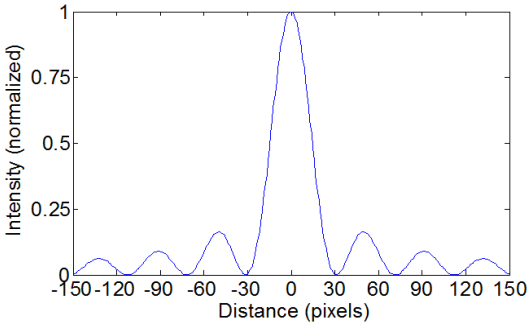

(d)

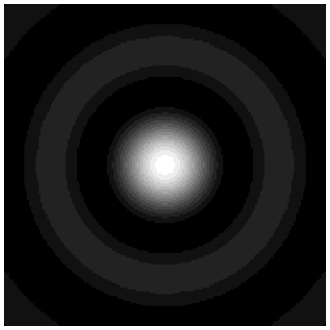

(e)

```
>> I=im2double(rgb2gray(imread('P470\
Picture 56.jpg')));

>> h=[0 -1 0;-1 6 -1;0 -1 0] %sharpening filter

h =

 0   -1    0
-1    6   -1
 0   -1    0

>> Is=imfilter(I,h);

>> imshow(Is,'initialmagnification',100,
'border','tight')
```

(f)

Figure 5.2: *a) Original PSF (green -543 nm point source). b) Plot of adjacent PSF. c) Modified Bessel based function overlaid with measured PSF. d) Bessel with equivalent period to measured PSF. e) Revolved Bessel function, 281 pixels square (intensity x 2000 for viewing purposes). f) Matlab commands used to apply sharpening filter.*

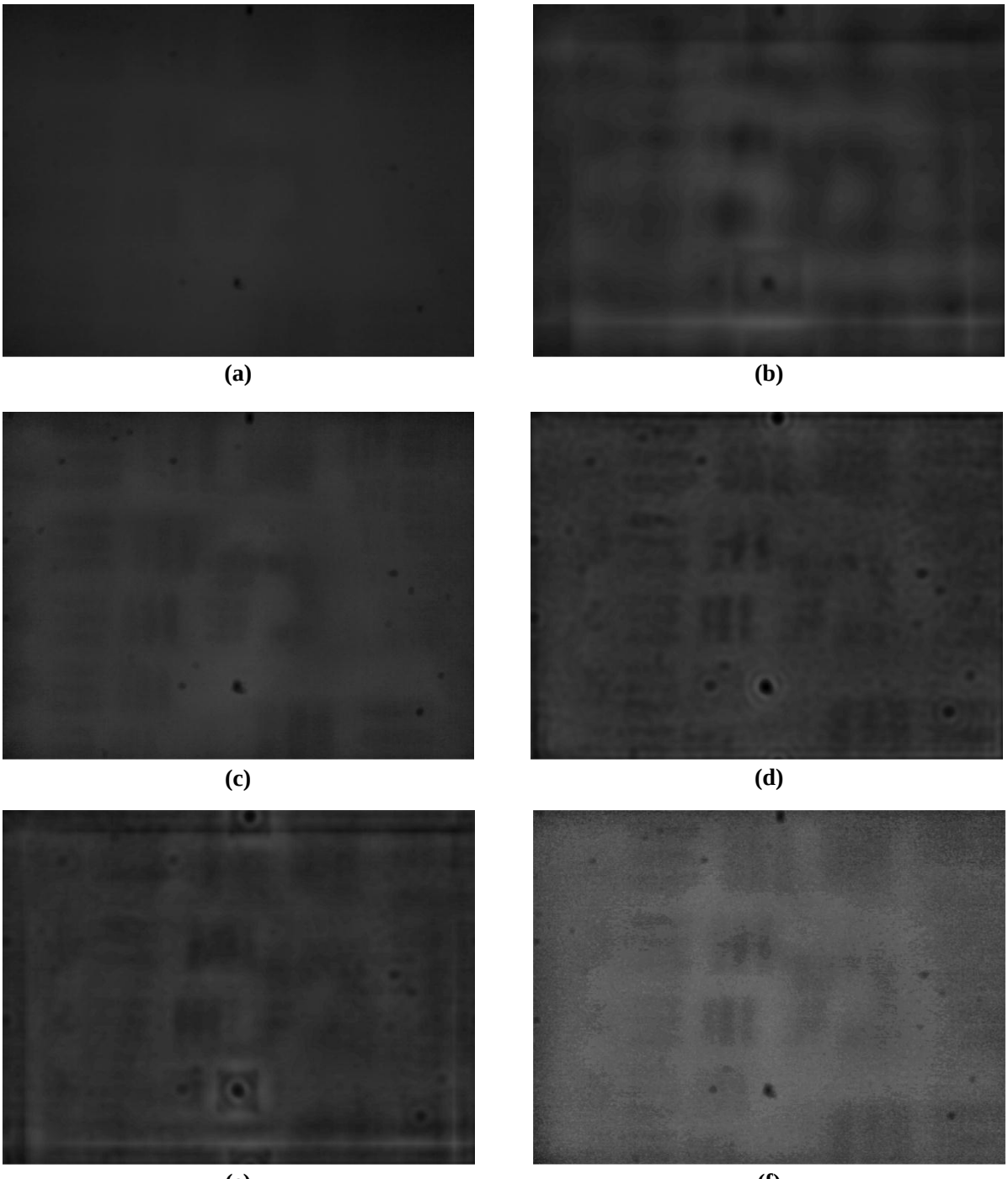

(a) **(b)**

(c) **(d)**

(e) **(f)**

Figure 5.3: *a) Greyscale of original image. b) Deconvolution using measured PSF + AHE c) Average with adaptive histogram equalization. d) Deconvolution using revolved Bessel + AHE. e) Deconvolution using revolved modified Bessel + AHE. f) MatLab Image filtering (imfilter) with sharpening filter.*

Initially, in order to produce a PSF from a Bessel function, a vector was created in MatLab® which was then populated with the data points generated by the Bessel function. The number of

elements in the vector was dependent on the desired mask size. The Bessel function inputs were chosen to generate a plot that best matched the periodicity of the measured PSF. The vector was revolved so as to populate a two dimensional array which, once normalized, served as a synthetic PSF. The normalising process involved summing all elements in the array and then dividing each element by the sum, the sum of all elements in the final PSF array should sum to unity to conserve the light energy in the system.

Comparing the various methods used to improve image quality, it can be seen that the measured PSF is of insufficient quality to produce a sharper image. It in effect produces the opposite result, further blurring the image. It should be added that the very poor contrast of the original image used required adaptive histogram equalization.

The simple averaging technique, fig. 5.3(c), though effective in reducing random noise, requires that a series of identical images be captured. This may not be practical and does not result in any significant increase in image sharpness in of itself. It should be noted however that averaging does not suffer from the blotchiness which results from the Wiener deconvolution method adjacent to it, fig. 5.3(d). Also, the more delicate structures to the upper right hand side of the image are preserved and enhanced with averaging. This is not the case for any of the other techniques shown here.

It is clear that the Bessel function, fig. 5.2(d), produces a better result than do the measured PSF, fig. 5.2(b), or the modified Bessel function, fig. 5.2(c). The sharpening filter enhanced image, fig. 5.3(f), had an effect similar to the Bessel function enhanced image, fig. 5.3(d).

The resolution limit can be calculated using the following expression from Druart et al. (2008):

$$v_{USAF} = (L/f) \times 2^{\text{group} + (\text{element} - 1)/6} \quad \textbf{(5.1)}$$

Where v_{USAF} is the system resolution limit in line pairs / millimeter, L is the object distance, f is the image distance and group and element refer to the groups and elements in the USAF test pattern. Using the image from fig. 5.3c, the resolution limit is approximately 10.5 lp/mm. This is the best resolution limit for this series of images.

Image: Axicon, X1 = 18.7cm, X2-X1 = 13cm (Picture 410.jpg).

A similar analysis to the one performed for the image with X1 = 18.7cm, X2-X1 = 4.5cm was followed in this case and the results are shown in Figures 5.4 and 5.5.

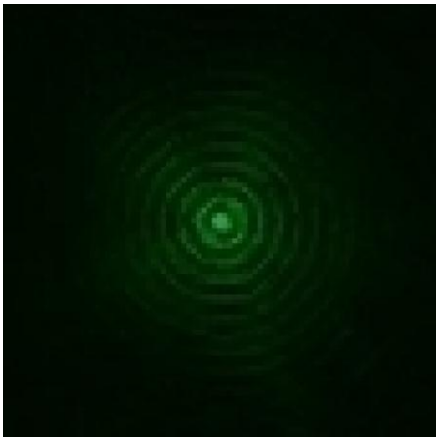

(a)

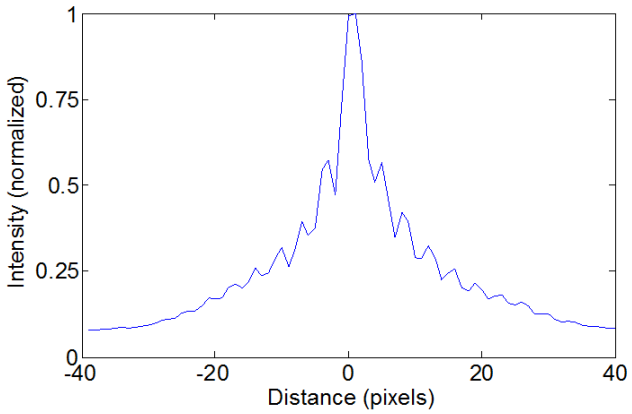

(b)

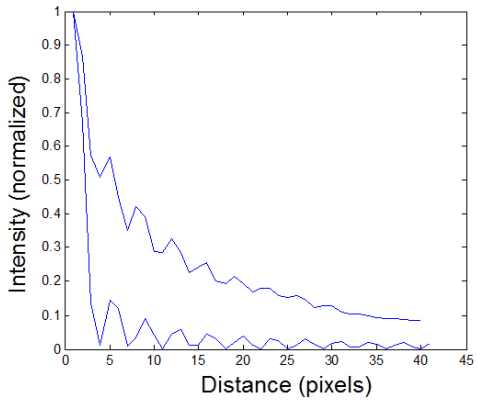

(c)

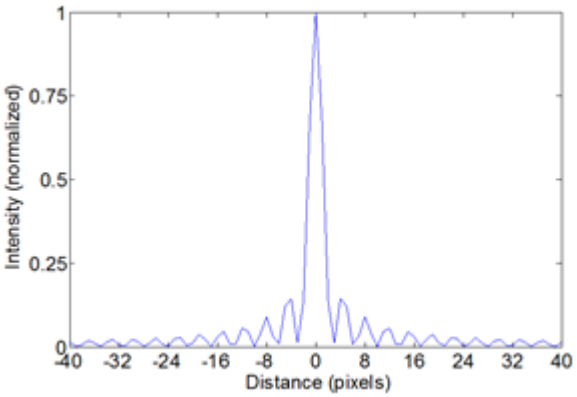

(d)

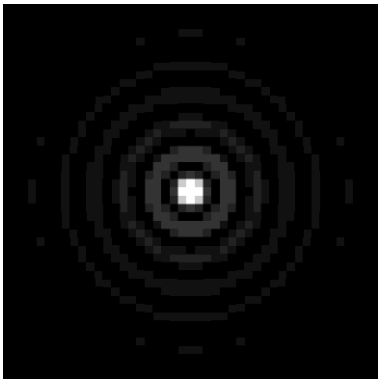

(e)

```
>> I=im2double(rgb2gray(imread('P410\Picture
410.jpg')));>> h=[0 -1 0;-1 6 -1;0 -1 0] %sharpening
filter

h =

     0    -1     0

    -1     6    -1

     0    -1     0

>> Is=imfilter(I,h);

>>
imshow(Is,'initialmagnification',100,'border','tight')
```

(f)

Figure 5.4*: a) Measured PSF b) Plot of adjacent PSF c) Generating a Bessel function with the same periodicity (intensity x 100 for viewing purposes d) Bessel with equivalent period to measured PSF e) Revolved Bessel function,81 pixels square f) Sharpening filter and commands used to generate image*

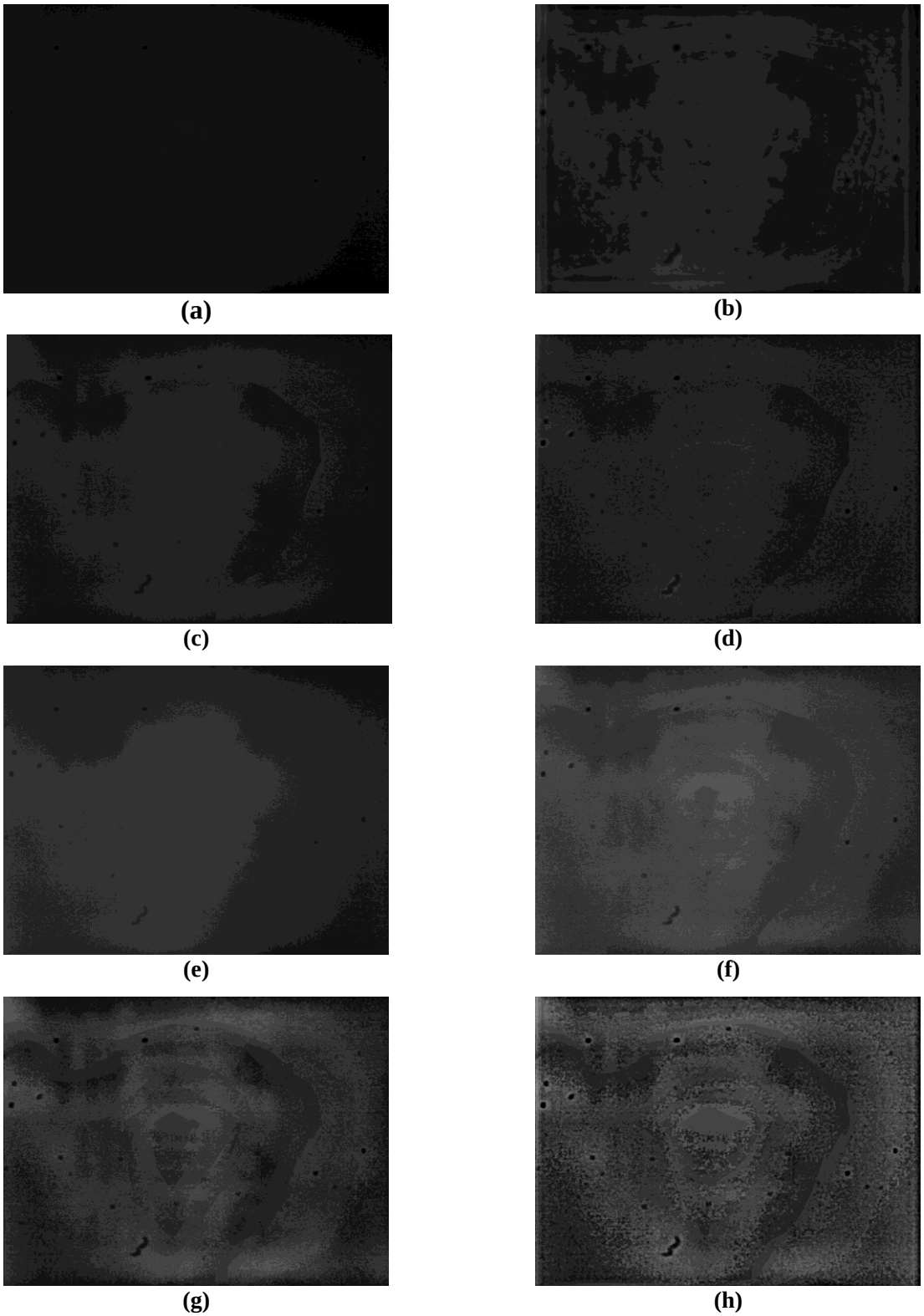

Figure 5.5: *a) Greyscale of original image b) Deconvolution using measured PSF + AHE c) Greyscale after adaptive histogram equalization d) Deconvolution using revolved Bessel + AHE e) MatLab Image filtering with sharpening filter f) MatLab Image filtering with sharpening filter + AHE g) Original greyscale + AHE × 2 (AHE carried out twice) h) Deconvolution using revolved Bessel + AHE × 2*

5.1.3 Processing of Fraxicon (5^o) Images

Image: Fraxicon, X1=19cm, X2-X1=4.9cm (Picture 59.jpg)

As was the case with the conventional axicon under similar circumstances (X1=18.7cm, X2-X1=4.5cm), the measured PSF was poor and produced poor results as can be seen in the table below. It was possible, just as with the axicon, to produce a substitute PSF directly from a Bessel function. The resulting de-convolution using this synthetic PSF was superior to that produced with the measured PSF and similar to that produced with the sharpening filter.

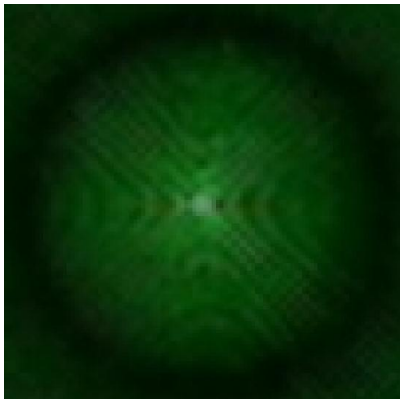

(a)

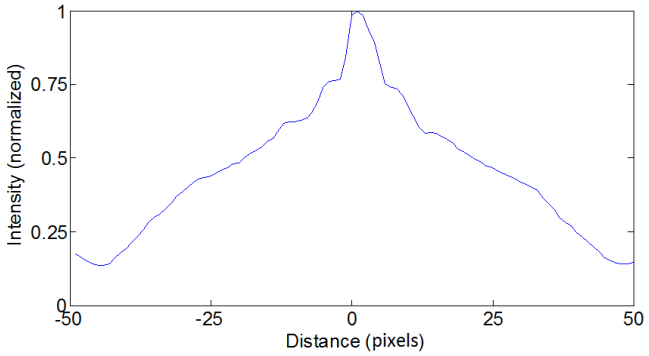

(b)

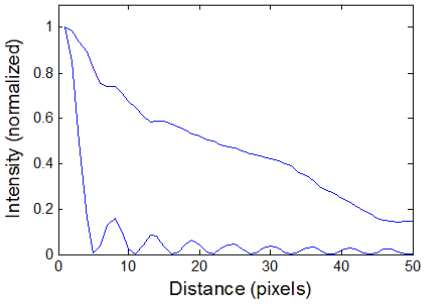

(c)

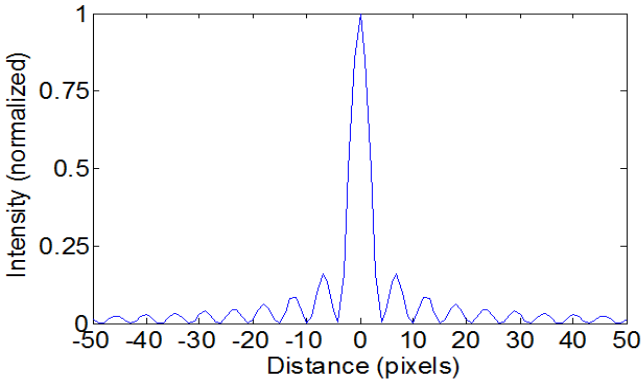

(d)

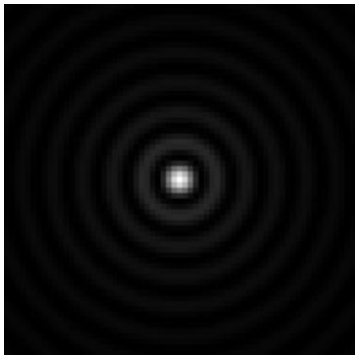

(e)

Figure 5.6:
a) Image of point of light as degraded by optical system (PSF) b) Plot of point spread function (PSF)
c) Modified Bessel and measured PSF
d) Bessel with equivalent period to measured PSF
e) Revolved Bessel function, 131 pixels square (intensity x *128) for viewing purpose*

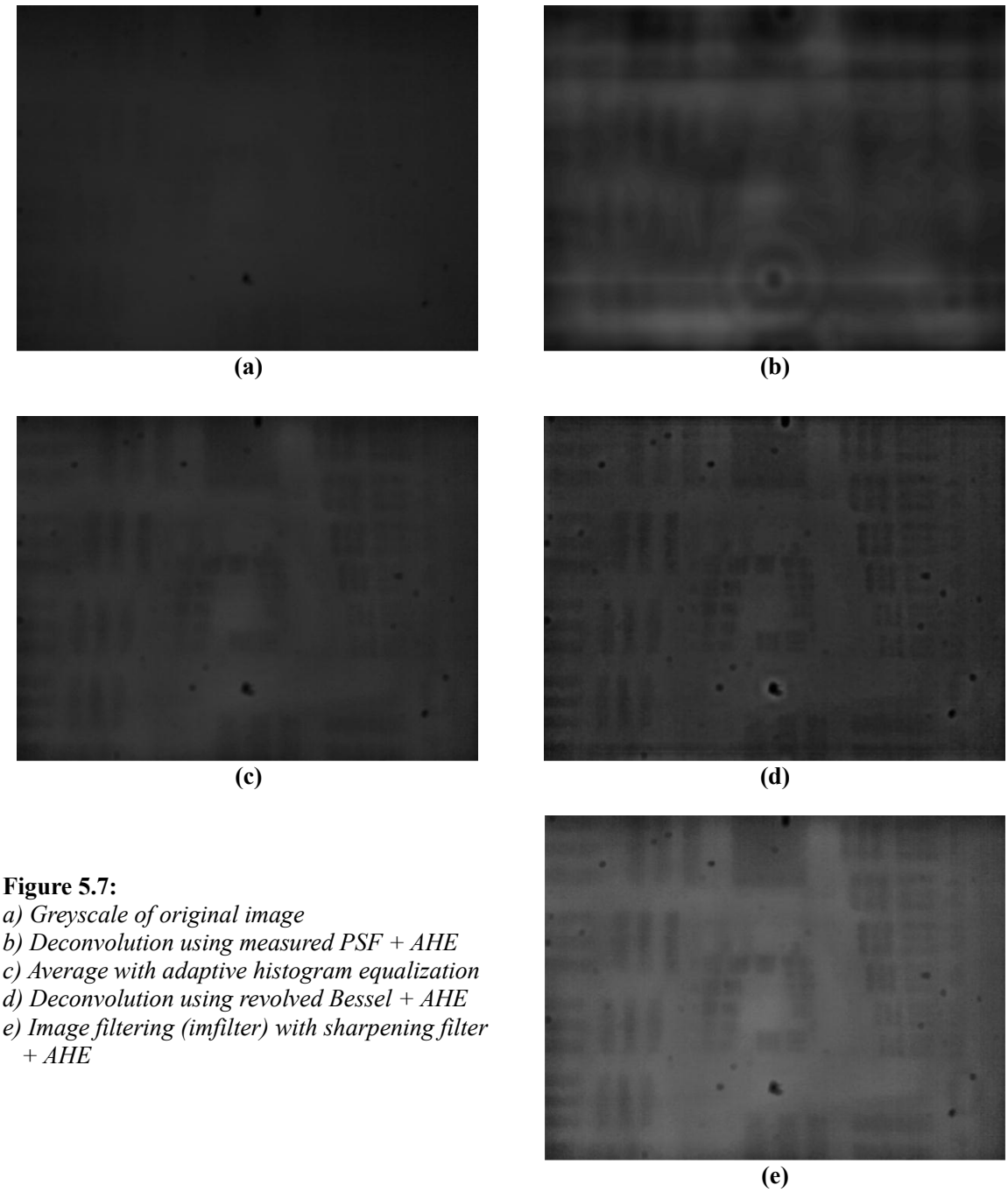

(a) **(b)** **(c)** **(d)** **(e)**

Figure 5.7:
a) Greyscale of original image
b) Deconvolution using measured PSF + AHE
c) Average with adaptive histogram equalization
d) Deconvolution using revolved Bessel + AHE
e) Image filtering (imfilter) with sharpening filter + AHE

The best resolution limit for the images in fig. 5.7 is approximately 17.5 lp/mm, for images (d) and (e).

Image: Fraxicon, X1 = 19.0cm, X2-X1 = 16.4cm (Picture 413.jpg)

A similar analysis to the one performed for the image with X1 = 19cm, X2-X1 = 4.9cm was followed in this case and the results are shown in Figures 5.8 and 5.9.

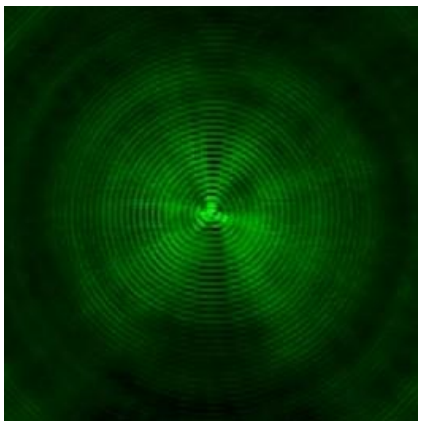

(a)

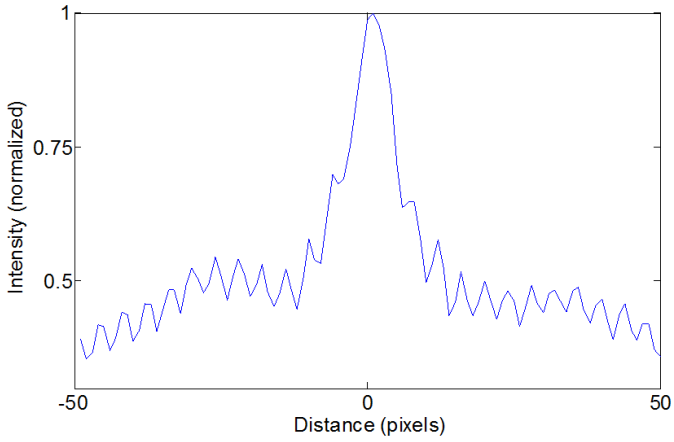

(b)

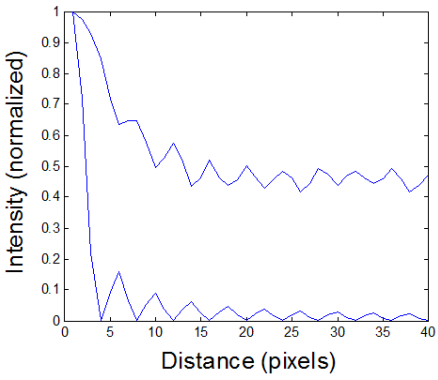

(c)

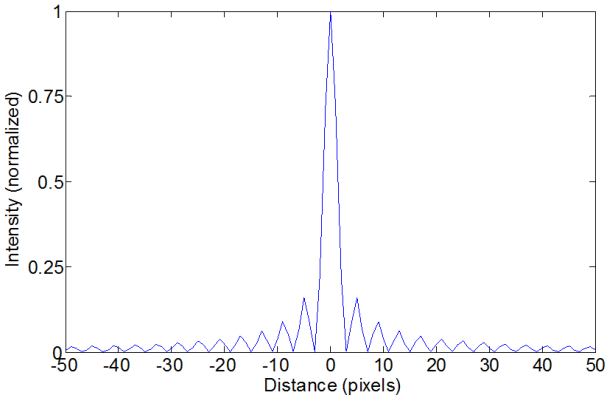

(d)

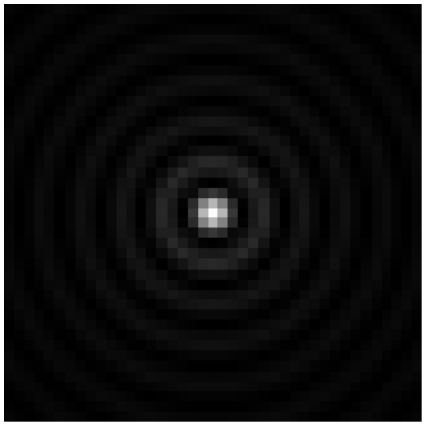

(e)

Figure 5.8:
a) Image of point of light as degraded by optical system (PSF) b) Plot of point spread function (PSF)
c) Modified Bessel and measured PSF
d) Bessel with equivalent period to measured PSF
e) Revolved Bessel function, 131 pixels square (intensity x *128 for viewing purpose)*

(a)

(b)

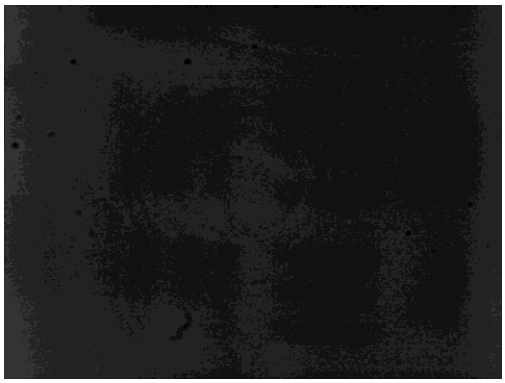

(c)

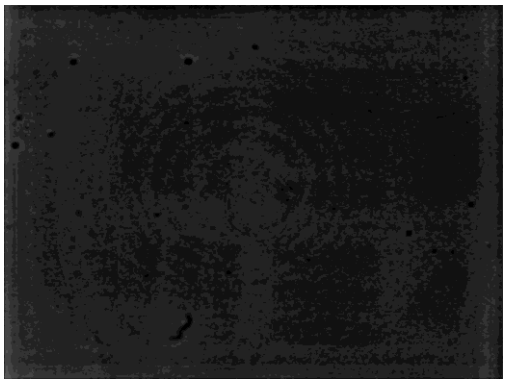

(d)

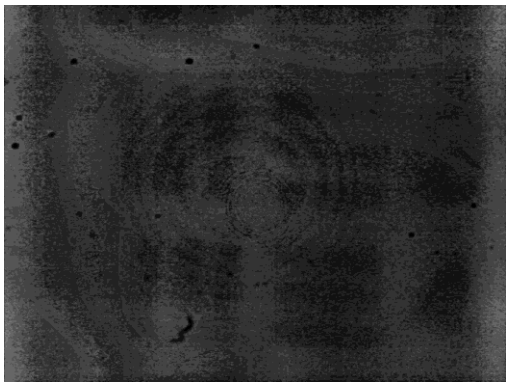

(e)

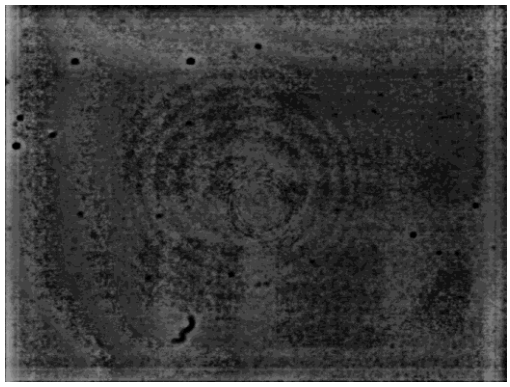

(f)

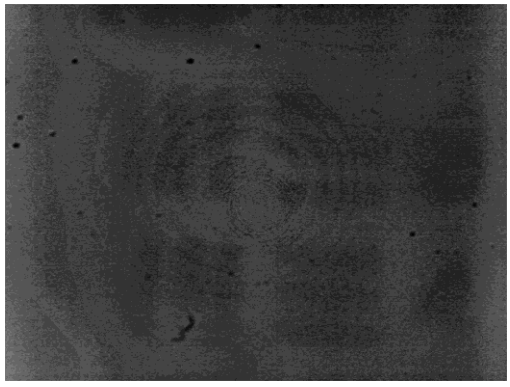

(g)

Figure 5.9:
a) Greyscale of original image
b) Deconvolution using measured PSF + AHE
c) greyscale + adaptive histogram equalization
d) Deconvolution using revolved Bessel + AHE
e) Greyscale + AHE x *2*
f) Deconvolution using revolved Bessel + AHE x *2*
g) Image filtering (imfilter) with sharpening filter + AHE

5.1.4 Processing of Logaxicon Images

The logaxicon produces superior images to conventional axicons. This is evident in the images that follow. The aspheric nature of this optical element reduces the distance (along the z-axis) over which the optical energy is dispersed. The end result is better image quality along the optical axis within a prescribed focal range. Additionally, this element, being designed to produce the same optical power at any point along the z-axis within its prescribed range, produces a more consistent quality of image over said range.

Recall from chapter 4 (4.2.3) that the PSF produced by a logaxicon though ‘Bessel like’ has an additional feature: the rings alternate in terms of brightness as they emanate outward from the center. This is in addition to a gradual reduction in intensity (as is the case for the Bessel function). As a result, it was decided that an averaged version of the original PSF be used for Wiener deconvolution.

Image: LogAxicon, X1=20cm, X2-X1=6.2cm (Picture 391.jpg)

For X_1 = 20 cm, X_2-X_1 = 6.2 cm produces the sharpest possible image. The greyscale of the image produced at this distance is shown in fig. 5.10(a).

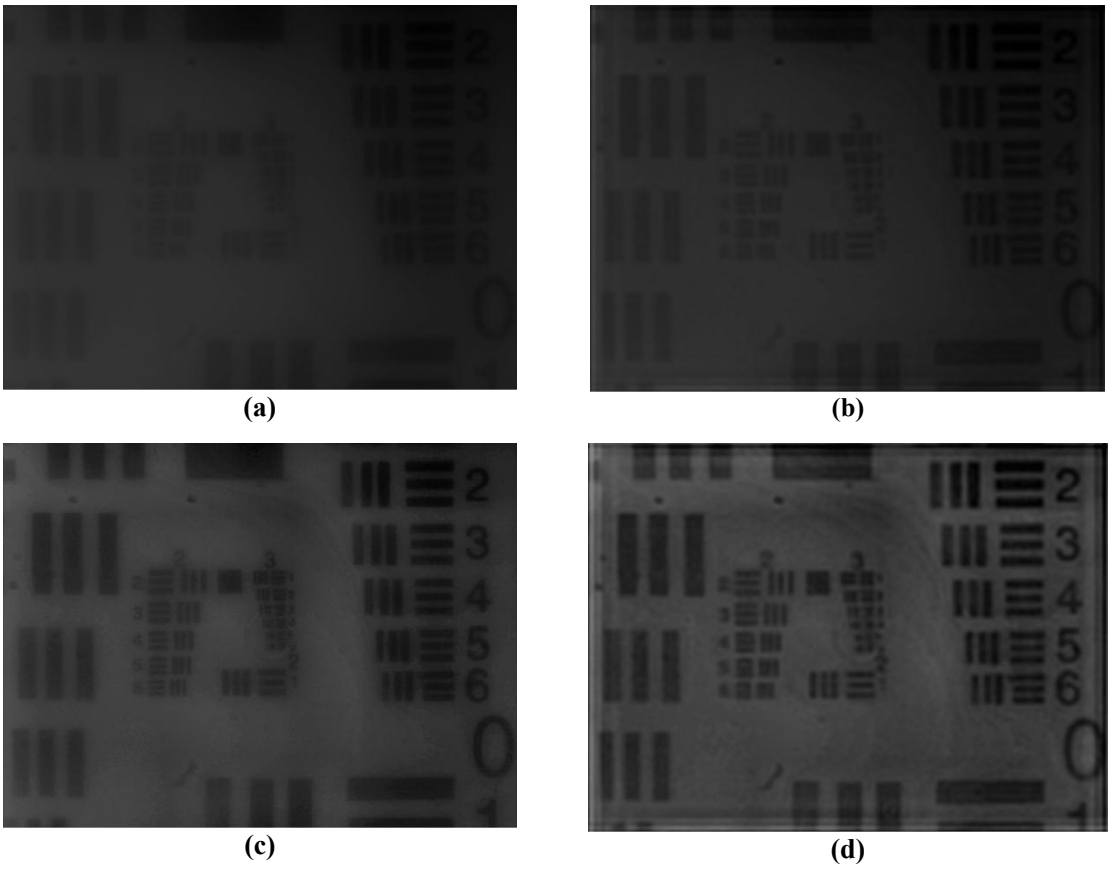

(a) **(b)** **(c)** **(d)**

Figure 5.10:
a) Original greyscale image (Picture 391.jpg) b) After deconvolution is applied
c) AHE applied to original greyscale d) After deconvolution and AHE

At first glance, the deconvolved image, fig. 5.10(d) has the best contrast giving the impression of a better image. A closer look, as can be seen in fig. 5.11, is more revealing.

Calculations for fig. 5.10(c) produce a resolution limit of approximately 35-40 lp/mm without Wiener Deconvolution, noticeably better than with (fig. 5.10(d)) at approximately 20 lp/mm.

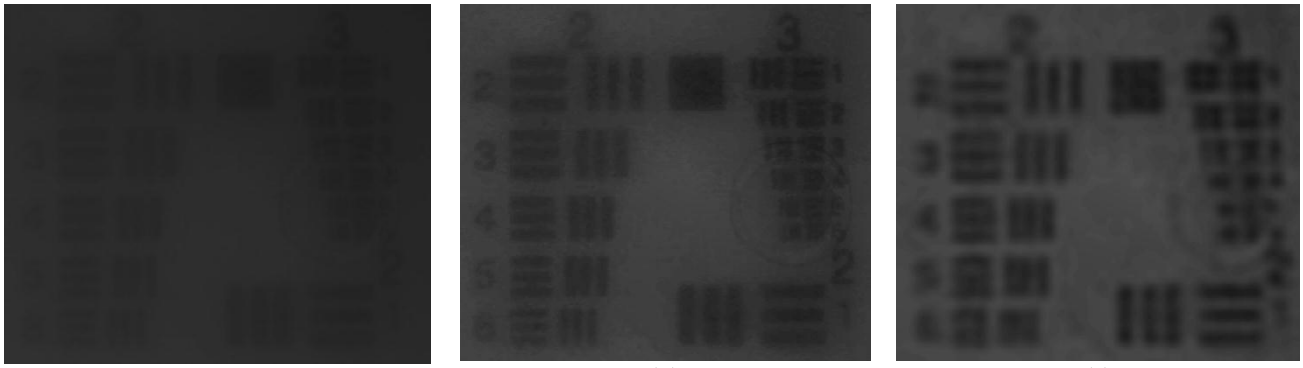

(a) **(b)** **(c)**

Figure 5.11: *a) Section of original image b) AHE only c) Deconvolution followed by AHE*

Although the Wiener deconvolution improves the contrast of this image, the relative sharpness achieved using this axicon is not improved through its use here. Applying it in fact reduces the image sharpness. In terms of sharpness, applying adaptive histogram equalization alone produces a better result in this particular case.

Image: LogAxicon, X1=20cm, X2-X1=5.5cm (Picture 401.jpg)

The effect of varying the noise to signal ratio (NSR) in the Wiener Deconvolution function can be seen in this instance, see fig. 5.12. The best value can be determined through trial and error. The exact value to use can be somewhat subjective however.

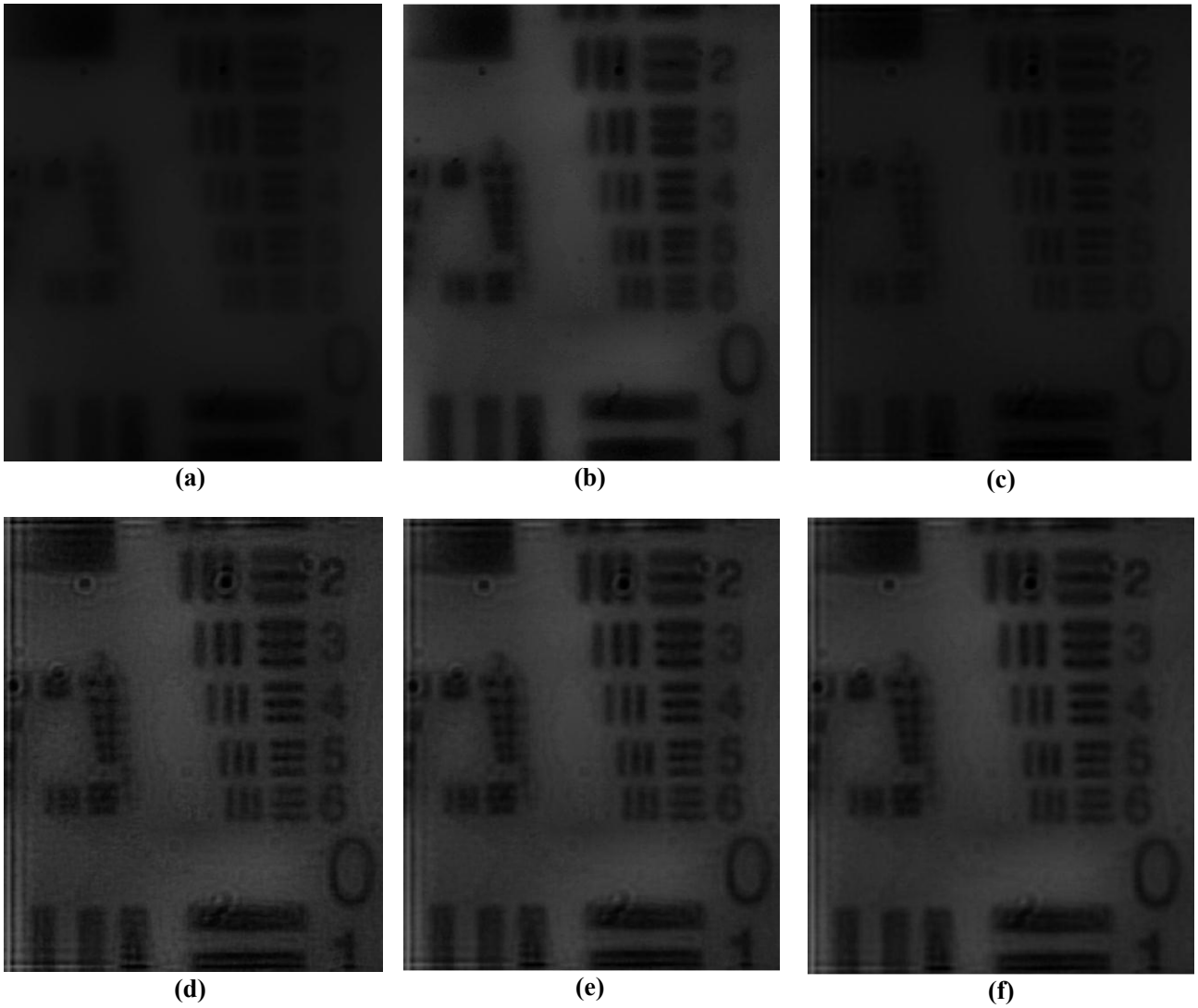

Figure 5.12: *a) Original greyscale image b) after AHE c) After deconvolution using measured PSF (NSR=0.035) d) after deconvolution using measured PSF (NSR=0.02) + AHE e) after deconvolution using measured PSF (NSR=0.035) + AHE f) after deconvolution using measured PSF (NSR=0.05) + AHE*

Image: LogAxicon, X1=14cm, X2-X1=8cm (Picture 409.jpg)

For this case, the extent of the PSF used is shown to have an effect on the degree to which the image is improved. As one might expect, using a larger range of the PSF, one that more completely accounts for the total point source energy should produce a higher quality image. This occurs at the cost of additional computational resources. The benefit also diminishes with PSFs of ever increasing completeness. If the PSF produced is not an experimental one, it may diverge from the ideal solution at some point and begin to have a detrimental effect on the image.

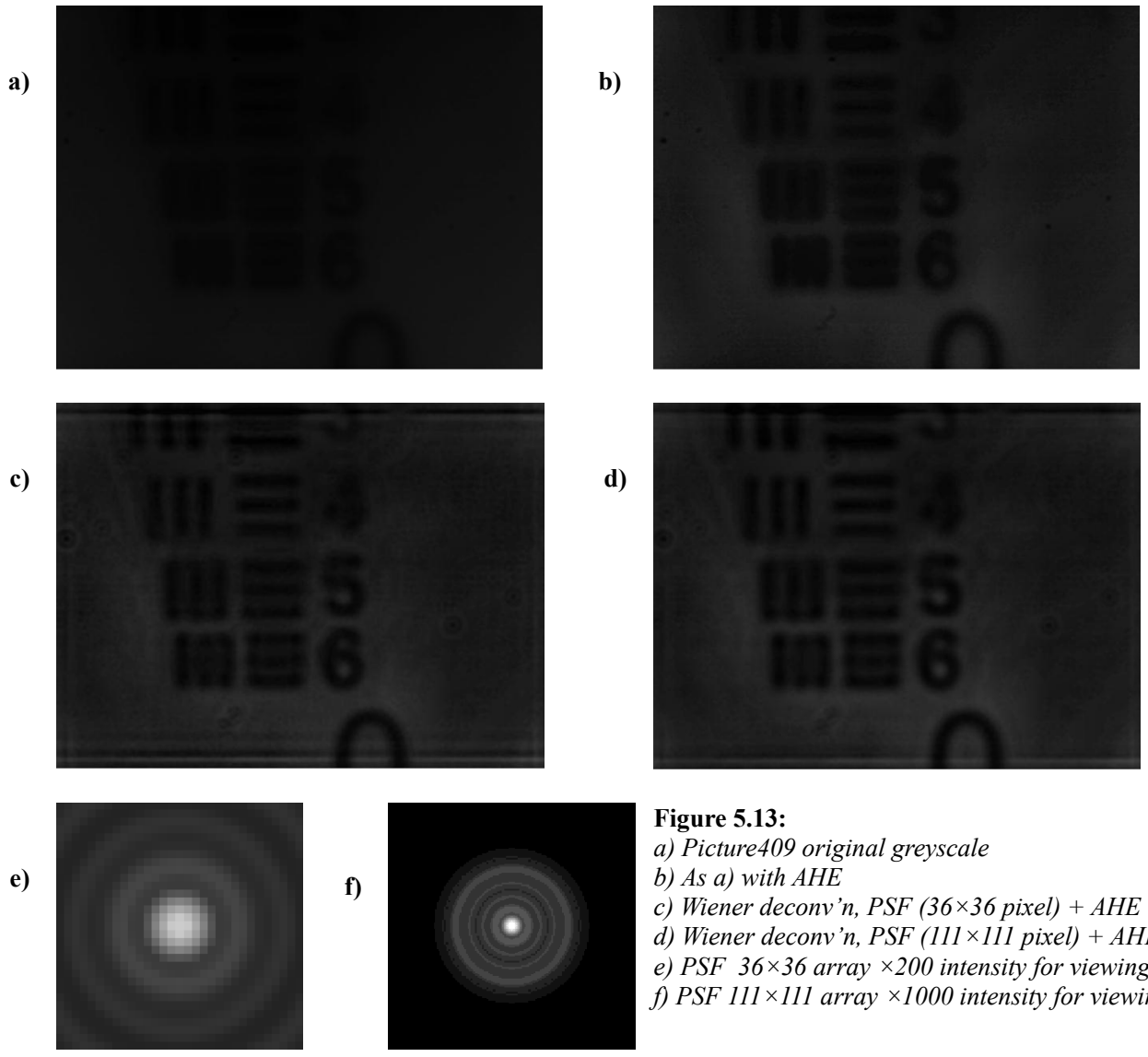

Figure 5.13:
a) Picture409 original greyscale
b) As a) with AHE
c) Wiener deconv'n, PSF (36×36 pixel) + AHE
d) Wiener deconv'n, PSF (111×111 pixel) + AHE
e) PSF 36×36 array ×200 intensity for viewing
f) PSF 111×111 array ×1000 intensity for viewing

5.1.5 Reduction of Random Noise by Averaging

By taking multiple exposures of an image, it is possible to reduce random noise. Since each exposure will have slight variations in the value of each pixel, creating a new image made up of the average value of each pixel acquired over several exposures can reduce random noise significantly. The results of this technique are demonstrated in fig. 5.14 c), d).

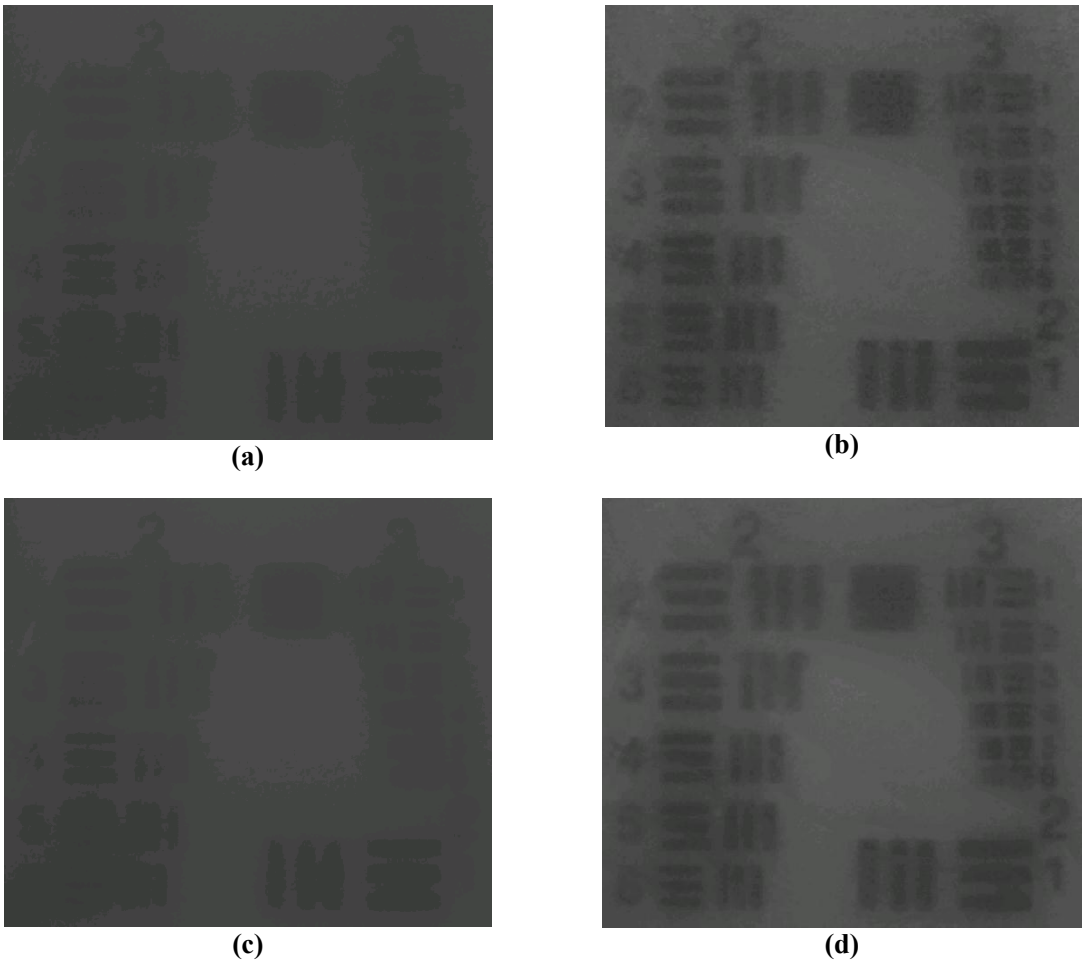

Figure 5.14:
a) Greyscale image section prior to processing b) Same section of 'Picture 24.jpg' after adapthisteq, c) Average of four images d) Same section of average of four after adapthisteq

The fig. a,b,c,d are 240 x 240 pixel sections of a 1600 x 1200 image of USAF test pattern image.

The complete enhanced image is shown in fig. 5.15. The image used is an average of four images to reduce random noise.

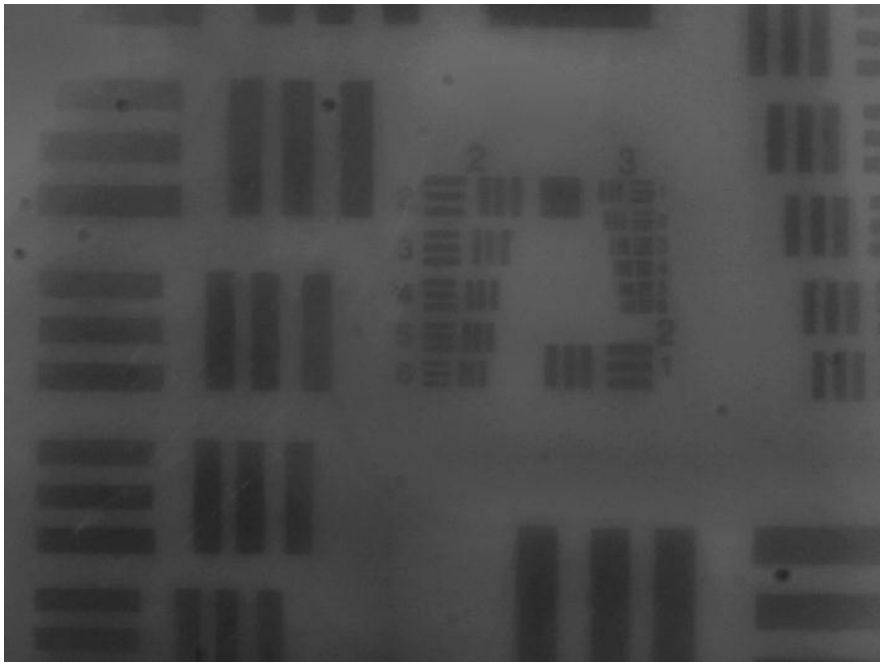

Figure 5.15: Average of 4 images captured with logaxicon (Picture 24, 25, 26, and 27) and AHE applied.

Based on the different trials of image processing performed, the optimum procedure determined was to perform a Wiener deconvolution followed by an adaptive histogram equalization.

5.2 Imaging of Second Set of Images

Prior work in the study of extended depth of field includes a number of efforts. Many of these are described in chapter 3. They are repeated here for the benefit of the reader. In some instances additional information is added to demonstrate the need to carry out the experimental work described in this section.

Results for both a light sword optical element (LSOE) and a linear diffractive axicon (Mikula et al., 2005): one with a depth of field extending from approximately 1108 mm from the element to about 1354 mm and the second one with a depth of field extending from 985 mm from the element to 1477 mm. They compared the results to those of a Fresnel lens having a focal distance limited by the center of the DOF of the above element which is equal to 1231 mm. They took images of an object placed at a distance p = 3,000 mm at planes at distances q = 1782, 1922, 2087, 2283 and 2520 mm corresponding to a defocusing parameter $w_{20} = \left(\frac{D^2}{8}\right)\left(\frac{1}{p} + \frac{1}{q} - \frac{1}{f}\right)$ equal to $2\lambda, 1\lambda, 0\lambda, -1\lambda, -2\lambda$.

Mikula et al. (2007) compared the imaging properties of a diffractive forward logarithmic axicon, an axilens which is a holographic lens with extended depth of field, and a diffractive LSOE. The forward logarithmic axicon and axilens have radial modulation of the phase transmittance while the LOSE has angular modulation. They present images and modulation transfer functions (MTFs) at a series of object distances p ranging from 250 to 2000 mm and an imaging plane at a fixed distance **q** = 20 mm from the optical element. The results suggest that the LSOE with its angular modulation produces images and MTFs that are far less affected by position along the optical axis. In a subsequent paper Garcia et al.(2008), which included

members involved in the above work manufactured and tested the imaging properties of a refractive LSOE which does not suffer from the strong chromatic aberrations associated with diffractive LSOE. In this latter work, the nearest object distance was no less than 525 mm.

Druart et al. (2008) used a diffractive axicon as a single element telescope. A two-step process by digitally processing axicon-captured images to restore/deblur the images has been suggested. The paper describes how the element can be translated along the optical axis to zoom in on an object and remain in focus. Three images were taken. The first two with the object at 3 m from the diffractive axicon, one with the imaging surface at 88 mm and the other at 37 mm. A comparison of the first two images demonstrated the zooming capability of the system. The third image was taken at a distance of 1.3 m from the object to the diffractive element and 37 mm from the element to the imaging surface. This third image combined with the second image mentioned demonstrates the invariance of the cut-off frequency along the focal line (invariance in MTFs for these images). In order to restore the contrast in these images, a high pass filter was used.

Zhai et al. (2009) developed an optical system comprised of a spherical lens, an axicon with a base angle equal to 0.01 radians (approx. 0.57^{o}) and a CCD camera. The images captured by this system are then processed using a Wiener filter. The author does mention an overall drop in image quality compared to an axicon free system while in focus, but, adds that with the axicon (and digital image processing), the system is less sensitive to defocus.

In instances where the object is nearer to the lens, $\mathbf{p} \leq 100$ mm, the results from the literature are scarce. In order to establish the suitability of an axicon or one of its derivatives for use in instruments in this range, a series of images were collected and image processing was applied. In order to simplify the approach to image processing, Wiener deconvolution is used. In section 5.1,

a zero order Bessel function replaced the measured PSF where it was unusable. The further an object being imaged is from the focusing lens, the closer the rays of light are to being parallel to the optical axis. However, the Bessel function used to generate a synthetic PSF is a far less accurate approximation for objects being imaged closer to the focusing lens.

For the second set of measurements, where the object distance **p** is between 20 and 100 mm from the lens, the PSF was calculated using an equation that describes the intensity distribution of a divergent laser source passed through an axicon (Roy and Tremblay, 1980).

$$I(r,z) = \frac{W}{2}\frac{a^2}{\omega^2}k\left(\left(\frac{1}{z}+\frac{1}{z'}+\frac{1}{R_i}\right)^{-1}\right)J_0^2\left(\frac{kra}{z}\rho_0\right)\frac{{\rho_0}^2}{z^2}\exp\left(-\frac{2a^2}{\omega^2}\rho_0\right) \quad \textbf{(5.2)}$$

Where

$$\rho_0 = \frac{(n-1)tan\,\boldsymbol{\alpha}}{a}\left(\frac{1}{z}+\frac{1}{z'}+\frac{1}{R_i}\right)^{-1}$$

W can be varied to normalize the function (a peak of 1 at the origin of the dependant variable, although this was not necessary since all elements of the two dimensional revolved PSF must sum to 1), ***a*** is the radius of the axicon, ***ω*** is the width of the beam at the plane of the axicon, ***k*** is the wave number, ***r*** is the radius, ***z*** is the on axis location, ***z'*** is as defined, in fig.5.10b, and $\boldsymbol{R_i}$ is the radius of the wave. In the present case, we use the above equation to calculate the PSF. The waist $\boldsymbol{2\omega_0}$ becomes the diameter of the aperture for the point source model (fig.5.10), $\boldsymbol{z' = p}$, $\boldsymbol{z = q}$ and it can be shown that the radius of the wave can be very accurately approximated by $\boldsymbol{R_i = p}$. See Figures 5.16 a) and b) for a graphical representation.

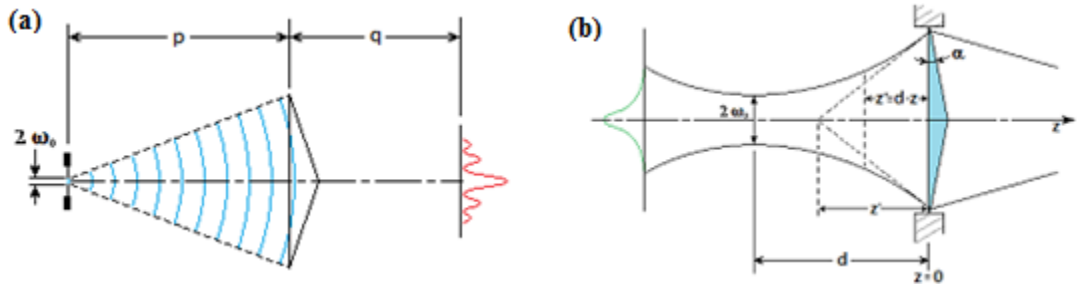

Figure 5.16: *a) **p**, **q**, and ω_0 variables in eq. 8 as adapted for a point source. b) Reproduction of original diagram from [Roy and Tremblay (1980)] for divergent Gaussian beam.*

Equation 8 produces a function that resembles a zero order Bessel function but one that compensates for the fact that it is not a plane wave incident on the axicon (point source at a finite distance). Multiplying the product within the Bessel function of equation 8 allowed for fine tuning of the period of the oscillations (varying the radius of the rings in the PSF ultimately). The period was adjusted until the best possible image processing result was reached.

5.2.1 Images Processed

For the remaining examples, axicon and fraxicon images at p = 20, 30, 40, 60, 80 and 100 mm were captured and processed.

For the logaxicon, **q** = 70 mm was used in conjunction with p = 175, 185, 215, 355 and 655 mm. These values were chosen as they fell within the constraints of the 5 to 15 cm focal length of the logaxicon. Specifically, **p** = 175 mm and **q** = 70 mm results in a focal length of 50 mm while p = 655 mm and **q** = 70 mm results in a focal length of 63.2 mm.

For all but original greyscale images, CLAHE was carried out. For images processed using Wiener deconvolution, CLAHE is carried out afterwards.

The PSFs produced using equation 8 did not produce the best results. Slight modifications to these using a scaling factor to fine tune the periodicity to better match measured PSFs resulted in improved image quality. This was true in every case, although the deviation was typically from the ideal theoretical value was very small, at least for the conventional and Fresnel axicons.

For the logaxicon which is not a revolved prism, equation 8 is not directly applicable. A trial and error approach was used to determine if an effective PSF could be generated by adjusting the term within the Bessel function until the best result was achieved. This produced improvements as can be seen from the processed logaxicon images.

The results are presented in Figure 5.17 to Figure 5.22 for the 5^o axicon, Figure 5.23 to Figure 5.28 for the 5^o fraxicon, Figure 5.29 to Figure 5.34 for the 5^o axicon and Figure 5.35 to Figure 5.39 for the loaxicon. Overall, the results show that the image processing procedure established can be successfully used to recover the images over a long depth of field. It should be mentioned that even though the image quality seems poor, monochromatic light was used and minimal external lighting was provided in order to focus on accurately characterizing the axicons.

(a)

(b)

(c)

Figure 5.17: Images from 5º axicon for:
p = 20mm, q = 20mm
a) original greyscale image (Picture 82.jpg)
b) original + AHE
c) after Wiener deconvolution + AHE

ImageProcessor(I,0.02,0.02,68,0.11,1.083)

(a)

(b)

(c)

Figure 5.18: Images from 5º axicon for:
p = 30mm, q = 20mm
a) original greyscale image (Picture 80.jpg)
b) original + AHE
c) after Wiener deconvolution + AHE
ImageProcessor(I,0.02,0.02,54,0.115,1.083)

(a)

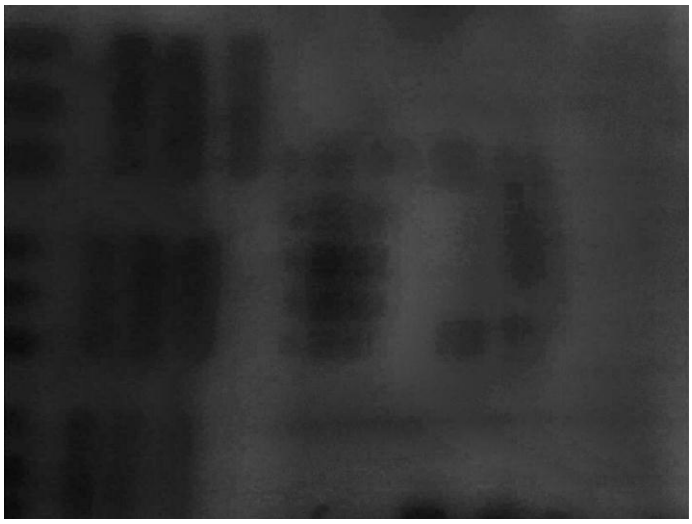

(b)

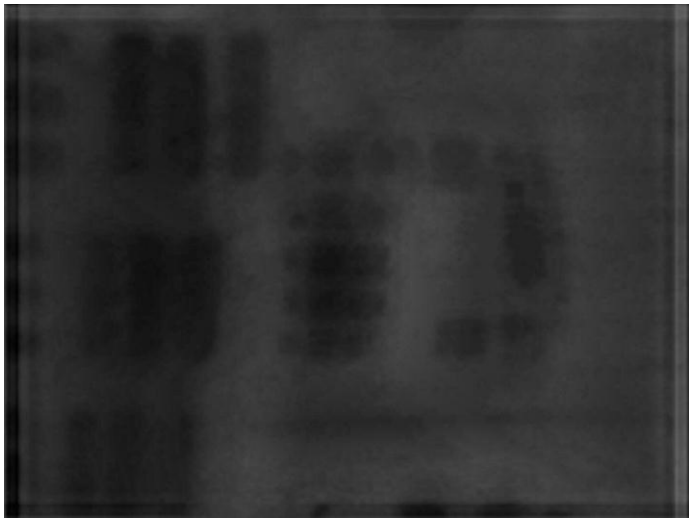

(c)

Figure 5.19: Images from 5º axicon for:
p = 40mm, q = 20mm
a) original greyscale image (Picture 82.jpg)
b) original + AHE
c) after Wiener deconvolution + AHE
ImageProcessor(J,0.04,0.02,60,0.113,1.066)

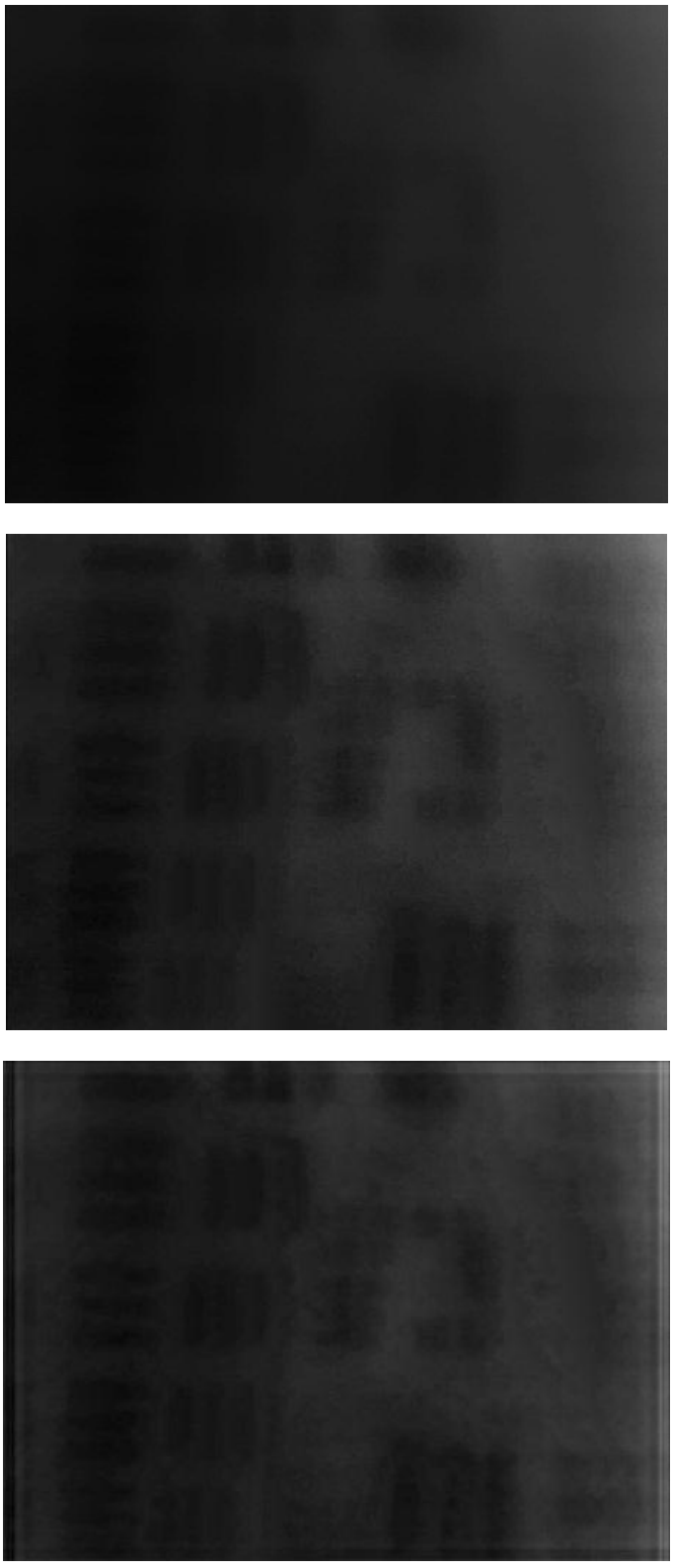

(a)

(b)

(c)

Figure 5.20: Images from 5º axicon for:
p = 60mm, q = 20mm
a) original greyscale image (Picture 83.jpg)
b) original + AHE
c) after Wiener deconvolution + AHE
ImageProcessor(I,0.06,0.02,50,0.125,0.95)

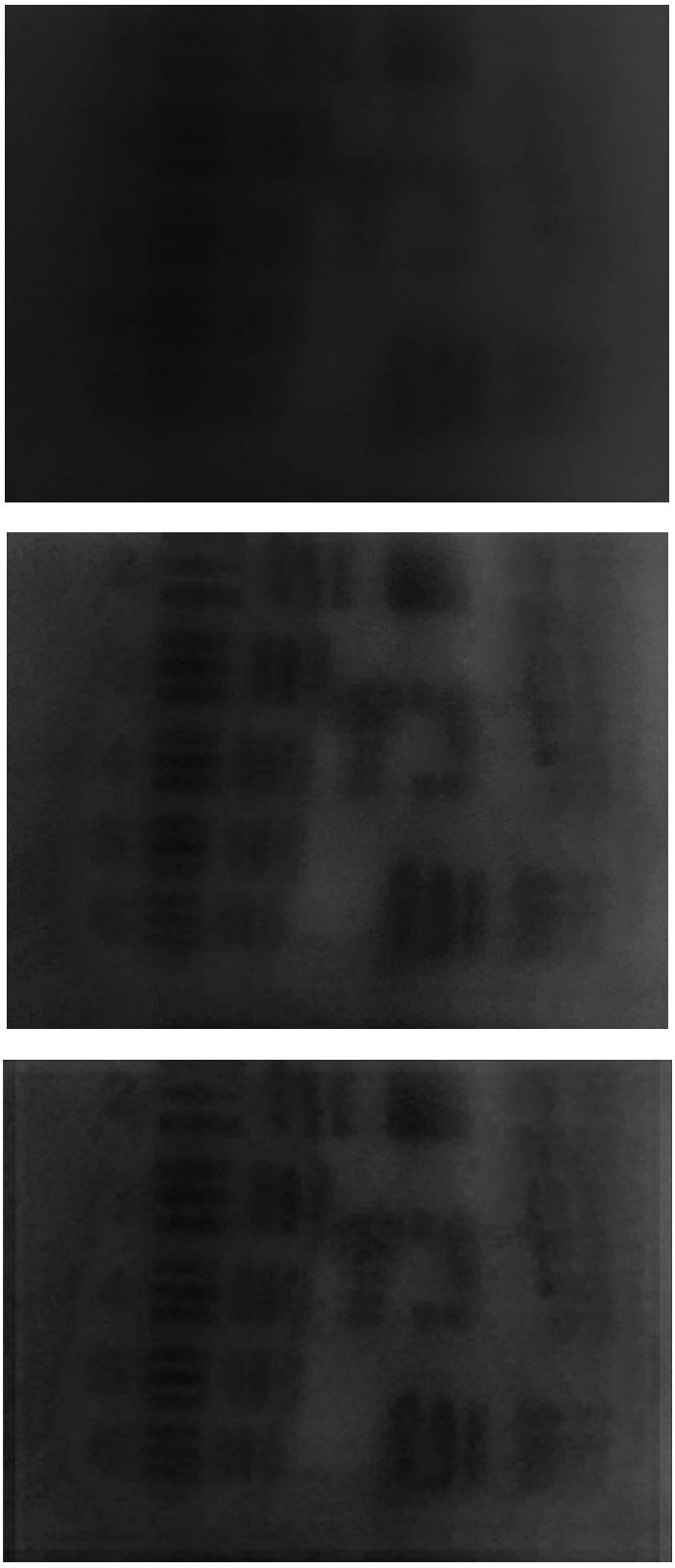

(a)

(b)

(c)

Figure 5.21: Images from 5º axicon for:
p = 80mm, q = 20mm
a) original greyscale image (Picture 84.jpg)
b) original + AHE
c) *after Wiener deconvolution + AHE*
ImageProcessor(I,0.06,0.02,50,0.125,0.86)

(a)

(b)

(c)

Figure 5.22: Images from 5º axicon for:
p = 100mm, q = 20mm
a) original greyscale image (Picture 94.jpg)
b) original + AHE
c) after Wiener deconvolution + AHE
ImageProcessor(I,0.10,0.02,60,0.125,0.77)

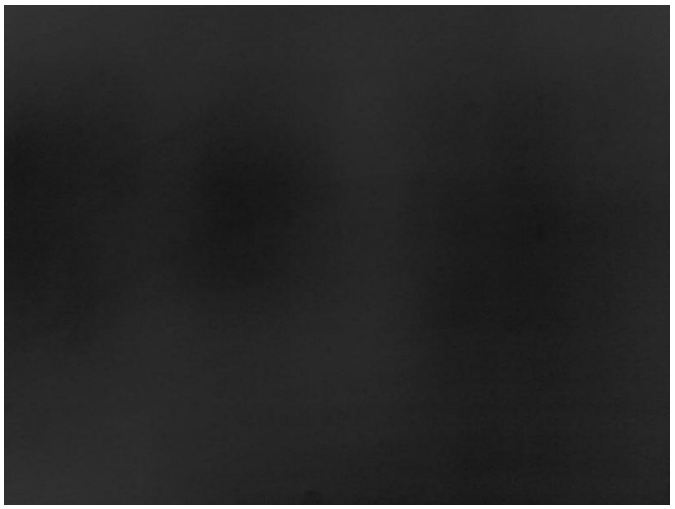

(a)

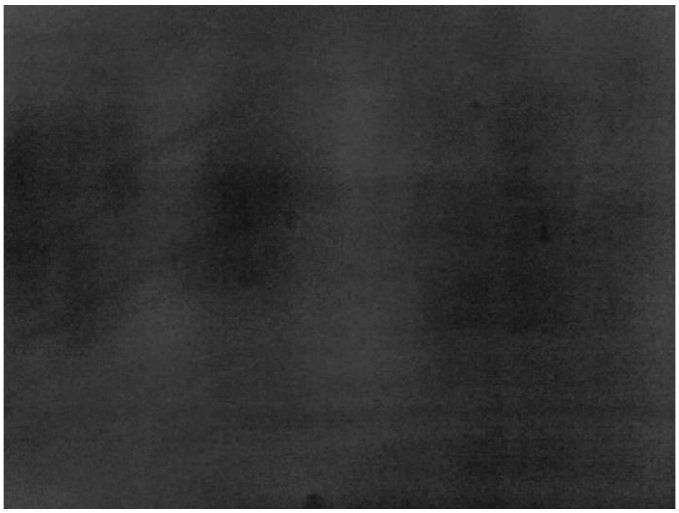

(b)

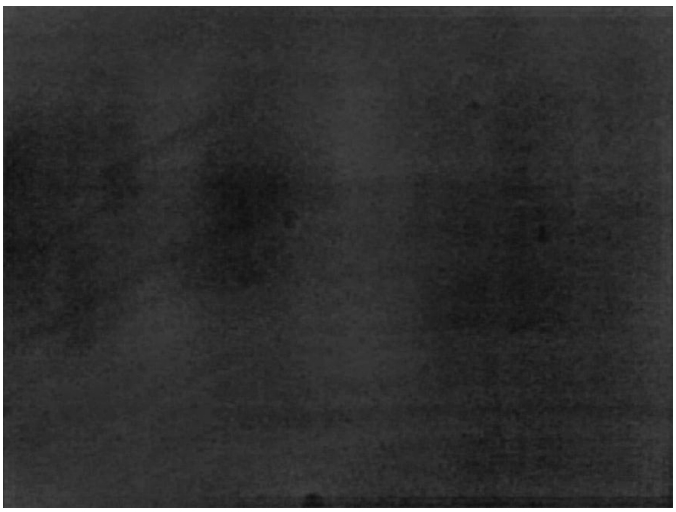

(c)

Figure 5.23: Images from 5º fraxicon for:
p = 20mm, q = 20mm
a) original greyscale image (Picture 157.jpg)
b) original + AHE
c) after Wiener deconvolution + AHE
ImageProcessor(I,0.02,0.02,50,0.11,1.337)

(a)

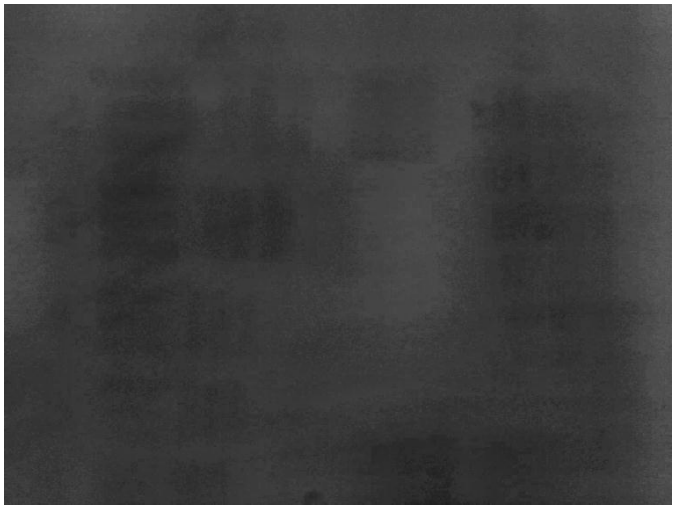

(b)

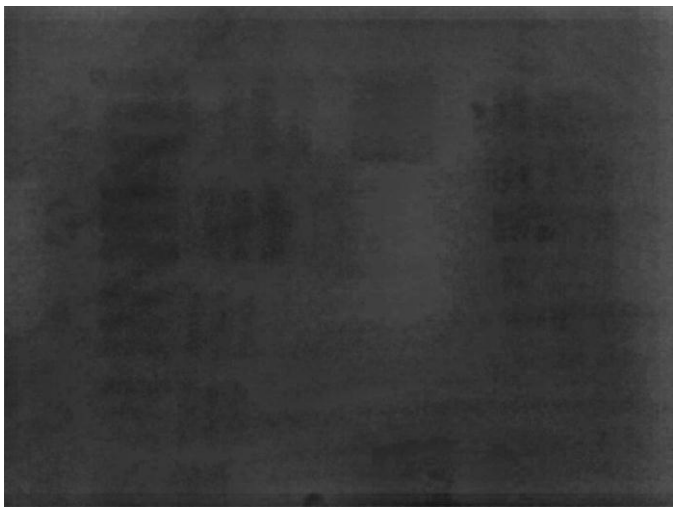

(c)

Figure 5.24: Images from 5º fraxicon for:
p = 30mm, q = 20mm
a) original greyscale image (Picture 163.jpg)
b) original + AHE
c) after Wiener deconvolution + AHE
ImageProcessor(I,0.03,0.02,60,0.10,1.28)

(a)

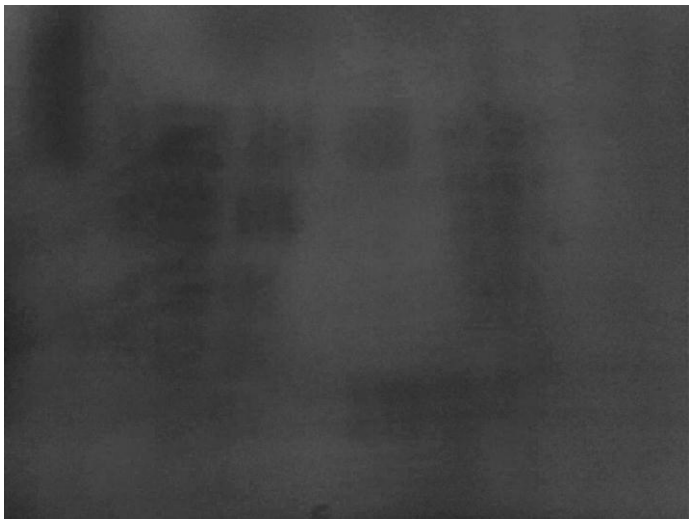

(b)

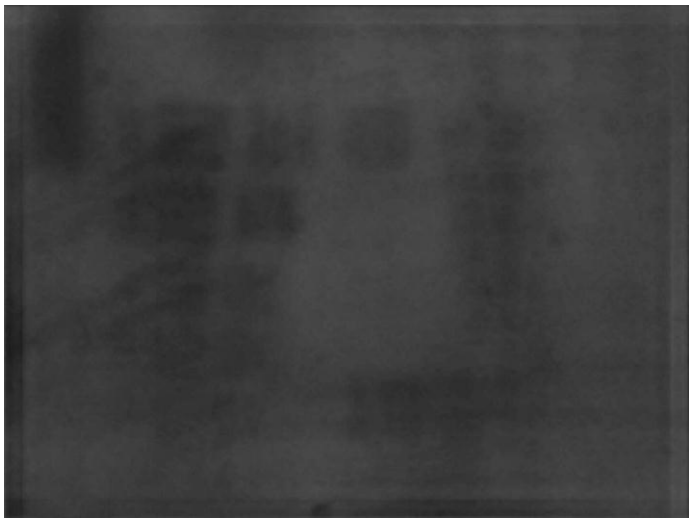

(c)

Figure 5.25: Images from 5º fraxicon for:
p = 40mm, q = 20mm
a) original greyscale image (Picture 169.jpg)
b) original + AHE
c) after Wiener deconvolution + AHE
ImageProcessor(I,0.04,0.02,80,0.11,1.273)

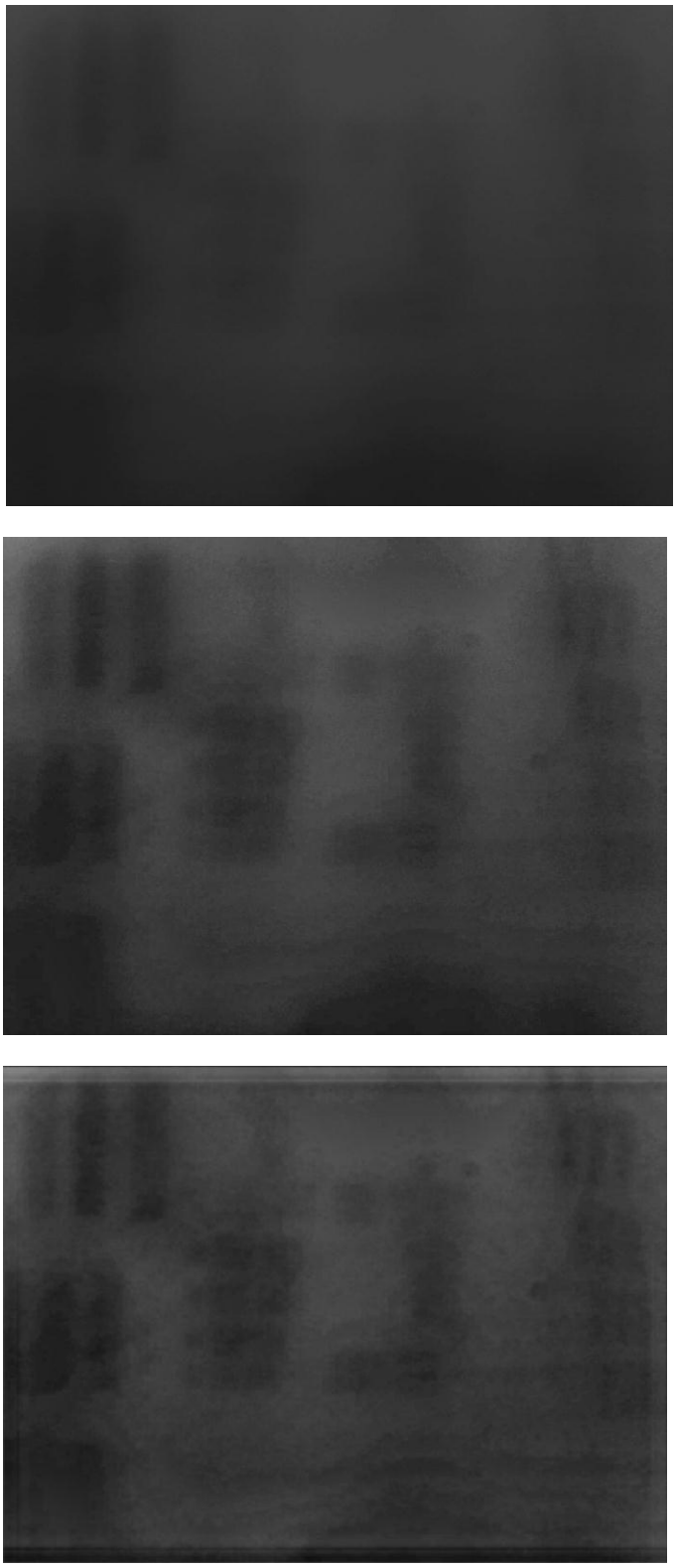

(a)

(b)

(c)

Figure 5.26: Images from 5º fraxicon for:
p = 60mm, q = 20mm
a) original greyscale image (Picture 174.jpg)
b) original + AHE
c) after Wiener deconvolution + AHE
ImageProcessor(I,0.06,0.02,70,0.10,1.175)

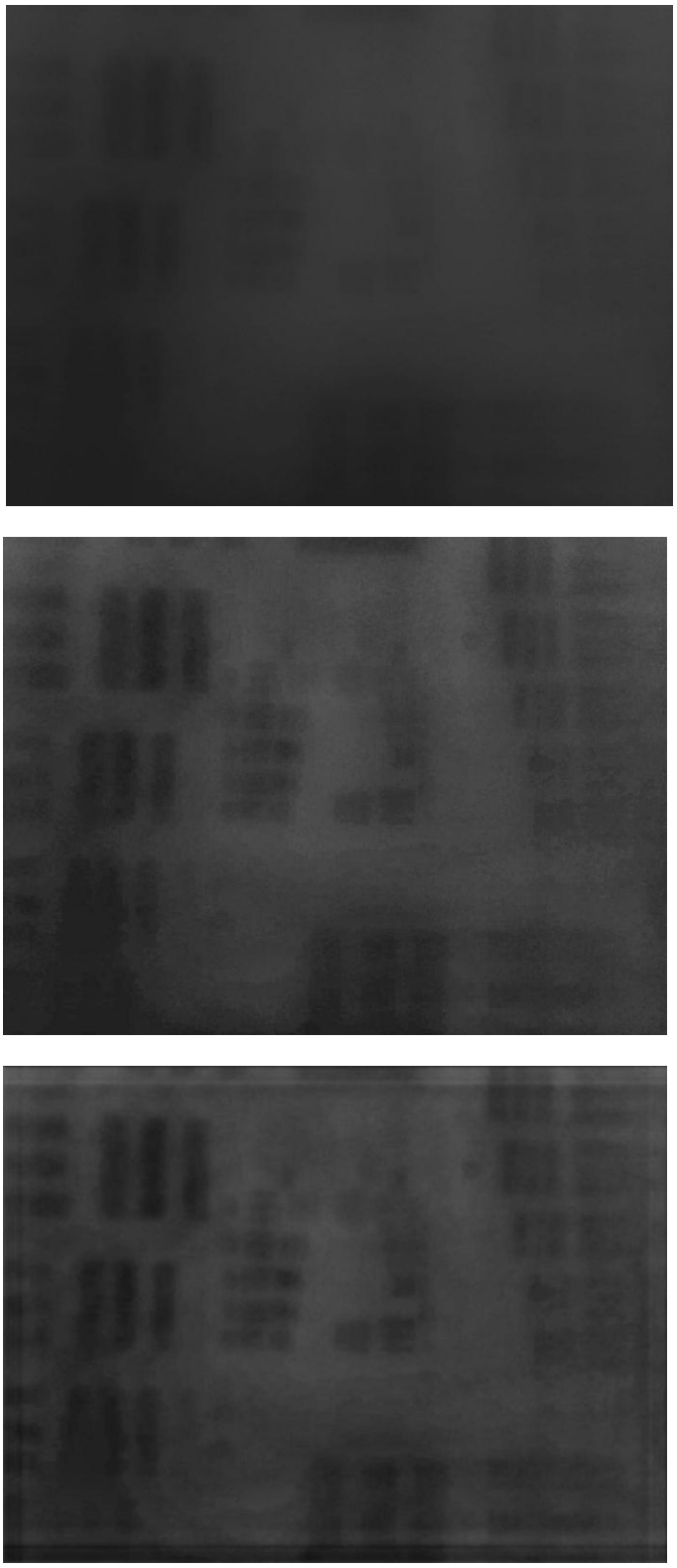

(a)

(b)

(c)

Figure 5.27: Images from 5º fraxicon for:
p = 80mm, q = 20mm
a) original greyscale image (Picture 180.jpg)
b) original + AHE
c) after Wiener deconvolution + AHE
ImageProcessor(I,0.08,0.02,80,0.11,1.145)

(a)

(b)

(c)

Figure 5.28: Images from 5º fraxicon for:
p = 100mm, q = 20mm
a) original greyscale image (Picture 185.jpg)
b) original + AHE
c) after Wiener deconvolution + AHE
ImageProcessor(I,0.1,0.02,70,0.11,0.89)

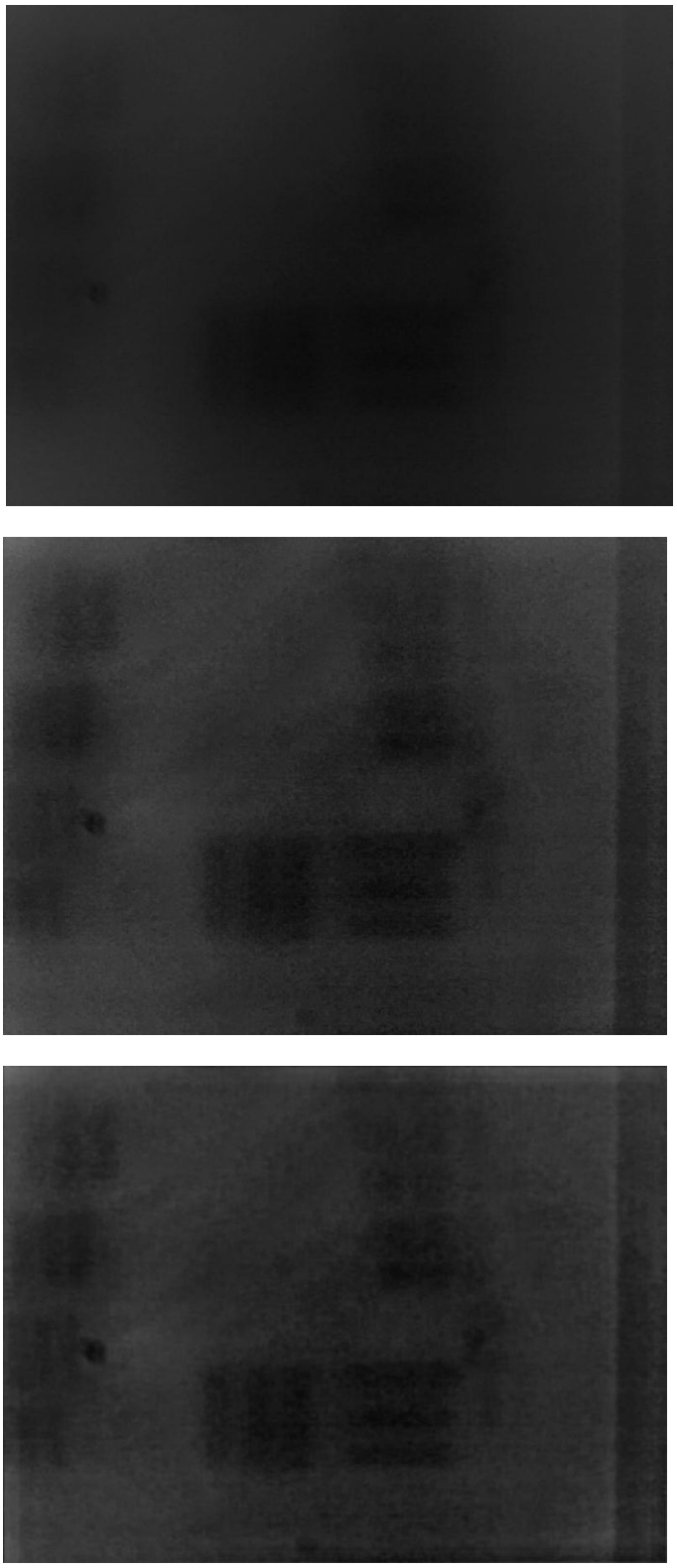

(a)

(b)

(c)

Figure 5.29: Images from 10º axicon for:
p = 20mm, q = 20mm
a) original greyscale image (Picture 380.jpg)
b) original + AHE
c) after Wiener deconvolution + AHE
ImageProcessor(I,0.02,0.02,70,0.11,1)

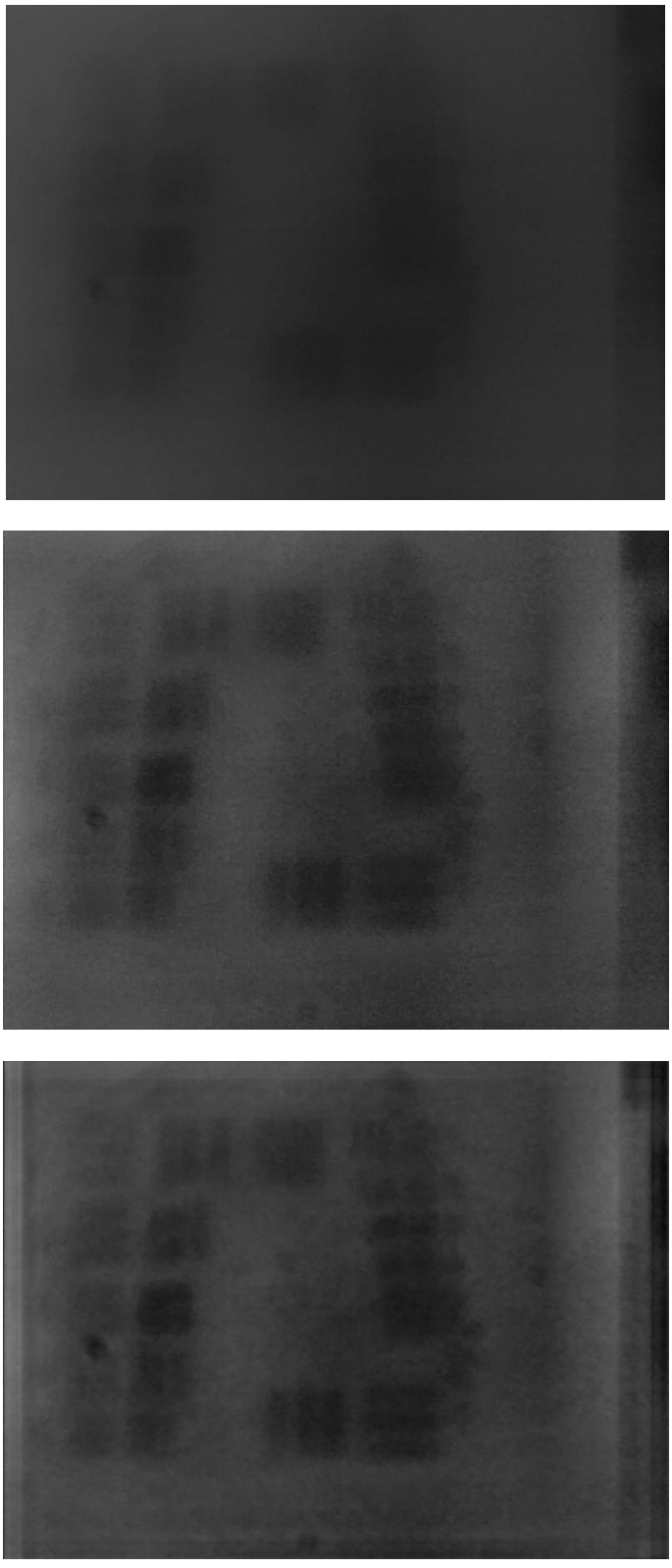

(a)

(b)

(c)

Figure 5.30: Images from 10º axicon for:
p =30mm, q = 20mm
a) original greyscale image (Picture 384.jpg)
b) original + AHE
c) after Wiener deconvolution + AHE
ImageProcessor(I,0.03,0.02,80,0.11,1.05)

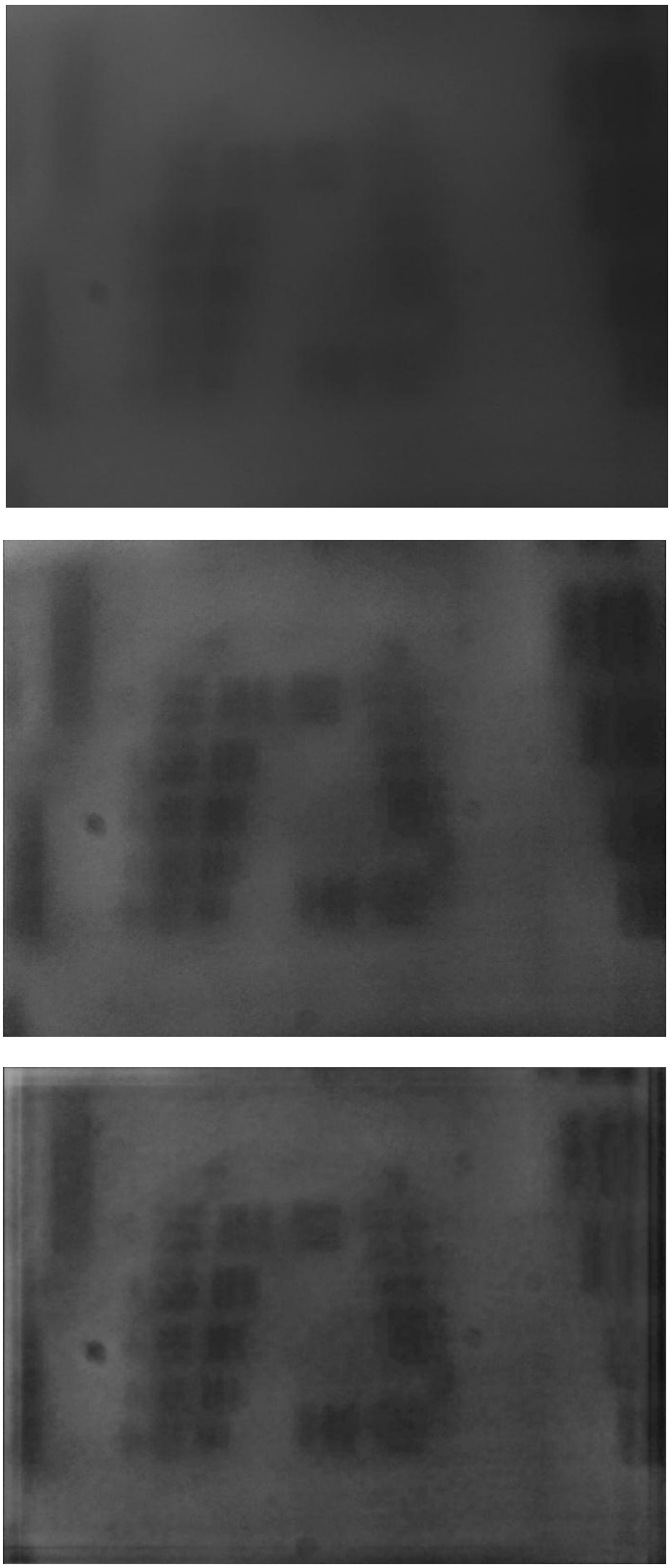

(a)

(b)

(c)

Figure 5.31: Images from 10º axicon for:
p = 40mm, q = 20mm
a) original greyscale image (Picture 388.jpg)
b) original + AHE
c) after Wiener deconvolution + AHE
ImageProcessor(I,0.04,0.02,80,0.09,1.125)

(a)

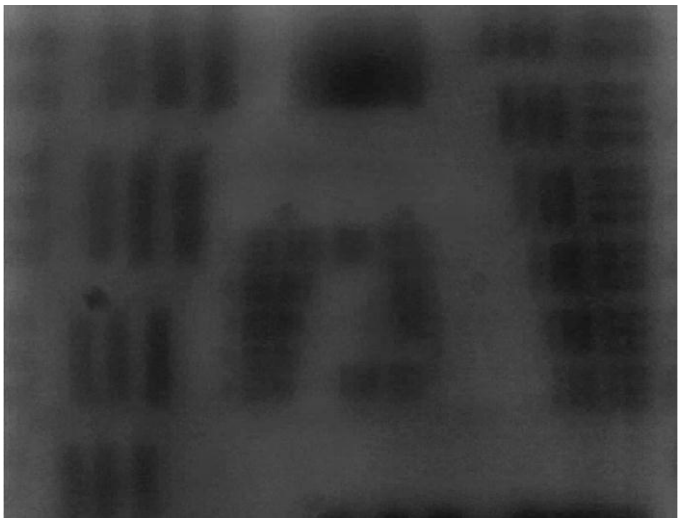

(b)

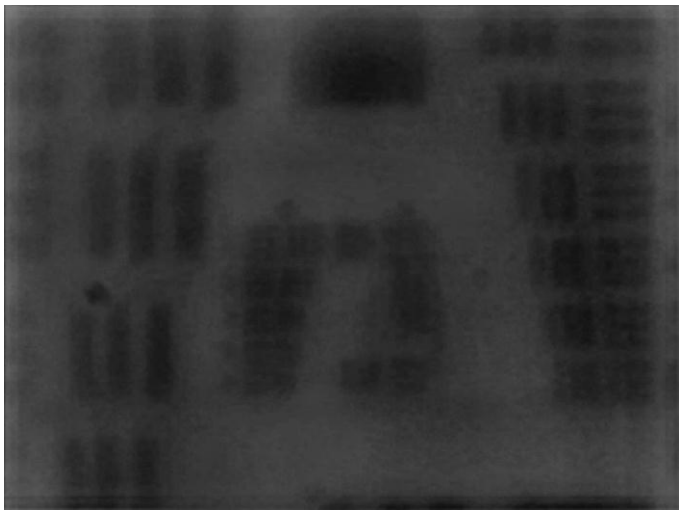

(c)

Figure 5.32: Images from 10º axicon for:
p = 60mm, q = 20mm
a) original greyscale image (Picture 396.jpg)
b) original + AHE
c) after Wiener deconvolution + AHE
ImageProcessor(I,0.06,0.02,60,0.13,1.1)

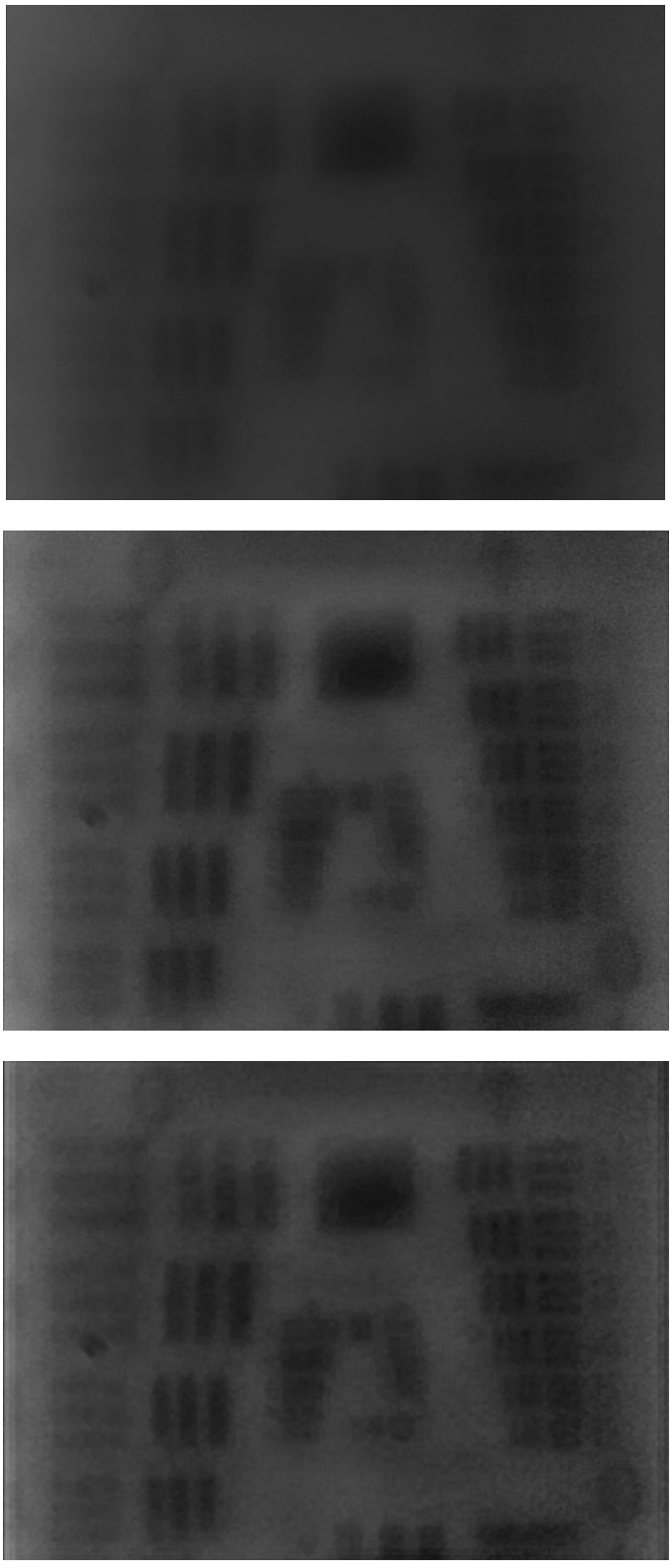

(a)

(b)

(c)

Figure 5.33: Images from 10º axicon for:
p = 80mm, q = 20mm
a) original greyscale image (Picture 400.jpg)
b) original + AHE
c) after Wiener deconvolution + AHE
ImageProcessor(I,0.08,0.02,50,0.11,0.95)

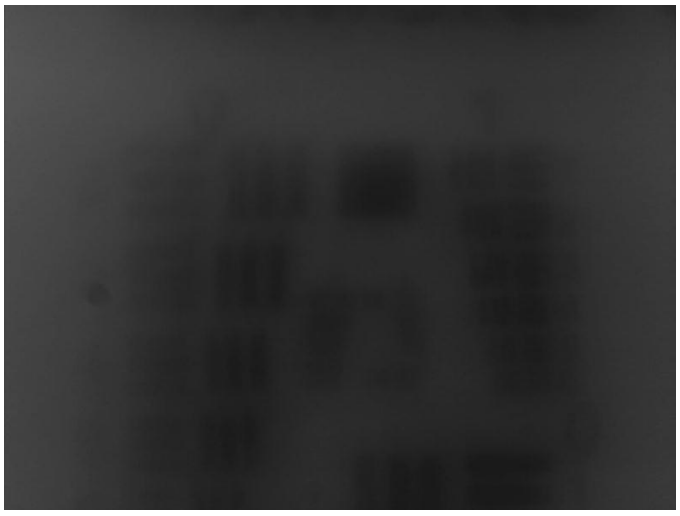

(a)

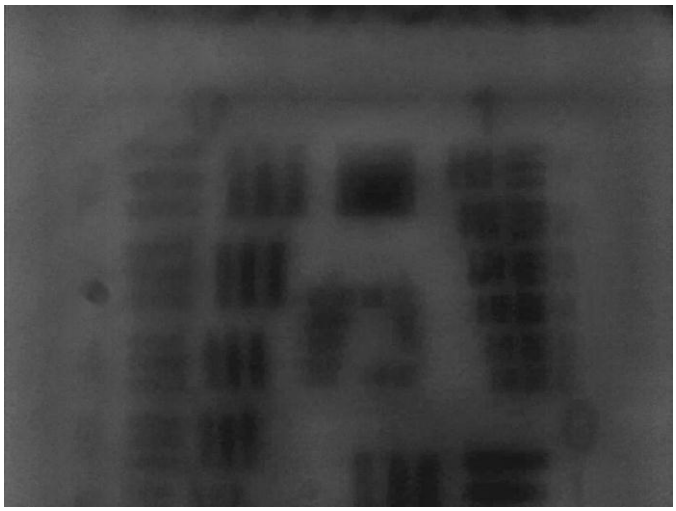

(b)

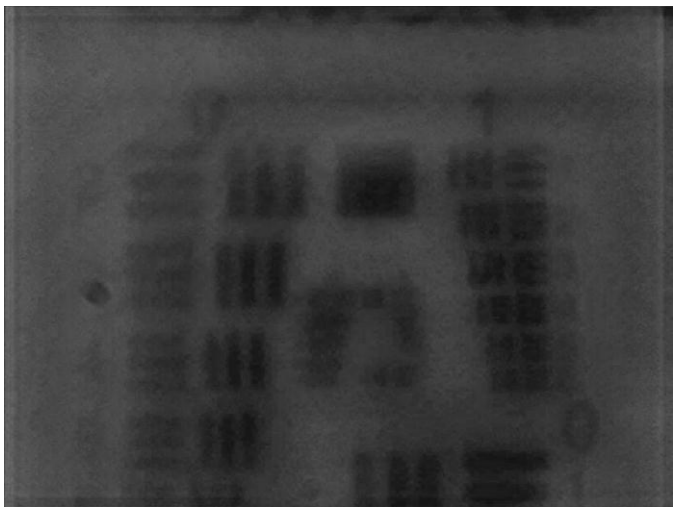

(c)

Figure 5.34: Images from 10º axicon for:
p = 100mm, q = 20mm
a) original greyscale image (Picture 400.jpg)
b) original + AHE
c) after Wiener deconvolution + AHE
ImageProcessor(I,0.1,0.02,40,0.09,0.925)

(a)

(b)

(c)

Figure 5.35: Images from logaxicon for:
p = 175mm, q = 70mm
a) original greyscale image (Picture 282.jpg)
b) original + AHE
c) after Wiener deconvolution + AHE
ImageProcessor(I,0.175,0.07,50,0.09,0.336)

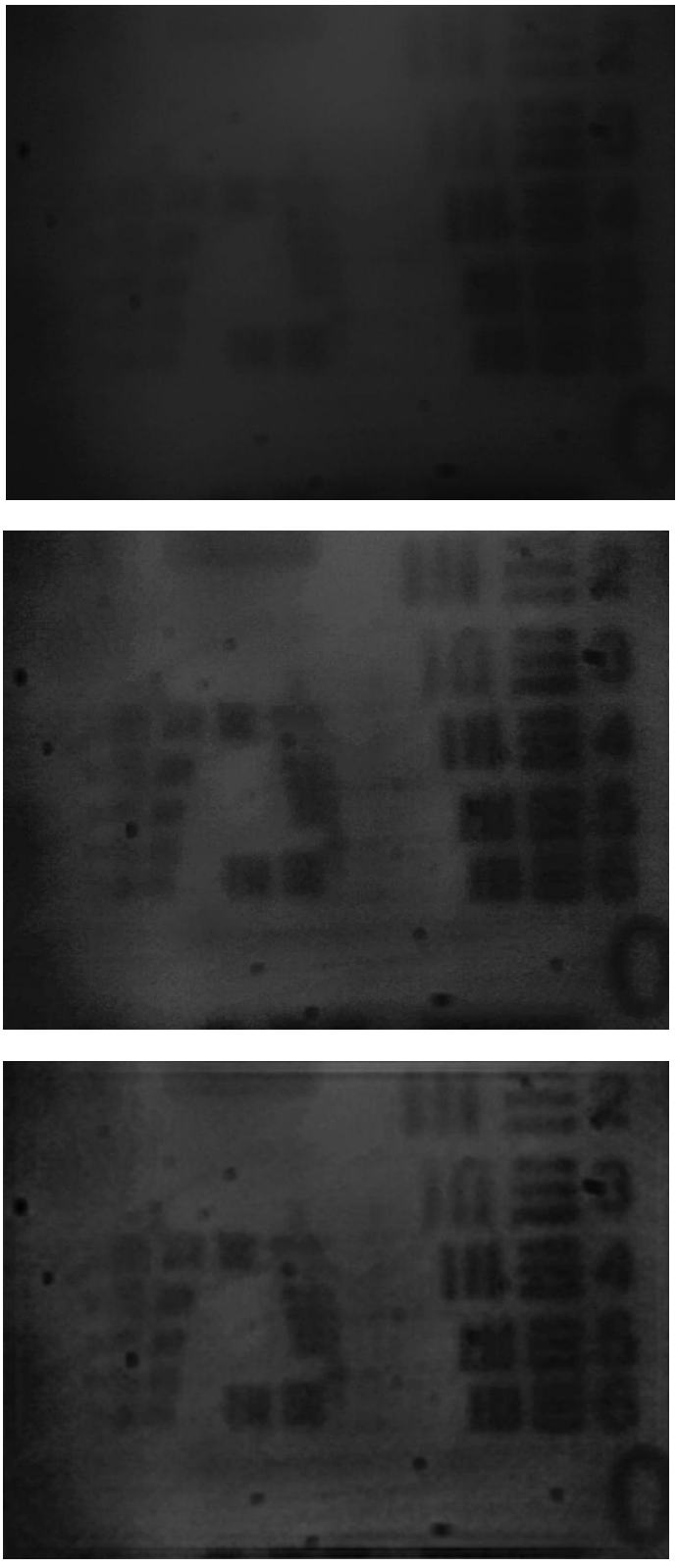

(a)

(b)

(c)

Figure 5.36: Images from logaxicon for:
p = 185mm, q = 70mm
a) original greyscale image (Picture 286.jpg)
b) original + AHE
c) after Wiener deconvolution + AHE
ImageProcessor(I,0.185,0.07,50,0.10,0.308)

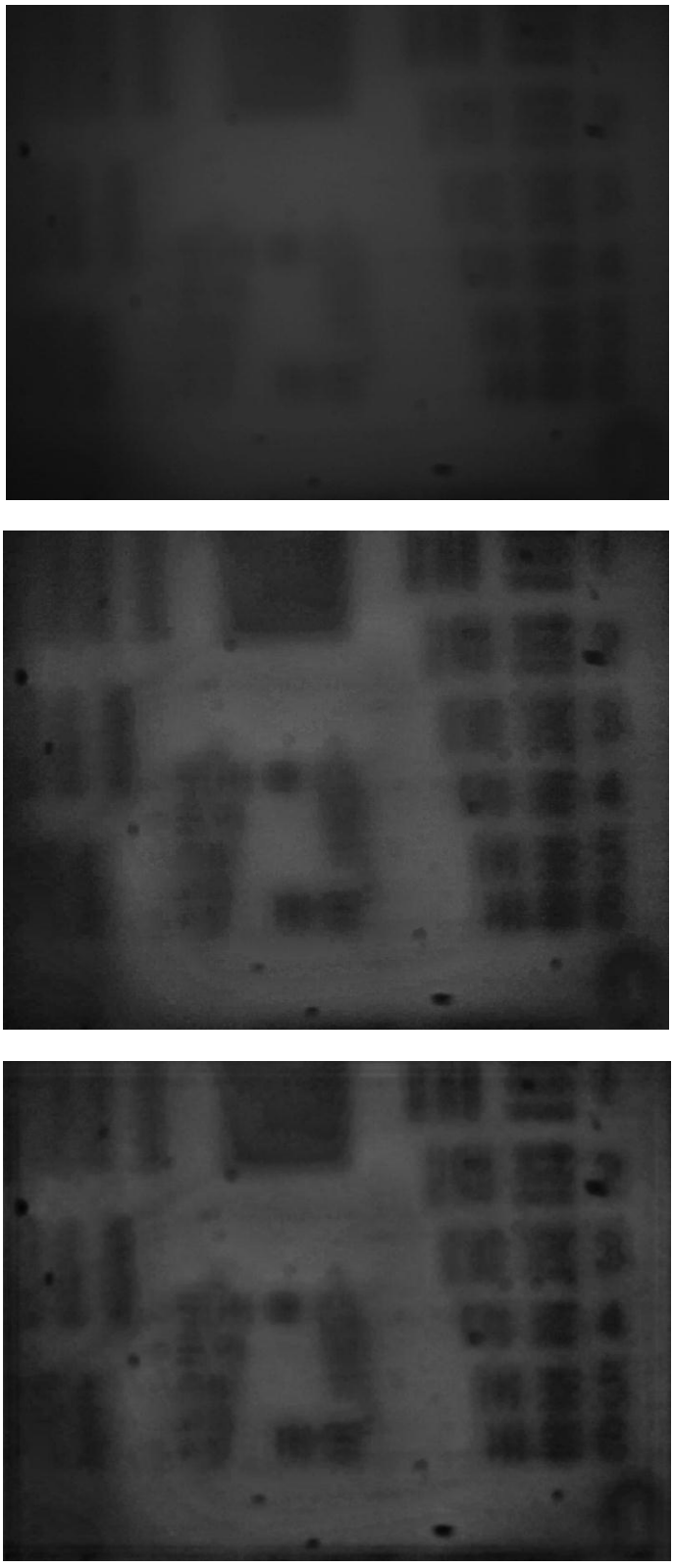

(a)

(b)

(c)

Figure 5.37: Images from logaxicon for:
p = 215mm, q = 70mm
a) original greyscale image (Picture 294.jpg)
b) original + AHE
c) after Wiener deconvolution + AHE
ImageProcessor(I,0.215,0.07,70,0.11,0.419)

(a)

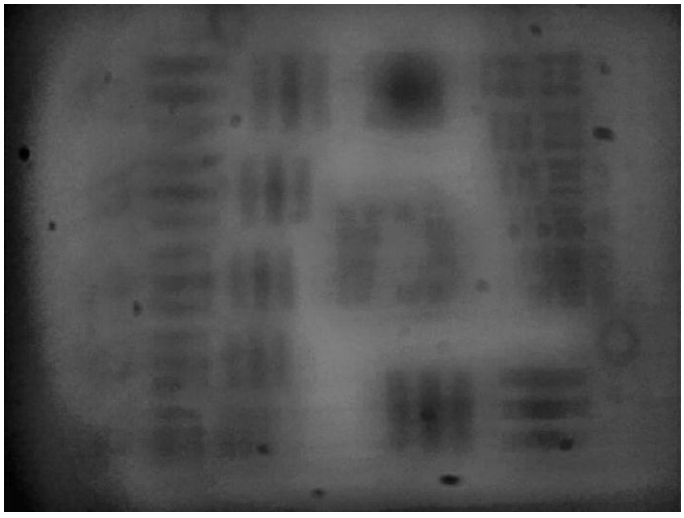

(b)

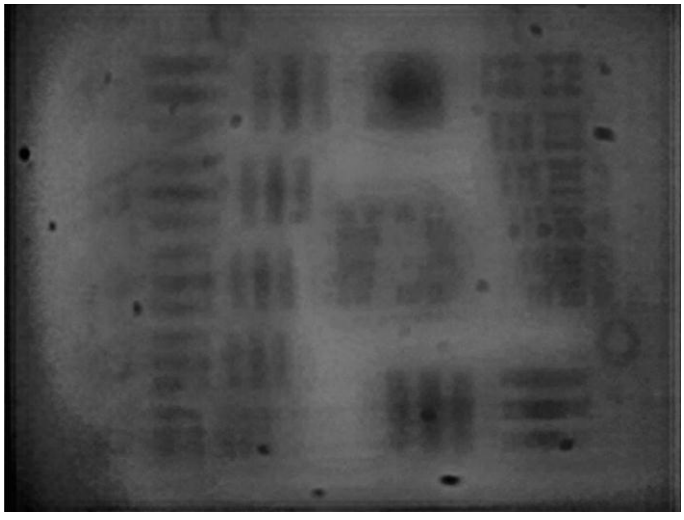

(c)

Figure 5.38: Images from logaxicon for:
p = 355mm, q = 70mm
a) original greyscale image (Picture 310.jpg)
b) original + AHE
c) after Wiener deconvolution + AHE
ImageProcessor(I,0.355,0.07,50,0.10,0.48)

(a)

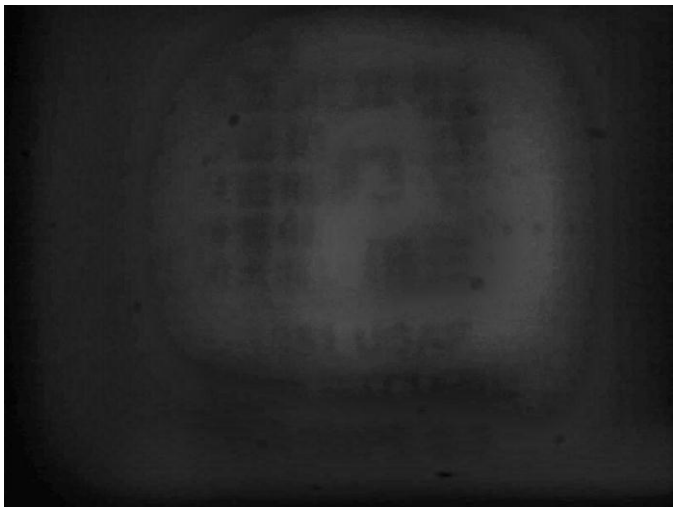

(b)

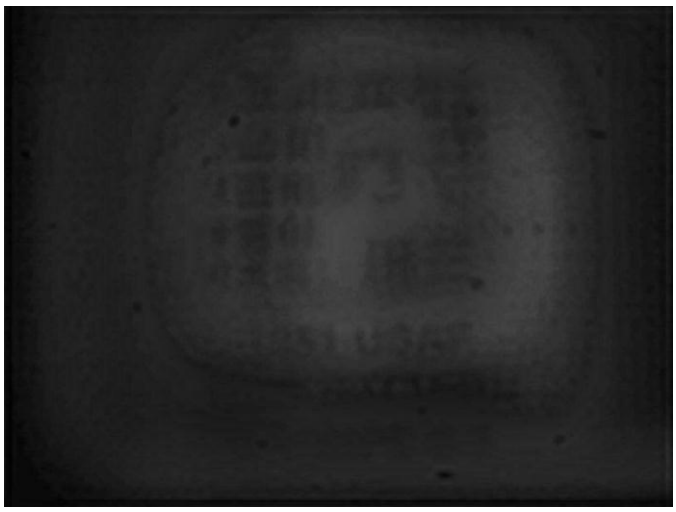

(c)

Figure 5.39: Images from logaxicon for p = 655mm, q = 70mm
a) original greyscale image (Picture 318.jpg)
b) original + AHE
c) after Wiener deconvolution + AHE
ImageProcessor(I,0.655,0.07,30,0.12,0.5)

Chapter VI
CONCLUSIONS

The measurements presented in this paper bring us closer to implementing an imaging system to be used in enclosures, which allows viewing without the need to move the optical element inside the enclosure. The intention was to use a fiber optic bundle telescopic axicon system which allows remote focusing and isotropic scaling at the same time. This was not possible because of diffraction from the individual fibers of the bundle. Instead separate systems of an axicon telescope in free air and a fiber optics bundle single axicon system were used to prove the isotropic scaling and the extended depth of field imaging separately. Using an axicon with a base angle comparable to the angle of diffraction would probably work and is planned for the future.

Implementation of a borescope with an axicon is likely to require image processing to achieve satisfactory results. In order to develop an effective image processing algorithm, different axicons have been characterized in this document. Measuring the systems impulse response was necessary for the development of an integrated optoelectronic imaging system. As a side benefit, digitizing the image renders a fiber optic bundle redundant (video borescope), thereby reducing the overall cost of the end product. As a further benefit, removal of the fiber bundle negates image degradation caused by it.

The imaging properties of three axicons, namely a regular axicon, a logarithmic axicon and a Fresnel axicon, were studied in detail. This study showed that it is possible to take advantage of the extended DOF of these optical elements. An image processing procedure was developed and allowed enhancement of the images obtained using these elements. The logarithmic axicon

usually has superior imaging quality, probably due in part to it having constant intensity over its DOF. Superior azimuthal symmetry of PSFs acquired using the logaxicon, it could be argued, suggest superior imaging properties (comments from Piché, 2013). The lack of comparable symmetry in many of the regular axicon PSFs may be due to poor alignment, flexing of the optics in their mounts (the axicons were much thinner and possibly more prone to deformation) or imperfections in the tip of the axicon elements (Brzobohatý et al.,2008). The Fresnel axicon imaging performance was comparable to that of a regular axicon, which is significant since it has the potential of being cheaper to manufacture.

The characterization of regular axicons and a Fresnel axicon have been synthesized using an equation adapted from Roy and Tremblay (1980). In practice, due to the difficulty acquiring useful degradation functions experimentally, these calculated PSFs produce superior results. This equation can also be adapted for use with the logarithmic axicon to good effect as shown in chapter 5. Future work might involve a theoretically generated PSF specifically for the logaxicon.

The best result in terms of resolution limit was achieved with a logaxicon at somewhere between 35 to 40 line pairs/mm (fig. 5.10c). The regular axicon produced an image with a maximum resolution limit of approximately 17.5 lp/mm (fig. 5.7c). Although in some instances, the non-deconvolved images produced a higher resolution image it was never significantly higher. For the most part the deconvolved images produced a slightly better result from the perspective of resolution.

Any practical system that relies on deconvolution would require a means of determining distance to the object so as to compute the PSF. An alternate approach that is both less computationally demanding and would not require object to lens distance information would be a simple

sharpening filter combined with some form of contrast enhancement (most probably some form of AHE). This latter method is arguably less accurate in terms of the end result. It can produce an image that appears sharper, but does so in a way that ignores the specific nature of the degradation.

The refractive logarithmic axicon, in providing the best image quality, is the most promising optical element studied. Since an endoscope is not likely to require more than a 3 or 4 cm DOF, a logaxicon designed with this capability in mind is likely to produce superior image quality to the one studied here, such an element may require only contrast enhancement if any.

The raw images collected here can still be studied with new PSF generation techniques, or entirely different image processing algorithms, with the possibility of producing additional results.

References

Ares García, J., Bará, S., Gomez García, M., Jaroszewicz, Z., Kolodziejczyk, A., and Petelczyc, K. (2008). Imaging with extended focal depth by means of the refractive light sword optical element, Optics Express, Vol. 16, No. 22, pp. 18371-18378.

Arimoto, R., Saloma, C., Tanaka, T.,and Kawata, S. (1992). Imaging properties of axicon in a scanning optical system, Appl. Opt., Vol. 31, pp. 6653-6657.

Arlt, J., and Dholakia, K. (2000). Generation of high-order Bessel beams by use of an axicon, Opt. Commun., Vol. 177, pp. 297-301.

Brzobohatý, O., Cižmár, T. and Zemánek P. (2008). High quality quasi-Bessel beam generated by round-tip axicon, Optics Express, Vol. 16, Issue 17, pp. 12688-12700.

Burvall, A., Kolacz, K., Jaroszewicz, Z., and Friberg, A.T. (2004). Simple lens axicon, Appl. Opt., Vol. 43, pp. 4838-4844.

Burvall, A., Kolacz, K., Goncharov, A.V., Jaroszewicz, Z. and Dainty, C. (2007). Lens axicons in oblique illumination, Appl. Opt., Vol. 46, pp. 312-318.

Brousseau, D., Drapeau, J., Piché, M. and Borra, E.F. (2011). Generation of Bessel beams using a magnetic liquid deformable mirror, Applied Optics, Vol. 50, Issue 21, pp. 4005-4010.

Cathey, W.T., Frieden, B.R., Rhodes, W.T., and Rushforth, C.K. (1984). Image gathering and processing for enhanced resolution, J. Opt. Soc. Am. A, Vol. 1, No. 3, pp. 241-250.

Chebbi, B., Minko, S., Al-Akwaa, N. and Golub, I. (2010). Remote control of extended depth of field focusing, Opt. Commun., Vol. 283, Issue 9, pp. 1678–1683.

Chebbi, B., Golub, I. and Gourley, K. (2012). Homogenization of on-axis intensity distribution produced by a Fresnel refractive axicon, Opt. Commun., Vol. 285, pp. 1636-1641.

Chi, W. and George, N. (2001). Electronic imaging using a logarithmic asphere, Optics Letters, Vol. 26, Issue 12, pp. 875-877.

Čižmár, T. and Dholakia , K. (2009). Tunable Bessel light modes: engineering the axial propagation, Optics Express, Vol. 17, Issue 18, pp. 15558-15570.

Couture, M., and Piche, M. (1993). Focussing properties of an axicon pair, Can. J. Phys. 71-70.

Dépret, B., Verkerk, P. and Hennequin, D. (2002). Characterization and modelling of the hollow beam produced by a real conical lens, Opt. commun., Vol. 211, pp. 31-38.

Davidson, N., Friesem, A.A., and Hasman, E. (1991). Holographic axilens: high resolution and long focal depth, Opt. Lett. 16 pp. 523-525.

Ding, Z., Ren, H., Zhao, Y., Nelson, J.S., and Chen, Z. (2002). High-resolution optical coherence tomography over a large depth range with an axicon lens, Opt. Lett. 27 pp. 243-245.

Dowski, E.R., Cathey, W.T. (1995). Extended depth of field through wave-front coding, Appl. Opt., Vol. 34, No. 11, pp. 1859-1866.

Druart, G., Taboury, J., Guérineau, N., Haïdar, R., Sauer, H., Kattnig, A. and Primot, J. (2008). Demonstration of image-zooming capability for diffractive axicons, Optics Letters, Vol. 33, Issue 4, pp. 366-368.

Dufour, P., McCarthy, N. and De Koninck, Y. (2005). Two-photon microscopy with high depth of field using an axicon, Proc of Conference on Lasers and Electro-Optics (CLEO), Vol. 2, pp. 1515 – 1517.

Durnin, J. (1987). Exact solutions for nondiffracting beams. I. The scalar theory, J. Opt. Soc. Am. A 4 pp. 651-654.

Eah, SK., Jhe, W. and Arakawa, Y. (2003). Nearly diffraction-limited focusing of a fiber axicon microlens, Rev. Sci. Instrum. 74, pp. 4969-4971.

Friberg, A.T. (1996). Stationary-phase analysis of generalized axicons, JOSA A 13 (4), pp.743-750.

Golub, I., Tremblay, R. (1990). Light focusing and guiding by an axicon-pair-generated tubular light beam, J. Opt. Soc. Am. B 7 pp. 1264-1267.

Golub, I. (2007). Solid immersion axicon: maximizing nondiffracting or Bessel beam resolution, Opt. Lett. 32, pp. 2161-2163.

Golub, I. (1995). Superluminal-source-induced emission, Opt. Lett. 20, pp. 1847-1849.

Golub, I. (2006). Fresnel axicon, Opt. Lett. 31, pp. 1890-1892.

Golub, I., Chebbi, B., Shaw, D., and Nowacki, D. (2010). Characterization of a refractive logarithmic axicon, Opt. Lett. 35, pp. 2828-2830.

Gonzalez, R.C., Woods, R.E. and Eddins, S.L. (2004). Digital Image Processing using Matlab, Prentice Hall.

Gourley, K., Golub, I. and Chebbi, B. (2009). First experimental demonstration of a Fresnel axicon, Proc. SPIE v. 7099.

Gourley, K., Golub, I. and Chebbi, B. (2011). Demonstration of a Fresnel axicon, Appl. Opti. 50, pp. 303-306.

Herman and R. M. Wiggins, T. A. (1991). Production and uses of diffraction less beams, J. Opt. Soc. Am. A8(6), pp. 932–942.

Jaroszewicz, Z., Sochacki, J., Kolodziejczyk, A., Staronski, L.R. (1993). Apodized annular-aperture logarithmic axicon: smoothness and uniformity of intensity distributions, Optics Letters, Vol. 18, Issue 22, pp. 1893-1895.

Jaroszewicz, Z. (1997). Axicons Design and Propagation Properties, Res. Dev. Treatises v. 5, SPIE Polish Chapter.

Kotlyar, V.V.; Kovalev, A.A.; Stafeev, S.S.; Soifer, V.A. (2011). Diffraction of a Gaussian beam by a logarithmic axicon, J. Opt. Soc. Am. A., Vol. 28, No. 5, pp. 844-849.

Kuang, D. and Fang, Z. (2010). Microaxicave: inverted microaxicon to generate a hollow beam, Optics Letters, Vol. 35, Issue 13, pp. 2158-2160.

Lee, K.S., Rolland, J.P. (2008). Bessel beam spectral-domain high-resolution optical coherence tomography with micro-optic axicon providing extended focusing range, Optics Letters, Vol. 33, Issue 15, pp. 1696-1698.

Lei, M. and Yao, B. (2004). Characteristics of beam profile of Gaussian beam passing through an axicon, Opt. Commun., Vol. 239, pp. 367-372.

McLeod, J.H. (1954). The Axicon: A New Type of Optical Element, J. Opt. Soc. Am. 44, pp. 592-597.

McLeod, J.H. (1960). Axicons and their uses, J. Opt. Soc. Am. 50, pp. 166-169.

Matsuoka, Y., Kizuka, Y. and Inoue, T. (2006). The characteristics of laser micro drilling using a Bessel beam, Applied Physics A: Materials Science & Processing, Vol. 4, No. 4, pp. 423-430.

Mikuła, G., Jaroszewicz, Z., Kolodziejczyk, A., Petelczyc, K., and Sypek, M. (2007). Imaging with extended focal depth by means of lenses with radial and angular modulation, Optics Express, Vol. 15, No. 15. pp. 9184-9193.

Mikuła, G., Kolodziejczyk, A., Makowski, M., Prokopowicz, C. and Sypek, M. (2005). Diffractive elements for imaging with extended depth of focus, Opt. Eng., Vol. 44, Issue 5, 058001.

Ojeda-Castaneda, J., Tepichin, E. and Diaz, A. (1989). Arbitrarily high focal depth with a quasioptimum real and positive transmittance apodizer, Appl. Opt., Vol. 28, pp. 2666-2670.

Overfelt, P. L. and Kenney, C. S. (1991). Comparison of the propagation characteristics of

Bessel, Bessel-Gauss, and Gaussian beams diffracted by a circular aperture, JOSA A, Vol. 8 Issue 5, pp.732-745.

Paterson, C. and Smith, R. (1996). Higher-order Bessel waves produced by axicon-type computer-generated holograms, Opt. Commun., Vol. 124, pp. 121-130.

Popov, S.U. and Friberg, A.T. (1998). Design of diffractive axicons for partially coherent light, Opt. Letters, Vol. 23, No. 21, pp. 1639-1641.

Ren, O. and R Birngruber, R. (1990). Axicon: a new laser beam delivery system for corneal surgery, IEEE Journal of Quantum Electronics, Vol. 26, No. 12, pp. 2305-2308.

Roy, G. and Tremblay, R. (1980). Influence of the divergence of a Laser Beam on the Axial Intensity Distribution of an Axicon, Optics Comm. Vol. 34, number 1.

Rioux, M., Tremblay, R. , Belanger, P.-A. (1978). Linear, annular, and radial focusing with axicons and applications to laser machining, Appl. Opt. 17, pp. 1532-1536.

Shao, B., Esener, S., Nascimento, J., Botvinick, E.L. , Berns, M.W. (2006). Dynamically adjustable annular laser trapping based on axicons, Appl. Opt. 45, pp. 6421-6428.

Staroński, L.R., Sochacki, J., Jaroszewicz, Z. and Kołodziejczyk, A. (1992). Lateral distribution and flow of energy in uniform-intensity axicons, J. Opt. Soc. Am. A, Vol. 9, Issue 11, pp. 2091-2094.

Turunen, J., Vasara, A., Friberg, A.T. (1988). Holographic generation of diffraction-free beams, Appl. Opt., Vol. 27, pp. 3959-3962.

Voigt, A., Heitkam, S., Büttner, L., Czarske, J. (2009). A Bessel beam laser Doppler velocimeter, Opt. Commun., Vol. 282, pp. 1874-1878.

Zhai, Z., Ding, S., Lv, Q.H., Wang, X., Zhong, Y. (2009). Extended depth of field through an axicon, Journal of modern Optics, Vol. 56, 11, pp. 1304-1308.